Clarifying detailed resistivity structures in seafloor hydrothermal fields by inversion of electric and electromagnetic data

Keiichi Ishizu

Clarifying detailed resistivity structures in seafloor hydrothermal fields by inversion of electric and electromagnetic data

Keiichi Ishizu

Department of Urban Management

Graduate School of Engineering

Kyoto University

2020

電気及び電磁データ逆解析法による
海底熱水域での比抵抗構造の詳細解明

石須慶一

京都大学工学研究科　都市社会工学専攻

2020 年

Contents

List of Figures

List of Tables

Abbreviations

1D: One-Dimensional

2D: Two-Dimensional

3D: Three-Dimensional

3DDOCSEM: 3D Data-space Occam inversion algorithm for CSEM data

AUV: Autonomous Underwater Vehicle

CSEM: Controlled Source ElectroMagnetic

CTD: Conductivity-Temperature-Depth

DCR: Direct Current Resistivity

EEZ: Exclusive Economic Zone

EM: ElectroMagnetic

ERT: Electrical Resistivity Tomography

FDM: Finite Difference Method

FEM: Finite Element Method

GN: Gauss Newton

HED: Horizontal Electric Dipole

IE: Integral Equation

LWD: Logging While Drilling

mbsf: meters below seafloor

MBES: Multibeam Echosounders

MPI: Message Passing Interface

MT: MagneTotelluric

NBC: North Big Chimney

NLCG: Non Linear Conjugate Gradient

OBE: Ocean Bottom Electrometer

OBEM: Ocean Bottom ElectroMagnetometers

QN: Quasi Newton

RHS: Right Hand Sides

RMS: Root Mean Square

ROV: Remotely Operated Vehicle

SMS: Seafloor Massive Sulfide

TAG: Trans Atlantic Geotraverse

TEM: Transient ElectroMagnetic

VMS: Volcanogenic Massive Sulfide

Abstract

This thesis consists of the development of resistivity imaging techniques based on inversion algorithms of electric and electromagnetic data for the exploration of seafloor massive sulfide (SMS) deposits. I specifically developed inversion algorithms of 2D marine electrical resistivity tomography (ERT) surveys and 3D controlled source electromagnetic (CSEM) surveys. The ERT survey tows a transmitter and eight electrode pairs of receivers for increasing resolution to shallow resistivity structures. Inversions of the towed ERT data recover the high-resolution resistivity structures near the seafloor. I focus on a CSEM survey consisting of a towed transmitter and ocean-bottom receivers on the seafloor to investigate deep resistivity structures. Various 3D CSEM data sets can be obtained with the array. Data with long transmitter and receiver offset has deeper penetration. 3D inversions of the CSEM data present resistivity structures covering the deep area below the seafloor. The developed 2D ERT inversion algorithm was applied to real field data collected in the Iheya hydrothermal fields, Okinawa. The recovered high resolution resistivity image clarified a semi-layered resistivity structure, interpreted as SMS deposits exposed on the seafloor, and another deep-seated SMS layer at about 40 m depth below the seafloor. The developed 3D CSEM inversion algorithm was applied to real field data collected in the Ieyama hydrothermal fields, Okinawa. The obtained 3D resistivity image to a depth of a few hundred meters revealed low resistivity anomalies below the seafloor. The conductive anomalies might be related to the formation of SMS. These results showed a combination between the inversion of ERT and CSEM data enabled seamless imaging of shallow and deep resistivity structures.

The first chapter consists of the introduction of the thesis. Recently, SMS deposits are focused as next-generation resources due to high global demands for metal. SMS deposits form through hydrothermal circulation below the seafloor, which is a process of heat and material exchange between seawater and the crust. The occurrences of SMS deposits are found at mid-ocean ridges, back-arc spreading centers, volcanic arcs, and so on. Hydrothermal activity and its associated SMS deposits have been found in Okinawa and Izu-Ogasawara Sea, Japan. Researchers from both academy and industry have conducted various surveys toward the development of SMS deposits. To investigate the distribution of SMS, various geophysical methods such as seismic, gravity, electric and electromagnetic (EM) surveys have been used. In this thesis, I focus on electric and EM surveys to investigate resistivity structures of SMS. The surveys are useful for imaging of SMS because SMS shows much lower resistivity compared to the surrounding rock. Pilot EM surveys in Trans-Atlantic Geotraverse (TAG) hydrothermal field, Mid-Atlantic Ridge revealed that the low resistivity area is consistent with SMS deposits. New EM systems have been developed to image SMS deposits because of the increasing interest in SMS deposits. However, the used EM surveys have two major problems. First, the detailed resistivity structures of SMS deposits have not been obtained. Next, the resistivity images covering deep

structures in hydrothermal fields have not been reported although the reservoirs and its associated buried SMS can be located at a depth of more than 100 m below the seafloor. Due to the problems, the distributions of SMS deposits are poorly known. Therefore, I develop a resistivity imaging technique using an inversion algorithm of 2D marine ERT surveys and 3D CSEM surveys to investigate shallow and deep resistivity structures in the hydrothermal fields.

The second chapter consists of the development of the forward modeling scheme of the 2D marine ERT survey and the 3D marine CSEM survey. Accurate and efficient forward modeling schemes are necessary for the inversion algorithms. For the near-seafloor explorations using 2D ERT modeling, the detailed bathymetry should be included in the modeling. I developed a 2D marine ERT forward modeling scheme based on the FEM with unconstructed meshes. The precise modeling of bathymetry with the unconstructed meshes enabled high-resolution ERT surveys for the near-seafloor exploration. Comparing the forward responses with analytical solution from the two-layer model showed the forward modeling scheme could produce accurate solutions. A 3D marine CSEM forward modeling scheme was developed. The FDM with a scattered field approach is used for the CSEM forward modeling scheme. The relatively rough mesh could be used for the modeling due to the scattered field approach. The linear equation in the 3D CSEM modeling was solved by a multicore parallel sparse direct solver PARDISO. The direct solver enables the fast computation of solving the forward problems. The performance of the forward modeling scheme was investigated using 1D and 3D examples. Numerical experiments with 1D and 3D examples showed that the forward modeling code could produce accurate solutions at a range of transmitter and receiver less than 10 km.

The third chapter consists of the development of an inversion algorithm of the 2D marine ERT survey and the 3D marine CSEM survey. Occam inversion scheme was applied to both inversion algorithms due to its robustness and efficiency. The model-space Occam inversion algorithm was applied to the 2D ERT inversion algorithm. In the model approach, the size of the system of equations that must be solved from $M \times M$. The data-space approach transforms the size of the system of equations from $M \times M$, to $N \times N$, where N and M are the numbers of data and model parameters, respectively. The number of model parameters is frequently larger than the data number for the 3D CSEM inversion. I applied the data-space approach to a 3D CSEM Occam inversion algorithm to reduce CPU time and memory.

Numerical tests were conducted to determine the ability of how the inversion algorithm of the deep-towed ERT systems can map SMS deposits. The results showed the inversion algorithm of the ERT data with 180 m cable length can image SMS deposits placed up to a depth of 45 m below the seafloor. With 360 m cable length, the inversion algorithm can image SMS deposits placed up to a depth of 75 m below the seafloor. However, the attitude of the longer cable easily becomes unstable, causing large navigation errors. Here, I focus on a CSEM survey consisting of a towed transmitter and stationary receivers on the seafloor for the deeper penetration depth. The performance of the developed CSEM inversion algorithm was investigated using synthetic data. The results showed the CSEM inversion algorithm sufficiently recovered 3D conductive anomaly simulating SMS. The inversion algorithm also imaged deeply buried resistive anomalies simulating oil reservoirs.

The fourth chapter consists of the application of the developed inversion algorithm of the 2D marine ERT survey to observed data in the Iheya North hydrothermal field, mid-Okinawa Trough. The high-resolution images of near-seafloor resistivity structures to a depth of 50 m depth with a spatial resolution of 10 m were obtained. The resistivity image by the inversion analysis revealed that the highly conductive zones below the seafloor were consistent with observed hydrothermal venting sites and heat anomalies. This high conductivity is probably attributable to rich conductive SMS minerals, not only to high-temperature fluids, clay minerals, and salinity of pore fluids. The resistivity cross-section indicates a semi-layered structure consisting of exposed and deeply embedded SMS deposits. The cap rock layer is also inferred from a seismic reflection survey and seafloor drillings. The integration of all results suggests a possible generation mechanism of SMS deposits. Hydrothermal fluids migrate from deep parts to the seafloor. They are captured by the cap rocks, where lower SMS deposits are generated below the seafloor. Fluids passing through fractures in the cap rocks to the seafloor develop the upper SMS deposits on the seafloor. The study represents the first reported success in imaging a semi-layered structure of SMS deposits although the layered structures were also proposed by seafloor drillings.

The fifth chapter consists of the application of the developed inversion algorithm of the 3D marine CSEM survey to observed data in the Ieyama hydrothermal field, mid-Okinawa Trough. A 0.125 Hz square wave current of approximately 60 A was transmitted through the dipole antenna. Six stationary receivers on the seafloor recorded the coupled CSEM signals. By applying the developed inversion algorithm to the observed data, a 3D resistivity model was imaged. It is obvious that resistivity structures in the hydrothermal field exhibit 3D features. Thus, the 3D inversion could estimate the resistivity structures more accurately than 1D or 2D inversion algorithms. Low resistivity anomalies with resistivity of 0.1-0.2 Ohm-m were recovered just below the seafloor. The self-potential anomalies and hydrothermal vents were observed around the conductive anomalies. The conductive anomalies might be associated with SMS mineralization.

The sixth chapter consists of a discussion on generation mechanisms of SMS based on resistivity structures obtained in chapters four and five. Hot fluids upwell from the deep below the seafloor. The impermeable cap layer traps the path of the hot fluids. Below the cap layers, the SMS accumulates.

The final chapter consists of conclusions and the future outlook of the thesis.

Key words: Controlled source electromagnetic / Electrical resistivity tomography / Inversion / Resistivity / Seafloor massive sulfide deposits

要旨

本論文では，海底熱水鉱床の分布調査のために，海底下浅部から深部まで網羅した比抵抗構造をイメージングできる電気及び電磁データ逆解析技術の開発を行った。具体的には，二次元曳航式 electrical resistivity tomography (ERT) データ逆解析法と三次元 controlled source electromagnetic (CSEM) データ逆解析法の開発を行った。曳航式ERT法では，送受信機を共に曳航することで，水平方向に密なデータを取得できる。そのため，二次元曳航式ERTデータ逆解析法により, 海底下浅部の高解像度二次元比抵抗構造のイメージングが可能である。一方，CSEM法では，曳航された送信機からの電磁場応答を海底面に設置された受信機で観測することで，様々な送受信配置データを取得可能である。そのため，三次元CSEMデータ逆解析法により，海底下深部までの三次元比抵抗構造のイメージングが可能である。開発した二次元曳航式ERT法逆解析法を，沖縄沖伊平屋北海丘熱水域で得られた実データに適用した結果，海底熱水鉱床が海底面直下と海底面下40 mに存在する二階建て構造を可視化できた。また，開発した三次元CSEMデータ逆解析法を，沖縄沖伊江山熱水域で得られた実データに適用した結果，海底下数百mまでの三次元比抵抗構造を推定できた。これらの結果より，二次元曳航式ERTデータ逆解析法と三次元CSEMデータ逆解析法の二つを組み合わせることで, 海底下浅部から深部まで網羅した比抵抗構造の可視化が可能であることを示した。

第一章は，本論文の緒論である。近年，世界的な金属需要から海底熱水鉱床への注目が高まっている。海底熱水鉱床は，日本の排他的経済水域内でも発見されており，特に金属を輸入に頼る日本では，その開発に向けて様々な調査を行っている。海底熱水鉱床の分布調査には，地震探査，重力探査，電気・電磁探査などの様々な物理探査手法が用いられてきた。本研究では，海底熱水鉱床の比抵抗構造を取得できる電気・電磁探査に着目する。海底熱水鉱床の比抵抗は，周りの基盤岩に比べて非常に小さいため，電気・電磁探査が，その分布調査に有効である。例えば，大西洋中央海嶺で行われた電磁探査によって，低比抵抗異常域と海底熱水鉱床の分布が一致するという結果が得られた。その他にも電磁探査が，海底熱水域で鉱床の分布調査のために行われてきた。しかしながら，これまで得られた比抵抗構造の解像度は限られており, 海底下浅部から深部まで網羅した比抵抗構造は得られていない。そのため，海底熱水鉱床の分布は，これまで明らかとなっていない。そこで，本論文では，二次元曳航式ERTデータ逆解析法と三次元CSEMデータ逆解析法を用いた海底下浅部から深部まで網羅できる比抵抗構造イメージング技術を開発し，海底熱水鉱床の詳細な分布を明らかとする。

第二章では，二次元曳航式ERT法と三次元CSEM法の順解析について述べる。二次元曳航式ERT法では，海底下浅部の詳細な比抵抗構造を推定するため，海底地形をできる限り現実に近く再現する必要がある。そこで，非構造格子を用いた有限要素法による順解析を行うことで，海底熱水域での複雑な海底地形を正確に表すことを可能とした。本順解析によって計算されるレスポンスを，一次元層構造モデルでの解析解と比較した結果，十分な精度が得られ

ていることを示した。一方，三次元CSEM法順解析では，Yee六面体格子を用いた有限差分法により，離散化を行った。更に，送信点近傍での特異点問題を回避するため，電場を一次場と二次場に分解して計算を行った。三次元順解析では，二次元順解析に比べて解くべき線形システムが莫大に大きくなるため，効率的な数値計算法が必要である。本論文では，並列計算疎行列直接法ソルバーPARDISOを用いて線形システムを解くことで，現実的な計算時間で順解析を実行可能とした。CSEM法順解析においても，計算されるレスポンスを一次元層構造モデルからの解析解，及び三次元石油貯留層モデルからの参照レスポンスと比較した結果，送受信距離10 km程度まで十分な精度が得られていることが示された。

第三章では，二次元曳航式ERTデータ逆解析法と三次元CSEMデータ逆解析法について述べる。両逆解析法ともに，安定して海底下比抵抗構造を推定できるOccamアルゴリズムを採用した。二次元ERTデータOccam逆解析では，モデルを更新する際に解くべき線形システムのサイズが，$M \times M$ であるモデルスペース法を用いた。M は，モデルパラメータ数を示す。一方，三次元CSEMデータ逆解析法では，モデルパラメータ数が，データ数に比べて格段に多い。そこで，データスペース法を逆解析に適用することで，解くべき線形システムを $N \times N$ に変換し，計算量を大幅に削減した。N は，データ数を示す。

仮想データを用いた数値実験により，二次元曳航式ERTデータ逆解析法の海底下比抵抗構造の可視化能力の評価を行った。その結果，曳航ケーブル長が180 mの場合，海底面下45 mより浅く存在する低比抵抗異常体を可視化できることが明らかとなった。更に，ケーブル長を360 mまで伸ばした場合，海底面下75 mまでの低比抵抗異常体を可視化できることが明らかとなった。しかしながら，長いケーブルを用いると形状が安定しないため，曳航中にその形状をモニタリングする必要がある。そこで，長いケーブルを用いる必要がなく，海底下深部まで探査深度を稼ぐことができるCSEM法データ逆解析法に注目する。三次元CSEMデータ逆解析法の海底下比抵抗構造の可視化能力評価のため，仮想データを用いた数値実験を行った。その結果，三次元CSEMデータ逆解析法は，海底下浅部に存在する三次元的分布をする海底熱水鉱床を模した低比抵抗異常体を高解像度で再現できた。また，本逆解析を海底下深部に存在する石油貯留層を模した低比抵抗異常体を含むモデルに適用した結果，石油貯留層も十分に再現できることが数値実験により示された。

第四章は，伊平屋北海丘熱水域での観測された曳航式ERT実データへの適用について述べる。観測された見かけ比抵抗データを逆解析法に適用することで，海底下50 mまでの二次元比抵抗構造を10 m程度の空間解像度で推定することができた。この比抵抗構造により，0.2 Ohm-m程度の低比抵抗異常体が，海底面直下と海底面下40 mに存在する二層構造をしていることが明らかとなった。岩石モデルや他情報を組み合わせて低比抵抗異常を解釈した結果，その異常体は，熱水や粘土の存在だけでなく，硫化鉱物の存在に由来すると考えられる。更に，その異常体が確認された近傍で，熱水噴出孔や高熱流量が観測されている。この比抵抗構造に基づいて，新たな海底熱水鉱床の形成メカニズムを提案した。そのメカニズムでは，海底下深部から熱水が上昇し，その熱水が帽岩により流れが規制された結果，帽岩下で硫化鉱物が

蓄積し，その帽岩を通り抜けた熱水が海底面で冷やされ海底面で硫化鉱物が蓄積するというものである。このような海底熱水鉱床の二層構造は，掘削により提案されていたが，比抵抗構造により可視化されたのは世界初の成果である。

第五章は，伊江山熱水域での観測されたCSEM実データへの適用について述べる。0.125 Hzの矩形波をダイポールアンテナから送信し，海底面に設置された六台の受信機でCSEMデータを観測した。開発した三次元CSEMデータ逆解析法をその実データに適用した結果，海底熱水域での三次元比抵抗構造の推定に成功した。海底熱水域では，三次元的比抵抗構造を示すのは明らかであり，一次元や二次元逆解析法に比べて，高精度に比抵抗構造を推定できた。その結果，0.1~0.2 Ohm程度の低比抵抗異常域が海底面直下に再現され，この異常域の近傍で海底熱水噴出孔，自然電位異常も確認された。そのため，この異常域は，熱水が冷やされる過程で蓄積した硫化鉱物を含むと考えられる。

第六章は，第五章及び第六章で推定された比抵抗構造を基づいて海底熱水鉱床の発達メカニズムを議論する。その結果，熱水が上昇し，その熱水の流れが帽岩により規制され水平方向にながれることによって，水平に伸びた硫化鉱物層が発達することが共通して考えられる。

第七章では，本論文の結論である。得られた結果をまとめる。

キーワード：電磁探査・電気探査・逆解析・比抵抗・海底熱水鉱床

Publications

1. **Ishizu, K.**, Vachiratienchai, C., Siripunvaraporn, W., Goto, T., Kasaya, T. & Iwamoto, H. (2019), Evaluations of effectiveness of marine deep-towed DC resistivity survey in investigation of seafloor massive sulfide deposits. *Geophysical Exploration*, **72**, 122–138 (in Japanese). https://doi.org/10.3124/segj.72.122
2. **Ishizu, K.**, Goto, T., Ohta, Y., Kasaya, T., Iwamoto, H., Vachiratienchai, C., Siripunvaraporn, W., Tsuji, T., Kumagai, H. & Koike, K. (2019), Internal structure of a seafloor massive sulfide deposit by electrical resistivity tomography, Okinawa Trough. *Geophysical Research Letters,* **46**, 11025–11034. https://doi.org/10.1029/2019GL083749
3. Okamoto, T., Goto, T., Kasaya, T., Teranishi, Y., **Ishizu, K.**, Inamori, T., Abe, S. & Takai, K. (2020), Technological development and challenges for the advancement of 3D marine CSEM survey. *Journal of the Japanese Association for Petroleum Technology*, **85**, 54–61 (in Japanese).
4. **Ishizu, K.**, Siripunvaraporn, W., Goto, T., Koike, K., Kasaya, T. & Iwamoto, H. Development of a data-space Occam inversion for 3D marine controlled-source electromagnetic survey data to explore seafloor massive sulfide deposits. (submitted to *Geophysical Journal International*).

Proceedings

5. **Ishizu, K.**, Vachiratienchai, C., Siripunvaraporn, W., Goto, T., Kasaya, T. & Iwamoto, H. (2017), Two-dimensional inversion of marine DC resistivity using fuzzy c-means clustering constraint. 87th Annual International Meeting, SEG, Expanded Abstracts, 1204–1208. https://doi.org/10.1190/segam2017-17729696.1
6. Goto, T., **Ishizu, K.,** Vachiratienchai, C., Siripunvaraporn, W., Kasaya, T. & Iwamoto, H. (2018), How are seafloor ore deposits produced at an active hydrothermal field?-Implication from marine DC resistivity survey in Okinawa Trough, Japan. The 13th SEGJ International Symposium, 180–181. https://doi.org/10.1190/segj2018-048.1

Acknowledgements

I would like to thank my supervisors Prof. Katsuaki Koike, Prof. Tada-nori Goto and Prof. Weerachai Siripunvaraporn for their constructive advice and continual encouragement throughout my studies. Prof. Koike shared valuable knowledge of geophysics, geology, and geochemistry. Much of the knowledge gave me new insights into my research on electromagnetic exploration. Particularly, his geological feedbacks on my research were very critical. The feedbacks helped me have a good balance between geophysics and geology. Prof. Goto invited me to geophysical researches and has provided me with countless hours of his time on my research. He gave me the opportunity to present my work on many conferences and join in various field surveys. He kindly revised not only my research papers but also my application forms of research funds such as JSPS Research Fellow DC1. I am grateful to him for making time to visit the Katsura campus for our research discussions. Prof. Siripunvaraporn generously hosted me at Mahidol University in 2018 for a year. He shared valuable knowledge of 3D electromagnetic modeling and inversion algorithms, which has benefited me greatly. Without his feedbacks, I could not make a 3D inversion code during my Ph.D. period. I very much enjoyed the life in Bangkok because of the support from him and his students. Besides my supervisors, Dr. Takafumi Kasaya and Dr. Hisanori Iwamoto gave me a great opportunity for joining in cruise surveys of JAMSTEC. I would like to thank them for kindly hosting me in the surveys and providing me the electromagnetic data set. I could learn practical data acquisition, which inspired my modeling work. I am grateful to Prof. Hitoshi Mikada and Prof. Koki Kashiwaya for their constructive comments and suggestions on my thesis. I thank Ms. Ai Watanabe for supporting me through many administrative tasks. I could work smoothly because of her help. I also thank Prof. Taiki Kubo and all members of the E.G.E group for their support on my thesis. I would like to deeply thank my parents for supporting me during Ph.D. life. They understood me and generously provided me financial supports. When I came back to my hometown, they always welcomed me with tasty food. I could not keep conducting my research without their help. My research was financially supported by JSPS Research Fellow DC1 (Grand number 17J08764).

Chapter 1

Introduction

1.1 Research background

A Stable supply of metal is critically important for various industries. Global demands for metal increase interest in mining of seafloor metal deposits because profitable deposits on land are becoming more difficult to find. For the hydrocarbon resources, offshore oil and gas reservoirs have been developed commercially. Global offshore oil production including lease condensate and hydrocarbon gas liquids in 2015 was at the highest level since 2010 and accounted for nearly 30% of total global oil production (U.S. Energy Information Administration 2015). Development of the seafloor metal resources also has great potential for contributing to global metal supplies.

The most profitable seafloor metal resources are SMS deposits containing Cu, Sn, Zn and potentially traces of Ag and Au. SMS deposits have been formed through hydrothermal circulation generally located near mid-ocean ridges and along submarine volcanic arc and back-arc spreading centers (Hannington *et al.* 2011, Boschen *et al.* 2013). SMS deposits in Japan were found in the mid-Okinawa Trough and Izu-Ogasawara Arc (Iizasa *et al.* 1999). Toward the future development of SMS deposits, Japan Oil, Gas and Metals National Corp. (JOGMEC) achieved consecutive lifting of ore and seawater in a state of solid–liquid flow from approximately 1,600 m depth during mid-August through the end of September 2017 (Yamaji *et al.* 2019).

A map of the internal structures of a seafloor hydrothermal system provides a key to elucidating the SMS deposit generation mechanisms. In past studies, seafloor drilling surveys have been conducted for the lithological studies of SMS deposits. One of the best-studied hydrothermal areas is the TAG hydrothermal field in the mid Atlantic Ocean . The Ocean Drilling Program revealed a lens-shaped ore body beneath the mound and an underlying upflow zone through the volcanic rocks that host the deposit (Humphris *et al.* 1995, Petersen *et al.* 2000). Other hydrothermal fields such as in the Iheya North Knoll (Expedition 331 Scientists 2010) and Palinuro Seamount (Petersen *et al.* 2014) were also investigated using boreholes. Tornos *et al.* (2015) compiled existing information of SMS deposits and proposed various models of SMS mineralization. However, the generation mechanisms of SMS remain unclear because of a lack of detailed images of SMS deposits. Although seafloor drilling is a powerful tool, its use is limited because it entails high costs. Even if numerous drillings are conducted, geophysical images have been requested to fill gaps among boreholes.

Various efforts to image and estimate SMS deposits have been undertaken using geophysical methods. Electrical and EM geophysical surveys are suitable for mapping the distribution of SMS deposits because the deposits show lower resistivity than the surrounding host rocks. Spagnoli *et al.*

(2016) reported SMS samples generally have resistivity in range from 0.01 to 1.0 Ohm-m whereas surrounding basaltic host rock have conductivity values in the order of a few Ohm-m. The substantial resistivity contrasts make EM surveys ideal for the exploration of SMS deposits.

Pilot EM surveys for the SMS deposits were conducted in the TAG mounds for investigating resistivity structures of SMS deposits (Cairns *et al.* 1996, Von Herzen *et al.* 1996). Cairns *et al.* (1996) and Von Herzen *et al.* (1996) used a time-domain EM survey and DCR sounding surveys, respectively. They found that anomalous low resistivity zones (about 0.2 Ohm-m) are associated with SMS deposits. Kowalczyk (2008) investigated shallow seafloor resistivity structures using the time-domain EM method with ROV at the Solwara site offshore Papa New Guinea. Its subsequent drilling surveys confirmed that the recovered low resistivity zone was associated with occurrences of SMS. However, the penetration depth is a few meters below the seafloor.

Recent global attention on SMS deposits drives new development of EM survey systems for imaging SMS deposits. Haroon *et al.* (2018) and Gehrmann *et al.* (2019) used a towed CSEM transmitter (DASI, Sinha *et al.* 1990) and a towed receiver (Vulcan, Constable *et al.* 2016) for the exploration of SMS deposits in the TAG mound. They obtained resistivity sections by applying a 2D EM inversion code (MARE2DEM, Key 2016) to observed data. They found low resistive zones immediately beneath the seafloor with greater than 50 m thickness. These towed CSEM surveys achieved both deeper penetration depth (~300 m) and dense spatial measurements. However, they had low sensitivity to near-seafloor structures because of the limited number of receivers and their survey configuration. Other new surveys have deeper penetration to tens to hundreds of meters (Safipour *et al.* 2017, 2018, Constable *et al.* 2018, Imamura *et al.* 2018, Müller *et al.* 2018). However, the measurements should be done as stationary (with the fixed source, receivers, or both) lacking dense spatial samplings. In fact, high-resolution images of near-seafloor resistivity structures in hydrothermal areas (*e.g.* to 50 m depth with a spatial resolution of 10 m) have never been reported even though such imaging is necessary to discuss the evolution mechanisms of SMS deposits attributable to high spatial heterogeneities that have been inferred from drilling studies.

SMS deposits are often associated with mound structures and complex bathymetry. These environments make resistivity structures in the area of SMS 3D. If the 2D CSEM inversion algorithms are used for imaging SMS, the 2D resistivity section possibly has several artifacts due to its 3D resistivity effects (Haroon *et al.* 2018). 3D CSEM inversion algorithms are necessary to more precisely recover resistivity structures of SMS deposits. 3D resistivity images can provide information on the volume and the tonnage of SMS deposits. The volume information is useful for estimation of resource potential of SMS deposits. However, 3D inversion algorithms have not been applied to CSEM data for imaging of SMS.

Drilling surveys revealed that some SMS are buried at a depth of about 100 m below the seafloor (Takai *et al.* 2015). The deeply buried SMS are not extensively oxidized and eroded at the seafloor and therefore have had a high likelihood of being preserved (Doyle & Allen 2003, Tornos 2006). Hydrothermal reservoirs can be at a depth more than a few hundred meters below the seafloor. The reservoirs play a key role in SMS generation. The reservoirs for hot fluids can be imaged as low resistivity anomalies. Therefore, deep resistivity structures in hydrothermal fields are useful for the reveling the reservoirs and its associated buried SMS. However, the resistivity structures covering deep resistivity structures in hydrothermal fields have not been reported.

1.2 Problem statement

The four main problems overcame in this thesis are summarized as follow:

i) High-resolution resistivity images of near-seafloor structures in hydrothermal areas (*e.g.* to 50 m depth with a spatial resolution of 10 m) have never been reported even though such imaging is necessary to discuss the evolution mechanisms of SMS deposits attributable to high spatial heterogeneities that have been inferred from drilling studies.

ii) 3D inversion algorithms have not been applied to CSEM data for imaging of SMS although 2D inversion algorithms have limitations to recover 3D resistivity structures of SMS. 3D resistivity images can provide information on the volume and the tonnage of SMS, which is necessary for estimation of resource potential of the deposits.

iii) The resistivity images covering deep structures in hydrothermal fields have not been reported although the reservoirs and its associated buried SMS can be located at a depth of more than 100 m below the seafloor.

iv) Due to lack of detailed images covering shallow and deep resistivity structures in hydrothermal fields, generation mechanisms of SMS remain unclear.

1.3 Purpose of this thesis

The purpose of this thesis is to develop an inversion algorithm of 2D marine ERT and 3D CSEM surveys for obtaining detailed resistivity images covering shallow and deep structures in seafloor hydrothermal fields and to investigate generation mechanism of SMS deposits using the detailed resistivity images in hydrothermal fields.

1.4 Approach to address the problem

To investigate shallow and deep resistivity structures in hydrothermal fields, I develop a resistivity imaging technique using an inversion algorithm of 2D marine ERT and 3D CSEM surveys. The marine deep-towed ERT system is used to obtain a 2D high-resolution resistivity image of the shallow seafloor structures. The system tows the transmitter and eight electrode pairs of receiver for increasing resolution to shallow structures while the towed CSEM system used in Haroon *et al.* (2018) and Gehrmann *et al.*

(2019) consisted of only two receivers. This survey system was developed first for detecting shallowly existing gas hydrate (Goto *et al.* 2008, Chiang *et al.* 2012). A CSEM survey consisting of a towed transmitter and stationary receivers on the seafloor is used for investigating deep resistivity structures. This configuration has been widely used to image deeply buried hydrocarbon reservoir (Constable 2006). Data recorded at various combinations between transmitter and receiver can be obtained in this configuration. 3D CSEM survey data set is also easily obtained. Longer offset data generally have deeper penetration depth and vice versa. It is necessary to consider Maxwell equation to compute accurately CSEM data at longer offset because the EM fields attenuate rapidly.

I develop a forward modeling scheme (*Chapter 2*) and inversion algorithm (*Chapter 3*) of the 2D towed marine ERT survey for investigating shallow resistivity structures below the seafloor. The ERT data was collected in the Iheya North hydrothermal field, mid-Okinawa Trough, southwestern Japan. A hydrothermal area discovered on the Iheya North Knoll in 1995 has since been investigated intensively (Nakagawa *et al.* 2005, Takai *et al.* 2006, Kumagai *et al.* 2010, Masaki *et al.* 2011, Tsuji *et al.* 2012, Kasaya *et al.* 2015, Miyoshi *et al.* 2015). The accumulated survey data indicate this area is suitable for the detailed imaging of SMS deposits. I apply the developed inversion algorithm to observed ERT data and present a new evolution mechanism of SMS deposits (*Chapter 4*).

I develop a forward modeling scheme (*Chapter 2*) and an inversion algorithm (*Chapter 3*) of the 3D marine CSEM survey for investigating deep resistivity structures below the seafloor. 3D inversion algorithms of the marine CSEM survey require great computational resources due to a huge number of model parameters. Efficiency is key for 3D CSEM inversion algorithms. A robust and efficient 3D inversion algorithm is the data-space Occam algorithm (Siripunvaraporn *et al.* 2005). The data-space approach transforms the size of the system of equations that must be solved from $M \times M$, as required for a model-space approach (Constable *et al.* 1987), to $N \times N$, where M and N respectively denote the quantities of model and data parameters. M is frequently larger than N for the 3D CSEM inversion (*e.g.* M=2,463,768 and N=16,088 in Wang *et al.* 2018). The data-space approach can reduce both CPU time and memory if $M < N$. I develop a data-space Occam inversion algorithm for 3D CSEM survey data, 3D Data-space Occam inversion algorithm for CSEM survey data (3DDOCSEM) and to apply for clarification of the 3D resistivity structure in the Ieyama hydrothermal field, mid-Okinawa Trough (*Chapter 5*).

I develop an combined CSEM inversion algorithm of towed and ocean-bottom electric field receiver data to investigate shallow and deep resistivity structures in hydrothermal fields (*Chapter 3*). Here, I treat deep-towed ERT data as CSEM data by considering Maxwell equation. Actually, transmitted current of the ERT system is a low-frequency square wave. Thus, electric fields are more precisely computed by considering Maxwell equation. A marine CSEM inversion combining towed and ocean-bottom electric field receiver data recovered 2D high-resolution resistivity structures of gas hydrate (Attias *et al.* 2018). I will show ability of the inversion of towed and ocean-bottom electric field receiver data for recovering shallow and deep resistivity structures using synthetic data.

1.5 Outline of SMS deposits

SMS deposits are considered to be the modern analogous of ancient VMS deposits preserved on land (Murton *et al.* 2019). These SMS deposits consist of relatively insoluble sulfide minerals, *e.g.*, pyrite (FeS2), chalcopyrite (CuFeS2), sphalerite (ZnS), and galena (PbS), and also contain trace elements such as Au, Ag, Co (Herzig & Hannington 1995). Their high metal concentrations can meet the global demand for metal resources. Therefore, SMS deposits are attractive for next-generation mining (Lipton 2012). Recent estimates, using bulk geochemical data from 95 sites, suggest a global resource potential for modern SMS deposits is at least 650 million tons with a median grade of 3 wt % Cu, 9 wt % Zn, 2 g/t Au and 100 g/t Ag (Hannington *et al.* 2011, Monecke *et al.* 2016). Fig. 1.1 shows a photograph of SMS mound taken during YK15–06 cruise survey JAMSTEC in mid-Okinawa Trough. Hydrothermal vents on the mound emit fluids which disperse as neutrally buoyant plumes.

Figure 1.1. Photograph of SMS taken by JAMSTEC during YK15–06 cruise survey in mid-Okinawa Trough.

1.5.1 Distribution

Since the first discovery of hydrothermal activity in the Red Sea (Miller *et al.* 1966) and near the Galapagos Islands in 1977 (Corliss *et al.* 1979), there are 165 recorded SMS deposits (Hannington *et al.* 2011, Monecke *et al.* 2016). 60% of all deposits occur at mid-ocean ridges and 27% in back-arc basins along the 67,000 km length of seafloor spreading centers. Only 13% of deposits are found along the 22,000 km of active submarine volcanic arcs and very few (<1 %) have been found at hotspot volcanoes, such as Hawaii (Hannington *et al.* 2011, Monecke *et al.* 2016). Fig. 1.2 shows the global distribution of

SMS deposits. Hydrothermal activity and its associated SMS deposits have been found in Japan. They are distributed along mid-Okinawa Trough basin and Izu-Ogasawara Arc.

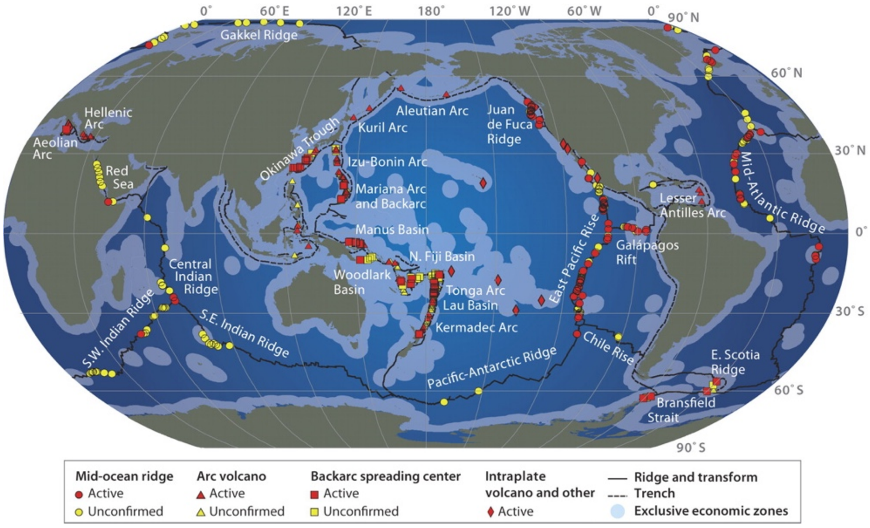

Figure 1.2. Global distribution of seafloor hydrothermal systems and related mineral deposits, after Hannington *et al.* (2011).

1.5.2 Formation

Hydrothermal circulation below the seafloor is a process of heat and material exchange between seawater and the crust (Stein & Stein 1992). Such seafloor hydrothermal systems often have accompanying SMS deposits, form as a consequence of the interaction of seawater with hot oceanic crust deep beneath the seafloor. During this process, cold seawater penetrates through cracks in the seafloor, reaching depths of several kilometers, where it is heated to temperatures over 400°C (Petersen *et al.* 2018). This hot fluid leaches the surrounding rocks and becomes strongly enriched in dissolved metals and sulfur. Due to its lower density, this heated mineral-rich fluids rise to the seafloor. The heated mineral-rich fluids mix with low-temperature (0°C) and alkalescent seawater (pH~8) on the seafloor. Accumulation of metals occurs due to the decline of solubility of metal caused by mixing with seawater. SMS mineralization has two representative types of **(1)** mound-style mineralization and **(2)** sub-seafloor replacement.

(1) Mound-style mineralization: Mound-style mineralization is the most common among found SMS mineralization. The vast majority of metal sulfides accumulate via the growth, collapse, and cementation of chimneys and spires and not by the fallout of sulfide particles precipitated in the water column (Rona 1988, Herzig & Hannington 1995). Most of the SMS deposits on the mound have not been preserved, likely due to oxidation of the sulfides in the prevailing oxic environment and/or destruction of oceanic crust during subsequent subduction (Tornos *et al.* 2015).

(2) Sub-seafloor replacement: Systematic drilling of the seafloor at several mineralized sites has shown that sub-seafloor hydrothermal replacement processes contribute to SMS mineralization (Herzig & Hannington 1995, Zierenberg *et al.* 1998). Similarly, recent drilling in the Iheya North Knoll in the middle Okinawa Trough has shown that from 40.0–50.0 mbsf, gray highly altered brecciated volcanic rock fragments are partly (15%) replaced by fine-grained sphalerite, chalcopyrite, and galena (Takai *et al.* 2015). Deposits formed in this way are not extensively oxidized and eroded on the seafloor and therefore have had a high likelihood of being preserved (Doyle & Allen 2003, Tornos 2006).

1.5.3 Exploration

The area of the world ocean is about 361.9 million km^2, which covers about 70.9% of Earth's surface. The scale of SMS deposits is much smaller (*e.g.* the TAG active mound is a circular feature, about 200 m in diameter and about 50 m high). Therefore, highly efficient surveys are required to identifying the potential area for SMS deposits. In the marine environment, all surveys use a ship. The following five phases of the survey are used for identifying the area for SMS deposits (Fig. 1.3).

(1) Selection of region (narrowing area from 361,000,000 km^2 to 10,000 km^2): Based on the genesis of SMS deposits, regions to be investigated are determined. Magmatic activities are essential for forming SMS deposits.

(2) Regional survey with a ship (narrowing area from 10,000 km^2 to 100 km^2): In this stage, a 10 m spatial resolution bathymetry map is obtained by a hull-mounted MBES. MBES can also obtain acoustic water column anomalies caused by exposed hot water from hydrothermal vents. Key evidences of forming ore deposits are the existence of i) a depression, ii) sediment and permeable pumice in depression, iii) a long term active hydrothermal field. Based on the obtained bathymetry map, an area with depression and fault structures with hydrothermal activity are identified.

(3) Semi-detailed survey with AUV and deep-towed system (narrowing area from 100 km^2 to 10 km^2): More high-resolution bathymetry map is obtained with AUV. Mounting sensors on AUV and deep-towed systems can record various data near the seafloor just above a few tens of meters. Temperatures and pH of seawater are often measured to identify local anomaly of seawater. Self-potential method is an quick reconnaissance tool to find SMS on the seafloor and buried SMS below the seafloor. Field surveys conducted in known SMS areas showed negative self-potential data are sensitive to the existence of SMS (Kawada & Kasaya 2017). Self-potential data is easy to be measured and analyzed. Electrodes to measure self-potential can be mounted on either AUV and deep-towed system.

To delineate distributions of SMS deposits, geophysical exploration are performed such as electric (Von Herzen *et al.* 1996), EM (Cairns *et al.* 1996), seismic (Asakawa *et al.* 2016), magnetic susceptibility (Honsho *et al.* 2013), and density (Evans 1996). In this thesis, I focus on electric and EM surveys using a deep-towed system, equivalent to semi-detailed surveys. Resistivity images are used for mapping the spatial distribution of both SMS on the seafloor and buried SMS below the seafloor.

(4) Detailed survey with ROV: The narrowed areas are further investigated by local-scale geophysical exploration and sampling of rocks with ROV. For the EM surveys, TEM with ROV has been used to map resistivity structures whose spatial resolution is a few meters (Nakayama & Saito 2016, Safipour *et al.* 2017). Rock samples from the seafloor can be brought back to ship using ROV. Information obtained from measurements of mineral contents and physical parameters of rock samples constrain the interpretation of resistivity structures.

(5) Drilling survey: Drilling surveys have been used for investigating internal structures of SMS deposits (Humphris *et al.* 1995, Expedition 331 Scientists 2010). Although its use is limited to the high cost, the drilling surveys are a very powerful tool to investigate SMS deposits. To reduce the number of drilling holes, the resistivity images can be used for ranking the priority zones of drillings. After the drilling, the resistivity structures can be used for estimating the detailed amount of SMS deposits combined with information obtained from the drilling data.

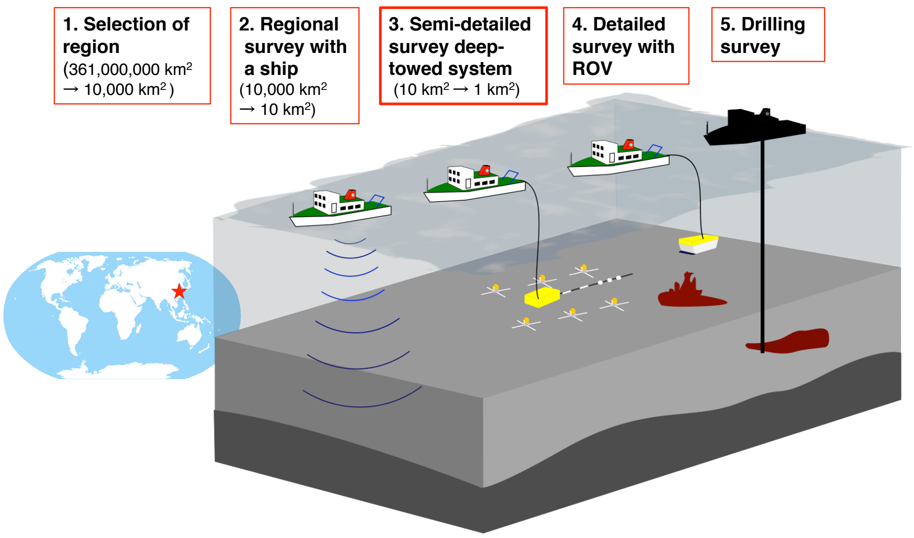

Figure 1.3. Schematic diagram of exploration of SMS deposits. The following five phases of surveys are used for identifying the area for SMS deposits.

1.6 Study area for SMS deposits

Since the first discovery of hydrothermal activity at Izena hole in Okinawa Trough, nine representative hydrothermal fields were found in the mid-Okinawa Trough (*i.e.* the Minami-Ensei knoll, the Yoron hole, the Iheya ridge, the Iheya North Knoll, the Izena hole, Irabu knoll, the Hatoma knoll, the Daiyon-Yonaguni knoll, and the Ieyama hydrothermal field). In this thesis, I focus on two hydrothermal fields of the Iheya North Knoll and the Ieyama hydrothermal field.

1.6.1 Okinawa Trough

The Okinawa Trough, to the southwest of Kyusyu, Japan, is an active backarc basin of the Ryukyu island arc–trench system where the Philippine Sea Plate is subducting under the Eurasia Plate (Fig. 1.4). The Okinawa Trough extends for more than 1,200 km from the Japanese mainland to Taiwan along the Ryukyu Arc. The Okinawa Trough is 60–100 km wide in the south and reaches up to 230 km wide in the north (Sibuet *et al.* 1998). Its maximum water depth approaches 2,300 m in the south and progressively decreases to 600 m in the north. The Okinawa Trough is interpreted to be still in the early stage of rifting (Letouzey & Kimura 1986). Magmatic activities occur in the center axis of the central and southern Okinawa Trough due to the back-arc rifting or a volcanic front. SMS associated with magmatic activity are also found in this area.

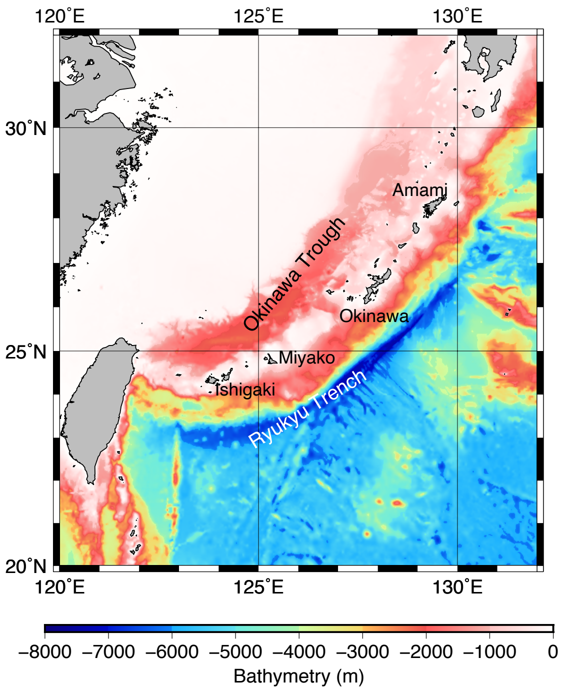

Figure 1.4. Map of the study area in mid-Okinawa Trough, southwestern Japan.

1.6.2 Iheya North Knoll hydrothermal field

The Iheya North Knoll is a volcanic complex located on the northern termination of the depression of the Okinawa Trough where water depths are about 1000 m. A seismic survey in the Iheya North Knoll hydrothermal field suggested presence of thick pumiceous volcaniclastic flow deposits below surficial hemipelagic sediments, rather than massive igneous rocks (Tsuji *et al.* 2012). About 10 hydrothermal mounds are concentrated in a small region aligned north to south (Kawagucci *et al.* 2011). Active fluid venting and sulfide mineralization are found in the mounds. A large mound of more than 30 m height called NBC host vigorous venting of clear fluid with the highest temperature of 311 °C. The high temperature hydrothermal flow have been recorded at NBC over a period of more than ten years (Kawagucci *et al.* 2013), indicating that the hydrothermal fluid vented from NBC comes from the main hydrothermal flow path in this region. Temperatures and flow rates of other vents in this region become lower with increasing distance from NBC (Masaki *et al.* 2011).

Three drilling programs (The IODP Expedition 331 and The SIP Expeditions 907, 908) were implemented to study hydrothermal system and internal structures of SMS in this field. Lithologies at the Iheya North Knoll field is a geologically complex mixed sequence of coarse pumiceous volcaniclastic and fine hemi-pelagic sediments, overlying dacitic to rhyolitic volcanic substrate (Yeats *et al.* 2017). Sulfide mineralization similar to the black ores in kuroko deposits of the Miocene age in Japan, were identified in the core drilled at the flank of the NBC mound (Expedition 331 Scientists 2010, Ishibashi *et al.* 2015). The drilling survey during the SIP Expeditions 907, CK 14–04 implies that the subseafloor structure of the Iheya-North Knoll was composed by multi-layers of hemi-pelagic sediment, acidic and neutral hydrothermally altered clay and sulfide mineral-bearing cap rock layers (Saito *et al.* 2015). The repeated occurrences of these layers detected by the CK 14–04 cruise survey strongly suggest that subseafloor hydrothermal fluids flow laterally along with upper and bottom cap rocks, possibly leading the formation of several layers-ore bodies observed at the Matsumine deposit that is the largest Kuroko-type VMS deposit in the Japanese Island (Kumagai *et al.* 2017).

The ERT data were collected during the YK 14–19 cruise survey (R/V Yokosuka, JAMSTEC) in the Iheya North Knoll hydrothermal field. I analyzed the observed ERT data and interpreted inverted resistivity structures with other geophysical data in *Chapter 4*. The accumulated survey data indicate this area as suitable for our detailed imaging of SMS deposits.

1.6.3 Ieyama hydrothermal field

A new hydrothermal field in mid-Okinawa Trough, southwestern Japan called Ieyama was found by a preliminary survey using a ship and a subsequent detailed survey using AUV (Kasaya *et al.* 2020). The detailed survey observed a clear negative self-potential zone and chimney structures in the hydrothermal field. Therefore, SMS formed through the hydrothermal activity are expected to be in the field. Resistivity images are required to evaluate the resource potential of SMS deposits in the fields. A CSEM survey was conducted in the Ieyama hydrothermal field during the KM 17–10 cruise survey (R/V Kaimei, JAMSTEC). The application of the inversion algorithm to the observed CSEM data is described in *Chapter 5*.

1.7 Electrical properties of rocks and minerals

Electrical conductivity measures a material's ability to conduct electrical current. Electrical resistivity is the inverse of electrical conductivity. Fig. 1.5 shows the range of electrical resistivity for various Earth materials varying over many orders of magnitude. The resistivity contrast can be used to elucidate the geological structure of the Earth's interior. Dry crystalline rock in the oceanic crust is electrically resistive. The bulk resistivity of seafloor rocks depends on pore fluids and the content of minerals. The highly porous rocks can make its bulk resistivity close to the resistivity of pore fluids. The resistivity of pore fluids decreases on the function of salinity and temperature (Keller 1988).

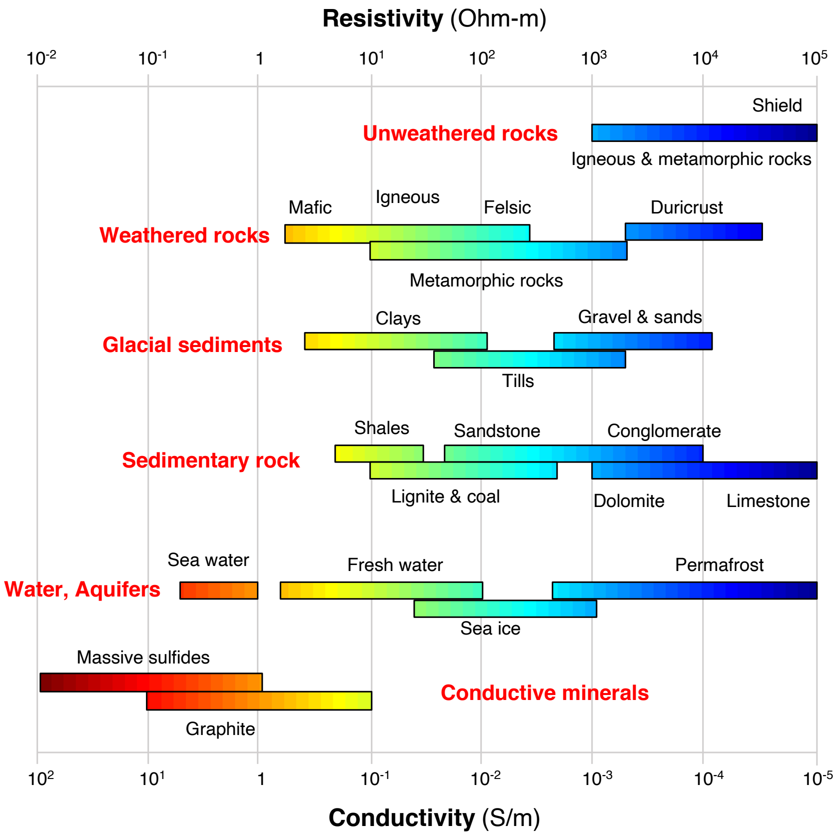

Figure 1.5. The electrical resistivity and conductivity values for various Earth materials. Resistivity is measured in units of Ohm meters (Ohm-m), conductivity in Siemens per meter (S/m). Values were taken from Palacky (1988) and references therein.

Laboratory measurement of SMS samples shows the resistivity is in a range from 0.01 to 1.0 Ohm-m whereas surrounding basaltic host rock has conductivity values in the order of a few Ohm-m (Spagnoli *et al.* 2016). Komori *et al.* (2017) also reported SMS samples collected in the Iheya hydrothermal fields in the Okinawa Trough exhibit much lower resistivity than the surrounding rocks. The substantial resistivity contrasts make electromagnetic surveys ideal for the exploration of SMS deposits. It is well known that most sulfide minerals, except for sphalerite, exhibit an anomalous signature of the induced polarization effect *i.e.* large imaginary conductivities and phase shifts (Pelton *et al.* 1978). Laboratory measurement of SMS samples shows SMS exhibit the induced polarization effect (Spagnoli *et al.* 2016, Komori *et al.* 2017).

1.8 Overview of applied geophysical method

I briefly describe the applied geophysical method for the exploration of SMS deposits. In the thesis, I use marine towed ERT and CSEM surveys to obtain resistivity structures in the hydrothermal fields.

1.8.1 Marine ERT survey

For ERT surveys, an electrical current is passed through two electrodes to produce an electrical potential field in the ground. The resultant voltages are then measured through other paired electrodes. The source current can be direct current or low-frequency (0.1-1 Hz) alternating current. The relationship between the resistivity, current and electrical potential is governed by Ohm's Law. Ohm's Law states the electric current through a material between two points is directly proportional to the potential difference between the two points. The spatial resistivity distribution in the subsurface is recovered by the inversion algorithm from the observed data.

ERT surveys are widely used for near-surface exploration on land such as underground water (Hermans *et al.* 2012, Afshar *et al.* 2015), metal deposits (Legault *et al.* 2008, Biswas & Sharma 2016), archeological items (Osella *et al.* 2005, Negri *et al.* 2008), and faults (Fuji-ta & Ikuta 2000, K. Suzuki *et al.* 2000). ERT surveys are also used for shallow water areas (Day-Lewis & Lane Jr 2004, Kwon *et al.* 2005, Allen & Merrick 2007, Mansoor & Slater 2007, Amidu & Dunbar 2008, Misonou *et al.* 2012) and even for deep water areas (Wynn 1988, Von Herzen *et al.* 1996). Goto *et al.* (2008) developed a deep-towed marine ERT system with multiple electrodes on cable. I use this deep-towed marine ERT system to map high-resolution resistivity structures to a depth of ~50 m below the seafloor (Fig. 1.6). The system affords high horizontal resolution by continuous towing of multiple electrodes, in addition to the simplicity of data acquisition and analysis.

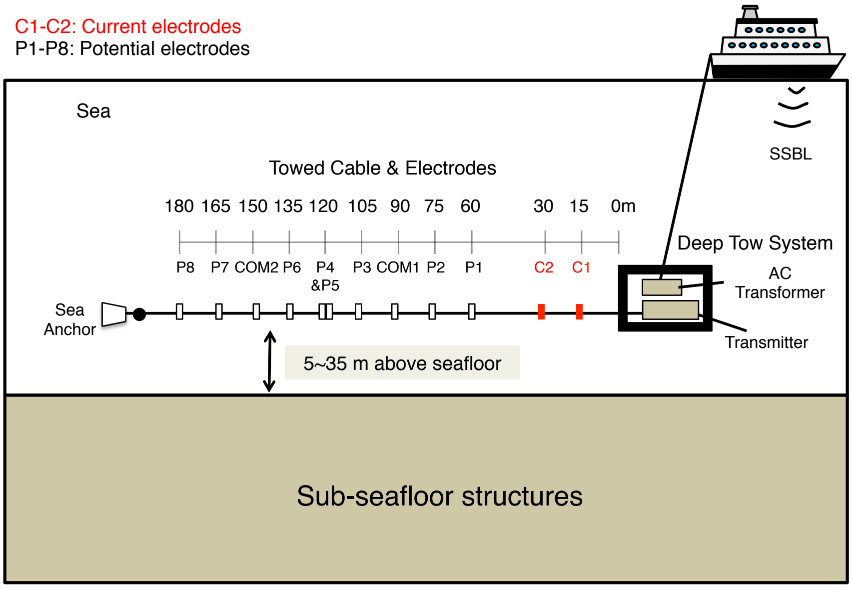

Figure 1.6. Schematic diagram of a deep-towed marine electrical resistivity tomography system developed by Goto *et al.* (2008). Two current electrodes C1 and C2 and eight potential electrodes P1–P8 are attached to the cable together with two reference electrodes COM1 and COM2. The voltage difference is measured using each 15-m dipole: P1–P2, P2–COM1, COM1–P3, P3–P4, P5–P6, P6–COM2, COM2–P7, and P7–P8. Acoustic transponders were attached respectively to the deep tow system and end of cable (a solid circle).

1.8.2 Marine CSEM survey

Marine CSEM surveys use a deep-towed transmitter to inject a time-varying current into the seawater. This electromagnetic signal diffuses away from the antenna, traveling through the ocean, seafloor, and air, where it is modified by the conductivity of each medium (Key 2012). The modified electromagnetic signal can be recorded by stationary receivers on the seafloor (Eidesmo *et al.* 2002) and towed receivers (Constable *et al.* 2016). The survey array with towed transmitters and the stationary receivers are often used for large-scale exploration. 3D CSEM data set can be easily obtained using the transmitter and receiver array. The CSEM surveys with the towed receivers have higher efficiencies of spatial coverage and resolution in the shallow sub-seafloor depth due to dense spatial measurements. The CSEM surveys with the towed receivers are used for near-seafloor exploration. CSEM surveys with the towed receiver have similar advantages to deep-towed ERT surveys. I focus on the CSEM surveys using stationary receivers on the seafloor to map deep resistivity structures below the seafloor (Fig. 1.7).

Marine CSEM surveys have been used for remotely mapping the seafloor resistivity structure with the goal of exploring hydrocarbons (Eidesmo *et al.* 2002, Yamane *et al.* 2009, Hesthammer *et al.* 2010, Myer *et al.* 2015), gas hydrate (Yuan & Edwards 2000, Schwalenberg *et al.* 2010, Weitemeyer *et al.* 2011, Zhdanov *et al.* 2014, Attias *et al.* 2016, Goswami *et al.* 2016), and SMS (Haroon *et al.* 2018, Gehrmann *et al.* 2019), and of elucidating oceanic lithosphere structures (Evans *et al.* 1994, MacGregor *et al.* 1998). Marine CSEM surveys also have been used with MT surveys for constraining resistivity structures of shallower crust (Blatter *et al.* 2019, Johansen *et al.* 2019).

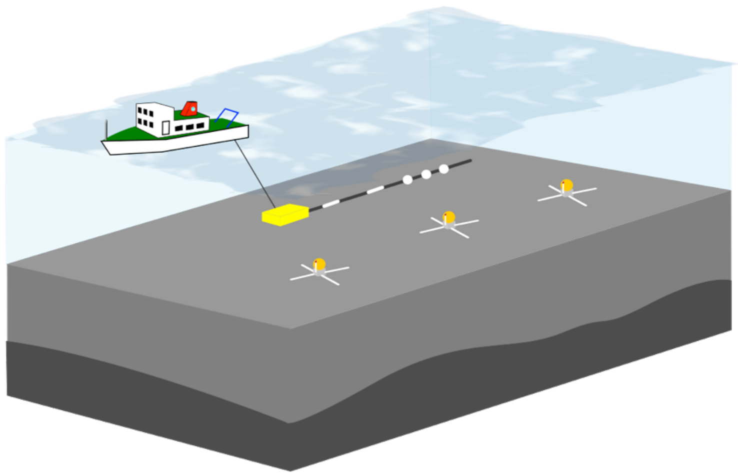

Figure 1.7. Schematic diagram of the marine CSEM surveys. The CSEM surveys use deep-towed dipole antenna for transmitting a time-varying current into the seawater. OBEM sensors deployed on the seafloor record the resultant EM responses for the CSEM surveys.

1.9 Thesis outline

The first chapter is devoted to the introduction. I describe the introduction of the thesis, introduction to SMS deposits, study fields, electrical properties of rocks and minerals, an overview of the applied geophysical method and thesis outline. The overview of the structures of this thesis is shown in a flow chart (Fig. 1.8).

The second chapter is devoted to the development of forward modeling schemes for 2D marine ERT and 3D marine CSEM surveys. The chapter includes a review of the forward modeling schemes of ERT and CSEM surveys. The numerical accuracy of the forward modeling schemes is validated by comparison with an analytical solution.

The third chapter is devoted to the development of inversion algorithms for 2D marine ERT surveys and 3D marine CSEM surveys. This chapter includes a review of inversion algorithms of ERT and CSEM surveys. The performance of the inversion algorithms is investigated using synthetic data sets.

The fourth chapter is devoted to the application of the 2D marine ERT inversion algorithm to data observed in the Iheya North hydrothermal field, Okinawa. I carefully discuss the reliability of the inverted model. The inverted model is interpreted combined with other geophysical information such as seismic and drilling.

The fifth chapter is devoted to the application of the 3D marine CSEM inversion algorithm to data observed in the Ieyama hydrothermal field, Okinawa.

The sixth chapter is devoted to the inferred conceptual model of SMS mineralization from shallow and deep resistivity structures. I discuss the generation mechanism of SMS based on the resistivity models obtained in the fourth and fifth chapters.

In the last chapter, general conclusions of the thesis, and the topics relevant for future research are discussed.

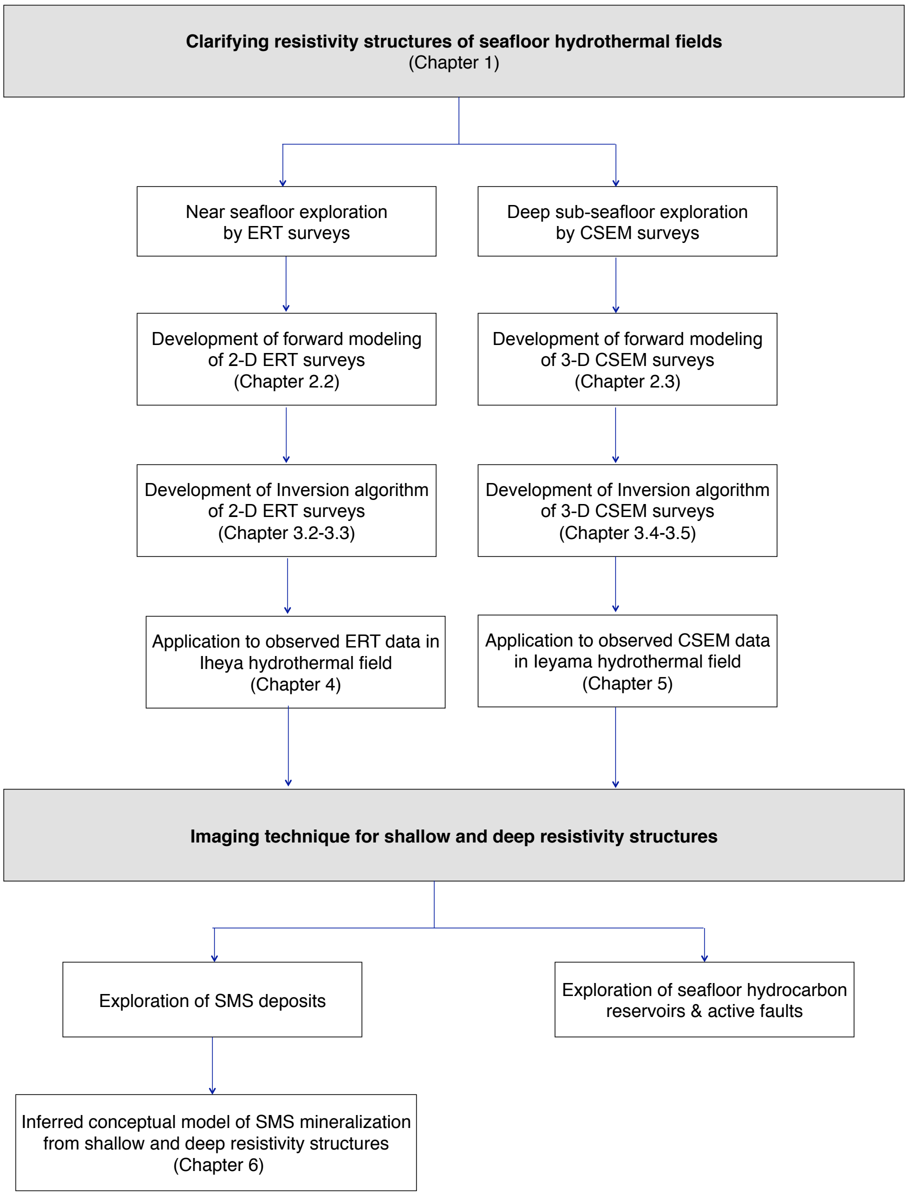

Figure 1.8. Overview of structures of this thesis.

Chapter 2

Development of forward modeling schemes

2.1 Introduction

Forward modeling schemes compute synthetic responses from the model based on known physics. Both ERT and CSEM forward modeling schemes compute their responses from the resistivity models (Fig. 2.1). The resistivity models in 1D, 2D, and 3D are discretized into the mesh. The FDM, FEM, and IE are generally used for solving governing equations in the forward problems of ERT and CSEM surveys. The forward modeling algorithms are the cores of inversion algorithms. Therefore, accurate and computationally efficient forward modeling schemes are required for inversion algorithms.

For the near-seafloor explorations using the 2D marine deep-towed ERT surveys, the detailed bathymetry should be included in the modeling. I apply the unstructured meshes generated by Triangle (Shewchuk 1996) to model discretization. The unstructured meshes are recently used for ERT and EM modeling due to its flexibility to complex bathymetry (Key & Weiss 2006, Rücker *et al.* 2006, Usui *et al.* 2018). I solve the governing equation of ERT surveys in the forward using the FEM with the unconstructed meshes. The performance of the forward modeling algorithm is investigated by comparing forward responses with analytical solution from the two-layer model.

For the 3D CSEM modeling, the number of the model parameters is much larger than the 2D modeling. A large number of model parameters require huge computation resources. Computational efficiency is a key for the 3D CSEM forward modeling. The most time-consuming part is solving the linear equation of the forward modeling. The linear equation is solved by a multicore parallel sparse direct solver PARDISO (Schenk & Gärtner 2004) via Intel MKL library. The parallel sparse direct solver can enable the fast computation of solving the linear equation. The governing equation is solved by the FDM method due to the simplicity of mesh generation. I show the performance of the developed forward modeling algorithm using 1D and 3D examples. The responses from the forward modeling algorithm is compared with responses by DIPOLE1D (Key 2009) for the 1D case and by 3D forward modeling code (Li *et al.* 2018) for the 3D case.

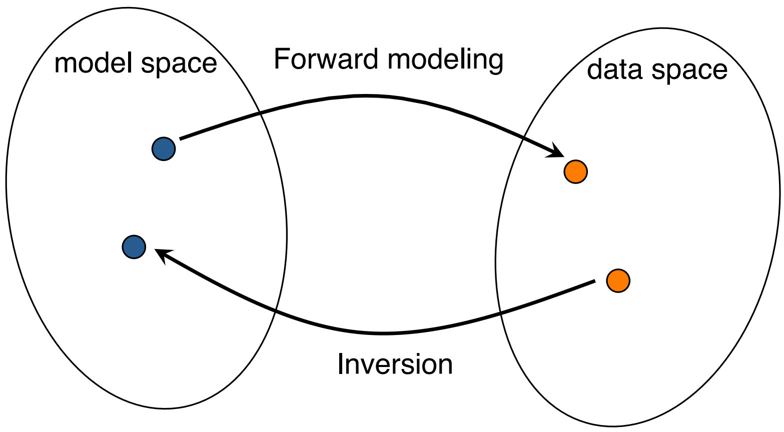

Figure 2.1. Schematic diagram of forward modeling and inversion.

2.2 2D towed marine ERT forward modeling

2.2.1 Fundamental equation

The governing equation of marine ERT surveys can be derived from Ohm's Law and the conservation of current. When electrical current flows into a conductor, Ohm's Law is expressed below

$$\mathbf{J} = -\sigma\nabla\phi \tag{2-1}$$

where **J** is the current density, σ is the conductivity and ϕ is the electric potential. The conservation of current is

$$\nabla\cdot\mathbf{J} = \frac{\partial q}{\partial t}\delta(x)\delta(y)\delta(z) \tag{2-2}$$

where q is the charge density at a point in the Cartesian (x, y, z) space by the Dirac delta function. Substituting eq. (2-1) into (2-2), 3D Poisson's equation are given as

$$-\nabla\cdot[\sigma(x,y,z)\nabla\phi(x,y,z)] = \frac{\partial q}{\partial t}\delta(x_s)\delta(y_s)\delta(z_s) \tag{2-3}$$

where (x_s, y_s, z_s) indicate the coordinates of the point source of charge injected in the Cartesian (x, y, z) space. The potential at any point in the medium can be calculated if the conductivity distribution is known. The conductivity distribution can be modeled in 1D, 2D, and 3D models. In this study, 2D resistivity models are assumed indicating the conductivity distribution in the strike y-direction is not changed. For the 2D resistivity models, the Poisson's equation is given as

$$-\nabla\cdot[\sigma(x,z)\nabla\phi(x,y,z)] = \frac{\partial q}{\partial t}\delta(x_s)\delta(y_s)\delta(z_s) \tag{2-4}$$

For computational ease, solving the equation in Fourier transformed space (x, k_y, z) where k_y is wave number. The transformation is performed in the forward and backward direction by

$$\tilde{\phi}(x,k_y,z) = \int_0^\infty \phi(x,y,z)\cos(k_y y)\mathrm{d}y \tag{2-5}$$

and

$$\phi(x,y,z) = \frac{2}{\pi}\int_0^\infty \tilde{\phi}(x,k_y,z)\cos(k_y y)\mathrm{d}k_y \tag{2-6}$$

, respectively.

The Fourier transformed equation from eq. (2-4) are

$$\nabla\cdot[\sigma(x,z)\nabla\tilde{\phi}(x,k_y,z)] - k_y^2\sigma(x,z)\tilde{\phi}(x,k_y,z) = -\frac{1}{2}\delta(x_s)\delta(z_s) \tag{2-7}$$

where $\tilde{\phi}$ denotes the Fourier potential. I use a so-called secondary field approach to remove the singularity at source positions. This singularity removal technique enables using coarse meshes around electrodes (Coggon 1971).

$$\tilde{\phi}(x,k_y,z) = \tilde{\phi}^p(x,k_y,z) + \tilde{\phi}^s(x,k_y,z) \tag{2-8}$$

The total field is divided into a primary field and secondary field. In this study, the primary potential is calculated from a homogenous half-space. The primary potential is obtainable as

$$\tilde{\phi}^p(x,k_y,z) = \frac{I}{2\pi\sigma^p(x,z)}K^0(k_y r) \tag{2-9}$$

where $r^2 = x^2 + z^2$, K^0 is the zero-order Bessel function, and σ^p represents the primary conductivity. The primary conductivity is homogeneous and set to be the sea conductivity. The governing equation for the primary field is written as follows.

$$\nabla\cdot[\sigma^p(x,z)\nabla\tilde{\phi}^p(x,k_y,z)] - k_y^2\sigma^p(x,z)\tilde{\phi}^p(x,k_y,z) = -\frac{1}{2}\delta(x_s)\delta(z_s) \tag{2-10}$$

Using eqs. (2-7) and (2-10), I can remove the Dirac delta function as shown below.

$$\begin{aligned}\nabla\cdot[\sigma(x,z)\nabla\tilde{\phi}^s(x,k_y,z)] &- k_y^2\sigma(x,z)\tilde{\phi}^s(x,k_y,z)\\ &= -\nabla\cdot[\sigma^s(x,z)\nabla\tilde{\phi}^p(x,k_y,z)] + k_y^2\sigma^s(x,z)\tilde{\phi}^p(x,k_y,z)\end{aligned} \tag{2-11}$$

To solve the secondary potential in eq. (2-11), mixed boundary conditions proposed by Dey & Morrison (1979) are applied. The mixed boundary conditions were based on the asymptotic behavior of the potential field in a homogeneous medium.

2.2.2 Discretization

The governing equation of ERT surveys has been used discretized by the FDM (Dey & Morrison 1979), and the FEM (Coggon 1971). The FDM and FEM handle the boundary value problem using very different principles. The FDM directly transfers partial differential equations into difference equations and the FEM method is based on the variational principle or the method of weighted residuals (Li & Spitzer 2002). The FEM is more flexible for modeling complex geometry than the FDM. The 2D ERT forward problem is solved using the FEM with unconstructed meshes to model complex topography in hydrothermal fields. The unconstructed meshes can model complex geometry more efficiently than structured meshes. I generate unstructured meshes using Triangle (Shewchuk 1996). The FE equations are assembled into a system of equations

$$\mathbf{K}\widetilde{\boldsymbol{\phi}}^{s} = \mathbf{b} \tag{2-12}$$

where **K** is sparse and symmetric and **b** is a vector of dimension containing the primary field information and the boundary condition of secondary potential.

2.2.3 Selection of wave number

The vector of transformed electric potential $\widetilde{\boldsymbol{\phi}}$ is computed by solving eq. (2-12). The inverse Fourier transform is applied to transform $\widetilde{\boldsymbol{\phi}}$ to electric potential $\boldsymbol{\phi}$ in the Cartesian (*x, y, z*) space. For efficient computation, the possible smallest number is desirable while the accurate solution is still calculated. In this thesis, the optimization approach proposed by Xu *et al.* (2000) is used for calculating the inverse Fourier transform. The electric potential $\boldsymbol{\phi}$ is expressed as a linear combination of the transformed electric potential $\widetilde{\boldsymbol{\phi}}$

$$\phi(\mathrm{x,z}) = \sum_{p=1}^{n} \widetilde{\phi}(x, k_{y_p}, z)\, g_p \tag{2-13}$$

where n is the number of wavenumber k_y, and g_p is the weighting parameters. For the homogenous half-space earth, the potential is a function of the earth resistivity and the radial distance as follows

$$\phi(\mathrm{x,y,z}) = \frac{I}{2\pi\sigma}\frac{1}{\sqrt{x^2+y^2+z^2}} \tag{2-14}$$

Taking the Fourier transform in y direction of the both sides of eq. (2-14), I yield

$$\widetilde{\phi}(\mathrm{x}, k_y, z) = \int_0^{\infty} \frac{I}{2\pi\sigma}\frac{\cos(k_y y)}{\sqrt{x^2+y^2+z^2}}\mathrm{dy} = \frac{I}{2\pi\sigma}K^0(k_y r) \tag{2-15}$$

where $r = \sqrt{x^2+z^2}$. Substituting eqs. (2-14) and (2-15) into (2-13) and setting y=0, I obtain

$$\frac{1}{r} \approx \sum_{p=1}^{n} K^0\left(k_{y_p} r\right) g_p \tag{2-16}$$

Setting a set of electrode spacing r_i ($1 \le i \le m$), the discrete wavenumber k_y and corresponding weighting parameters g_p can be determined by solving a non-linear optimization problem as follows:

$$\min_{k_j,} \Psi \approx \sum_{i=1}^{m}\left[\frac{1}{r_i} - \sum_{p=1}^{n} g_p K^0\left(k_{y_p} r\right)\right] \tag{2-17}$$
$$\text{s.t. } k_{y_p} > 0, g_p > 0$$

The non-negative constraints are imposed on the optimization problem. Xu *et al.* (2000) used a two-step gradient-based approach for obtaining an optimal set of the wavenumber and corresponding weighting parameters. The first step is to determine the values of g_p from their given set of k_y by solving the linear least-squares method in the first step. The second step is to determine optimal k_y for obtained weighting parameters g_p by using non-linear least-squares method. By repeating the iterations, an optimal set of k_y and g_p which make the objective function Ψ are determined (Pan & Tang 2014). Following 2D forward modeling presented by Vachiratienchai & Siripunvaraporn (2013), a set of eight number of wavenumbers and weighting is selected in this study.

2.3 Validation of 2D towed marine ERT forward modeling scheme

I validate the forward modeling performance through comparison between numerical results of the forward calculation and analytical results. High numerical accuracy is necessary because a tiny change of the apparent resistivity in the marine environment can reflect a significant change of the seafloor model. The test model for validation is a two-layer model consisting of the sea and the sub-seafloor layer. The analytical apparent resistivity is written as

$$\rho_{\mathrm{a}} = \frac{\rho_{\mathrm{w}}^2(R' - R) + \rho_{\mathrm{w}}\rho_{\mathrm{s}}(R' + R)}{\rho_{\mathrm{s}}R' + \rho_{\mathrm{w}}R'} \quad \textbf{(2-18)}$$

where

$$\frac{1}{R} = \frac{1}{r_{c_1p_1}} - \frac{1}{r_{c_12}} - \frac{1}{r_{c_2p_1}} + \frac{1}{r_{c_2p_2}} \quad \textbf{(2-19)}$$

and

$$\frac{1}{R'} = \frac{1}{r_{c_1'p_1}} - \frac{1}{r_{c_1'p_2}} - \frac{1}{r_{c_2'p_1}} + \frac{1}{r_{c_2'p_2}} \quad \textbf{(2-20)}$$

Therein, ρ_w and ρ_s respectively represent seawater and sub-seafloor resistivity (Fig. 2.2). Here, the relative error is defined as presented below.

$$\mathrm{Error} = 100 \times \frac{\left|\rho_a^{\mathrm{cal}} - \rho_a^{\mathrm{true}}\right|}{\rho_a^{\mathrm{true}}} \quad \textbf{(2-21)}$$

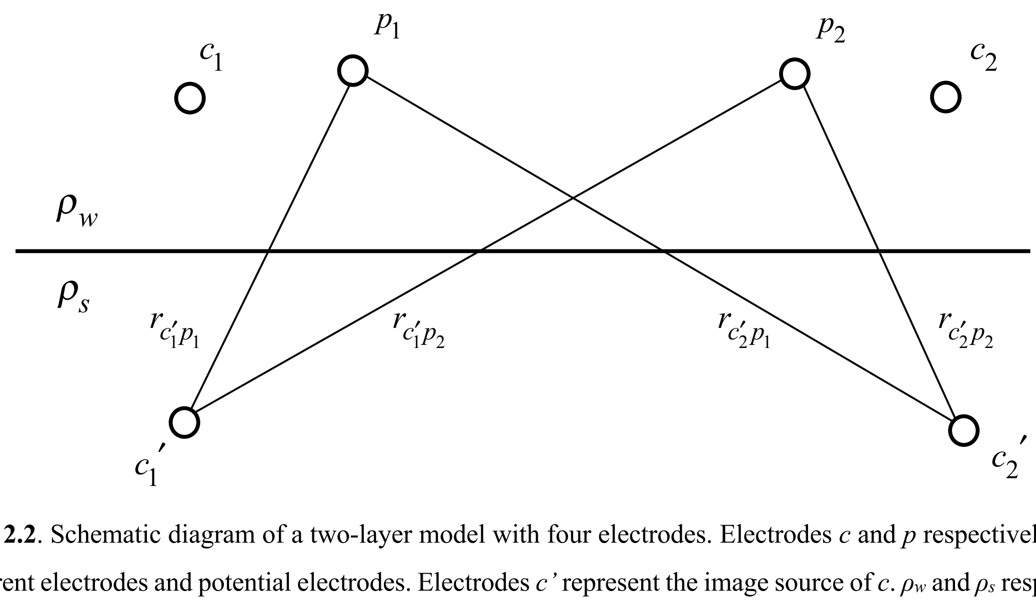

Figure 2.2. Schematic diagram of a two-layer model with four electrodes. Electrodes *c* and *p* respectively denote the current electrodes and potential electrodes. Electrodes *c'* represent the image source of *c*. ρ_w and ρ_s respectively represent seawater resistivity and sub-seafloor resistivity. *r* represents the distance from a current electrode to a potential electrode.

For the numerical test, ρ_w and ρ_s are assumed respectively to be 0.3 and 1.0 Ohm-m. The ERT system shown in Fig. 1.6 is used for the data acquisition. The apparent resistivity is calculated each 5 m in horizontal distance (during towing from 0 to 1000 m) at towed height of 10 m above the seafloor. The total number of the apparent resistivity data is 1344. The model for this forward calculation includes 4197 vertices and 8378 triangles (Fig. 2.3). Fig. 2.4 presents a pseudo-section of response and error where the n Level is related to the distance between a transmitter and receiver: Tx-Rx are $15 \times n$ m. Average errors, derived from the apparent resistivity at various horizontal positions of towed cable, are less than 0.7%. Therefore, I conclude that the forward modeling code is sufficiently accurate compared to observation errors found in real fields.

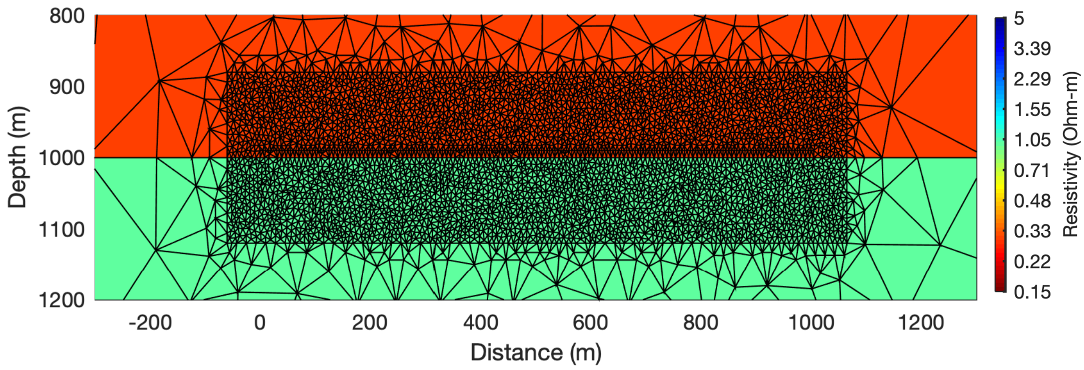

Figure 2.3. Model discretization using unstructured grids. The red and green area shows the sea and sub-seafloor, respectively. The depth is from the sea surface. The seafloor is at a depth of 1000 m.

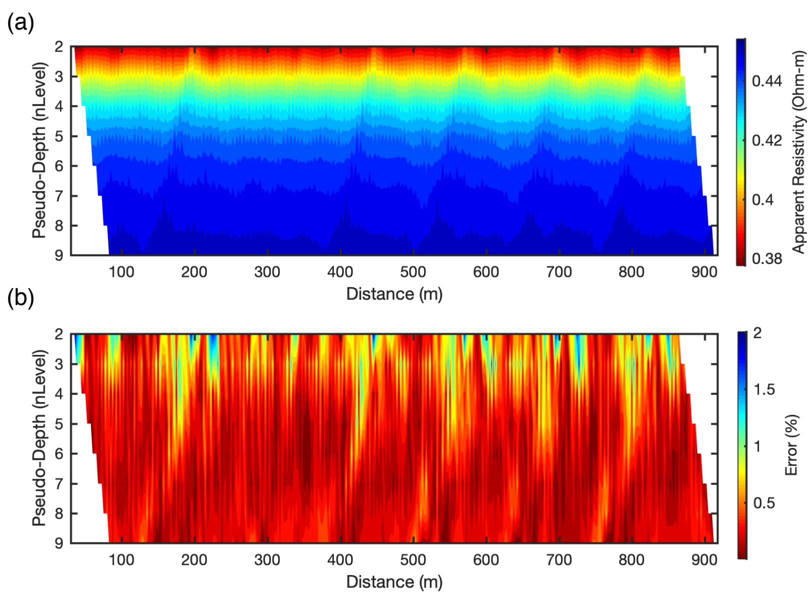

Figure 2.4. (a) Apparent resistivity pseudo-section. Pseudo-depth shows the n level of Tx-Rx distance ($15 \times n$). (b) Relative error of the response.

2.4 3D marine CSEM forward modeling

2.4.1 Fundamental equation

For the 3D CSEM forward modeling, neglecting the displacement currents, Maxwell's equations in the frequency domain are

$$\nabla \times \mathbf{E} - i\omega\mu\mathbf{H} = 0 \tag{2-22}$$

and

$$\nabla \times \mathbf{H} - \sigma\mathbf{E} = \mathbf{J} \tag{2-23}$$

where **E** and **H** respectively stand for the electric and magnetic fields, ω denotes the angular frequency of the field assuming time-dependence of the form $e^{-i\omega t}$, μ expresses the magnetic permeability, σ signifies the conductivity, and **J** is the vector of the current density of a source. To solve Maxwell's equation, the total field and scattered field approaches are useful. The total field approach requires production of fine grids around transmitters (Um *et al.* 2013, Key 2016, Cai *et al.* 2017). In the scattered field approach, the source term can be converted into primary field information, allowing rough mesh around transmitters (Newman & Alumbaugh 1997, Weiss & Constable 2006, Sasaki & Meju 2009, Streich 2009, Schwarzbach *et al.* 2011, da Silva *et al.* 2012, Grayver *et al.* 2013, Dehiya *et al.* 2017). The primary field is an analytical solution from layered earth. I use a scattered field technique for computational efficiency. The total electromagnetic fields are split into a primary and secondary field as

$$\mathbf{E} = \mathbf{E}^p + \mathbf{E}^s \tag{2-24}$$

$$\mathbf{H} = \mathbf{H}^p + \mathbf{H}^s \tag{2-25}$$

where $\mathbf{E}^p$ represents the primary electric field, $\mathbf{E}^s$ denotes the secondary electric field, $\mathbf{H}^p$ signifies the primary magnetic field, and $\mathbf{H}^s$ represents the secondary magnetic field. Calculation of the primary field is described in the next section. Maxwell's equations for the primary field are

$$\nabla \times \mathbf{E}^p - i\omega\mu\mathbf{H}^p = 0 \tag{2-26}$$

and

$$\nabla \times \mathbf{H}^p - \sigma^p\mathbf{E}^p = \mathbf{J} \tag{2-27}$$

where σ^p represents the background layered conductivity.

Substituting eqs. (2-26) and (2-27) to eqs. (2-22) and (2-23), I obtain

$$\nabla \times \mathbf{E}^s - i\omega\mu\mathbf{H}^s = 0 \tag{2-28}$$

and

$$\nabla \times \mathbf{H}^s - \sigma\mathbf{E}^s = (\sigma - \sigma^p)\mathbf{E}^p \tag{2-29}$$

By taking the curl of eq. (2-28), then substitute into eq. (2-29), I obtain the vector Helmholtz equation for the secondary electric field as shown below.

$$-\nabla \times \nabla \times \mathbf{E}^s + i\omega\mu\sigma\mathbf{E}^s + i\omega\mu(\sigma - \sigma^p)\mathbf{E}^p = 0 \tag{2-30}$$

2.4.2 Primary field computation

The primary field is calculable analytically in the layered earth (Chave & Cox 1982, Løseth & Ursin 2007, Key 2009, Li & Li 2016). The formulation of Schelkunoff potential is used in this study to compute the electromagnetic field (Ward & Hohmann 1988). Using Schelkunoff potential **B**, the electromagnetic fields of electric sources can be expressed as shown below.

$$\mathbf{E} = i\omega\mu\mathbf{B} + \frac{1}{\sigma}\nabla(\nabla \cdot \mathbf{B}) \tag{2-31}$$

$$\mathbf{H} = \nabla \times \mathbf{B} \tag{2-32}$$

The potential is obtainable from the solution of the Hankel transform equation of

$$\mathbf{B} = \frac{1}{2\pi}\int_0^\infty \widehat{\mathbf{B}}(\lambda, z) J_0(\lambda r)\lambda dr \tag{2-33}$$

where J_0 represents a zeroth-order Bessel function of the first kind and r denotes the horizontal range. Recursive formation for computation of the transform kernel $\widehat{\mathrm{B}}$ for horizontal and vertical electric dipoles in the layered earth is described by Li & Li (2016). The Hankel transforms are evaluated using the digital filter method (Guptasarma & Singh 1997, Kong 2007). I apply a 201-point filter produced using a direct matrix inversion method (Kong 2007) to the Hankel transforms of primary field computation.

2.4.3 Discretization

Maxwell's equation can be discretized using FDM (Mackie & Madden 1993, Davydycheva *et al.* 2003, Weiss & Constable 2006, Sasaki & Meju 2009, Mittet 2010, Jaysaval *et al.* 2015, Li *et al.* 2018), FEM (Nam *et al.* 2007, Schwarzbach & Haber 2013, Wang *et al.* 2018, Usui *et al.* 2018), and IE (Avdeev *et al.* 2002, Gribenko & Zhdanov 2007). For this study, FDM is used because of its speed of computation and simplicity of mesh generation. Actually, FEM is suitable for modeling complex bathymetry. Some techniques for modeling bathymetry with FDM have been developed because the simplicity of FDM is still useful (Baba *et al.* 2013). Writing eq. (2-30) explicitly in the three components produces the following.

$$\frac{\partial}{\partial y}\frac{\partial \mathbf{E}_x^s}{\partial y} + \frac{\partial}{\partial z}\frac{\partial \mathbf{E}_x^s}{\partial z} - \frac{\partial}{\partial y}\frac{\partial \mathbf{E}_y^s}{\partial x} - \frac{\partial}{\partial z}\frac{\partial \mathbf{E}_z^s}{\partial x} + i\omega\mu\sigma\mathbf{E}_x^s + i\omega\mu(\sigma - \sigma^p)\mathbf{E}_x^p = 0 \tag{2-34}$$

$$\frac{\partial}{\partial x}\frac{\partial \mathbf{E}_y^s}{\partial x} + \frac{\partial}{\partial z}\frac{\partial \mathbf{E}_y^s}{\partial z} - \frac{\partial}{\partial x}\frac{\partial \mathbf{E}_x^s}{\partial y} - \frac{\partial}{\partial z}\frac{\partial \mathbf{E}_z^s}{\partial y} + i\omega\mu\sigma\mathbf{E}_y^s + i\omega\mu(\sigma - \sigma^p)\mathbf{E}_y^p = 0 \tag{2-35}$$

$$\frac{\partial}{\partial x}\frac{\partial \mathbf{E}_z^s}{\partial x} + \frac{\partial}{\partial y}\frac{\partial \mathbf{E}_z^s}{\partial y} - \frac{\partial}{\partial x}\frac{\partial \mathbf{E}_x^s}{\partial z} - \frac{\partial}{\partial y}\frac{\partial \mathbf{E}_y^s}{\partial z} + i\omega\mu\sigma\mathbf{E}_z^s + i\omega\mu(\sigma - \sigma^p)\mathbf{E}_z^p = 0 \tag{2-36}$$

The equations above are solved using FDM with Yee's staggered grid (Yee 1966). The electric sample point is at the center of each edge and the magnetic sample point is at the center of each face (Fig. 2.5).

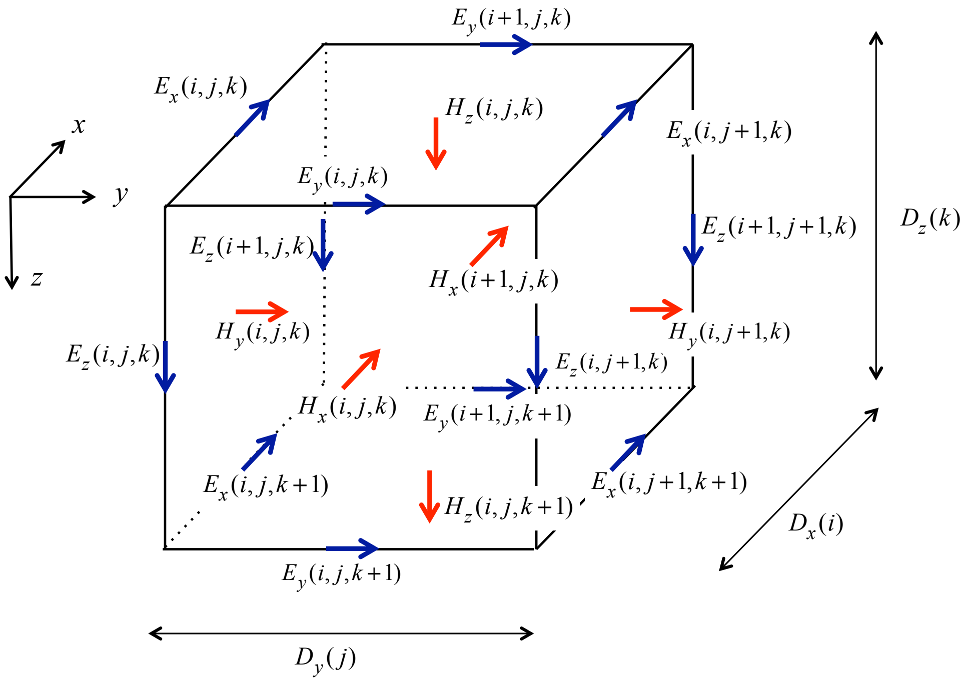

Figure 2.5. Coordinate system and Yee's grid system used. Electric field components E_x, E_y, and E_z are on the cell edges. Magnetic field components H_x, H_y, and H_z are on the cell faces.

The entire computational domain is divided into $N_{\text{cell}} = N_x \times N_y \times N_z$ cells, where N_x, N_y, and N_z respectively denote the numbers of cells in the x-, y-, and z- directions (Fig. 2.6). By applying the Yee's staggered grid to of eqs. (2-34)-(2-36),

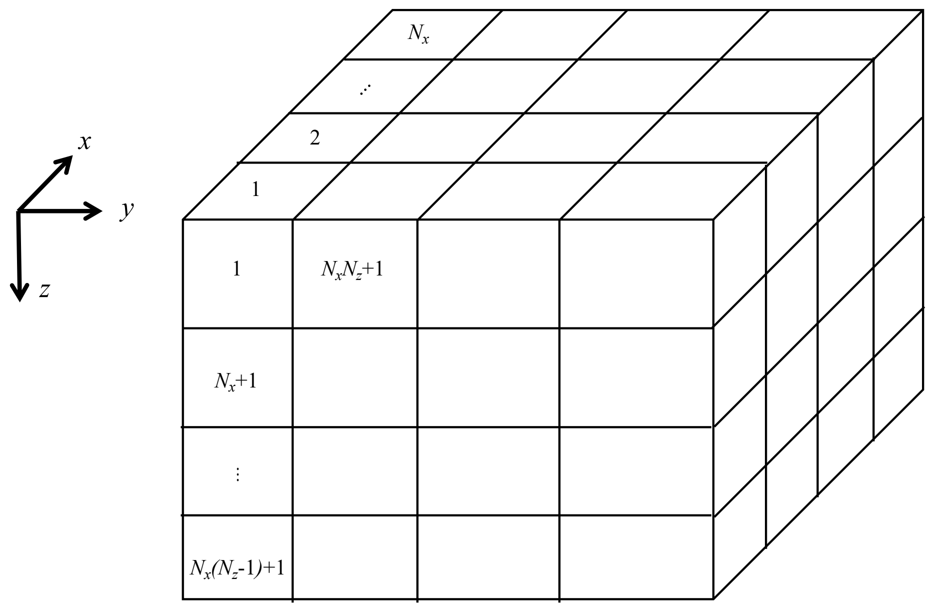

Figure 2.6. An ordering of the meshes in the 3D model.

$$\left[i\omega\mu\sigma(i,j,k)-\frac{2}{D_y(j-1)D_y(j)}-\frac{2}{D_z(k-1)D_z(k)}\right]E_x^s(i,j,k)+\frac{1}{D_y(j)\Delta y(j)}E_x^s(i,j+1,k)$$
$$+\frac{1}{D_y(j-1)\Delta y(j)}E_x^s(i,j-1,k)+\frac{1}{D_z(k)\Delta z(k)}E_x^s(i,j,k+1)+\frac{1}{D_z(k-1)\Delta z(k)}E_x^s(i,j,k-1)$$
$$-\frac{1}{D_x(i)\Delta y(j)}\left[E_y^s(i+1,j,k)+E_y^s(i,j-1,k)-E_y^s(i,j,k)-E_y^s(i+1,j-1,k)\right]$$
$$-\frac{1}{D_x(i)\Delta z(k)}\left[E_z^s(i+1,j,k)+E_z^s(i,j,k-1)-E_z^s(i,j,k)-E_z^s(i+1,j,k-1)\right]$$
$$+i\omega\mu[\sigma(i,j,k)-\sigma^p(i,j,k)]E_x^p(i,j,k)=0$$

(2-37)

$$\left[i\omega\mu\sigma(i,j,k)-\frac{2}{D_x(i-1)D_x(i)}-\frac{2}{D_z(k-1)D_z(k)}\right]E_y^s(i,j,k)+\frac{1}{D_x(i)\Delta x(i)}E_y^s(i+1,j,k)+\frac{1}{D_x(i-1)\Delta x(i)}E_y^s(i-1,j,k)$$
$$+\frac{1}{D_z(k)\Delta z(k)}E_y^s(i,j,k+1)+\frac{1}{D_z(k-1)\Delta z(k)}E_y^s(i,j,k-1)$$
$$-\frac{1}{D_y(j)\Delta x(i)}\left[E_x^s(i,j+1,k)+E_x^s(i-1,j,k)-E_x^s(i,j,k)-E_x^s(i-1,j+1,k)\right]$$
$$-\frac{1}{D_y(j)\Delta z(k)}\left[E_z^s(i,j+1,k)+E_z^s(i,j,k-1)-E_z^s(i,j,k)-E_z^s(i,j+1,k-1)\right]$$
$$+i\omega\mu[\sigma(i,j,k)-\sigma^p(i,j,k)]E_y^p(i,j,k)=0$$

(2-38)

$$\left[i\omega\mu\sigma(i,j,k)-\frac{2}{D_x(i-1)D_x(i)}-\frac{2}{D_y(j-1)D_y(j)}\right]E_z^s(i,j,k)+\frac{1}{D_x(i)\Delta x(i)}E_z^s(i+1,j,k)$$
$$+\frac{1}{D_x(i-1)\Delta x(i)}E_z^s(i-1,j,k)+\frac{1}{D_y(j)\Delta y(j)}E_z^s(i,j+1,k)+\frac{1}{D_y(j-1)\Delta y(j)}E_z^s(i,j-1,k)$$
$$-\frac{1}{D_z(k)\Delta x(i)}\left[E_x^s(i,j,k+1)+E_x^s(i-1,j,k)-E_x^s(i,j,k)-E_x^s(i-1,j,k+1)\right]$$
$$-\frac{1}{D_z(k)\Delta y(j)}\left[E_y^s(i,j,k+1)+E_y^s(i,j-1,k)-E_y^s(i,j,k)-E_y^s(i,j-1,k+1)\right]$$
$$+i\omega\mu[\sigma(i,j,k)-\sigma^p(i,j,k)]E_z^p(i,j,k)=0$$

(2-39)

where

$$\Delta x(i)=\frac{D_x(i-1)+D_x(i)}{2},\Delta y(j)=\frac{D_y(j-1)+D_y(j)}{2},\Delta z(k)=\frac{D_z(k-1)+D_z(k)}{2} \quad \textbf{(2-40)}$$

The discretization is conducted using neighboring 13 electric fields (Fig. 2.7). The linear system resulting from these equations is not symmetric when the spacing is non-uniform. To make the matrix symmetric, the scaling with volume elements can be used (Smith 1996). Multiplying eqs. (2-37), (2-38), and (2-39) by $D_x(i)\Delta y(j)\Delta z(k)$, $D_y(j)\Delta x(i)\Delta z(k)$ and $D_z(k)\Delta x(i)\Delta y(j)$, respectively.

$$
\begin{aligned}
&\left[i\omega\mu\sigma(i,j,k)D_x(i)\Delta y(j)\Delta z(k) - \frac{2D_x(i)\Delta y(j)\Delta z(k)}{D_y(j-1)D_y(j)} - \frac{2D_x(i)\Delta y(j)\Delta z(k)}{D_z(k-1)D_z(k)}\right]E_x^s(i,j,k) + \frac{D_x(i)\Delta z(k)}{D_y(j)}E_x^s(i,j+1,k) \\
&\quad + \frac{D_x(i)\Delta z(k)}{D_y(j-1)}E_x^s(i,j-1,k) + \frac{D_x(i)\Delta y(j)}{D_z(k)}E_x^s(i,j,k+1) + \frac{D_x(i)\Delta y(j)}{D_z(k-1)}E_x^s(i,j,k-1) \\
&\quad - \Delta z(k)\left[E_y^s(i+1,j,k) + E_y^s(i,j-1,k) - E_y^s(i,j,k) - E_y^s(i+1,j-1,k)\right] \\
&\quad - \Delta y(j)[E_z^s(i+1,j,k) + E_z^s(i,j,k-1) - E_z^s(i,j,k) - E_z^s(i+1,j,k-1)] \\
&\quad + i\omega\mu[\sigma(i,j,k) - \sigma^p(i,j,k)]D_x(i)\Delta y(j)\Delta z(k)E_x^p(i,j,k) = 0
\end{aligned}
\tag{2-41}
$$

$$
\begin{aligned}
&\left[i\omega\mu\sigma(i,j,k)D_y(j)\Delta x(i)\Delta z(k) - \frac{2D_y(j)\Delta x(i)\Delta z(k)}{D_x(i-1)D_x(i)} - \frac{2D_y(j)\Delta x(i)\Delta z(k)}{D_z(k-1)D_z(k)}\right]E_y^s(i,j,k) + \frac{D_y(j)\Delta z(k)}{D_x(i)}E_y^s(i+1,j,k) \\
&\quad + \frac{D_y(j)\Delta z(k)}{D_x(i-1)}E_y^s(i-1,j,k) + \frac{D_y(j)\Delta x(i)}{D_z(k)}E_y^s(i,j,k+1) + \frac{D_y(j)\Delta x(i)}{D_z(k-1)}E_y^s(i,j,k-1) \\
&\quad - \Delta z(k)[E_x^s(i,j+1,k) + E_x^s(i-1,j,k) - E_x^s(i,j,k) - E_x^s(i-1,j+1,k)] \\
&\quad - \Delta x(i)[E_z^s(i,j+1,k) + E_z^s(i,j,k-1) - E_z^s(i,j,k) - E_z^s(i,j+1,k-1)] \\
&\quad + i\omega\mu[\sigma(i,j,k) - \sigma^p(i,j,k)]D_y(j)\Delta x(i)\Delta z(k)E_y^p(i,j,k) = 0
\end{aligned}
\tag{2-42}
$$

$$
\begin{aligned}
&\left[i\omega\mu\sigma(i,j,k)D_z(k)\Delta x(i)\Delta y(j) - \frac{2D_z(k)\Delta x(i)\Delta y(j)}{D_x(i-1)D_x(i)} - \frac{2D_z(k)\Delta x(i)\Delta y(j)}{D_y(j-1)D_y(j)}\right]E_z^s(i,j,k) + \frac{D_z(k)\Delta y(j)}{D_x(i)}E_z^s(i+1,j,k) \\
&\quad + \frac{D_z(k)\Delta y(j)}{D_x(i-1)}E_z^s(i-1,j,k) + \frac{D_z(k)\Delta x(i)}{D_y(j)}E_z^s(i,j+1,k) + \frac{D_z(k)\Delta x(i)}{D_y(j-1)}E_z^s(i,j-1,k) \\
&\quad - \Delta y(j)[E_x^s(i,j,k+1) + E_x^s(i-1,j,k) - E_x^s(i,j,k) - E_x^s(i-1,j,k+1)] \\
&\quad - \Delta x(i)\left[E_y^s(i,j,k+1) + E_y^s(i,j-1,k) - E_y^s(i,j,k) - E_y^s(i,j-1,k+1)\right] \\
&\quad + i\omega\mu[\sigma(i,j,k) - \sigma^p(i,j,k)]D_z(k)\Delta x(i)\Delta y(j)E_z^p(i,j,k) = 0
\end{aligned}
\tag{2-43}
$$

The linear system resulting from these equations become the symmetric. The discrete equations are assembled into a system of equations as

$$\boldsymbol{A}\mathbf{E}^s = \mathbf{b} \tag{2-44}$$

where **A** is complex, sparse and symmetric positive definite of dimension $N_p = N_x \times (N_y + 1) \times (N_z + 1) + (N_x + 1) \times N_y \times (N_z + 1) + (N_x + 1) \times (N_y + 1) \times N_z$, and **b** is a vector of dimension N_p including the primary field information and the boundary condition of secondary electric field. After solving the electric fields, the magnetic fields are calculable from the electric fields as follows:

$$H_x^s(i,j,k) = \frac{1}{i\omega\mu}\left(\frac{\partial E_z^s}{\partial \mathrm{y}} - \frac{\partial E_y^s}{\partial \mathrm{z}}\right) = \frac{1}{i\omega\mu}\left(\frac{E_z^s(i,j+1,k) - E_z^s(i,j,k)}{D_y(j)} - \frac{E_y^s(i,j,k+1) - E_y^s(i,j,k)}{D_z(k)}\right) \tag{2-45}$$

$$H_y^s(i,j,k) = \frac{1}{i\omega\mu}\left(\frac{\partial E_x^s}{\partial \mathrm{z}} - \frac{\partial E_z^s}{\partial \mathrm{x}}\right) = \frac{1}{i\omega\mu}\left(\frac{E_x^s(i,j,k+1) - E_x^s(i,j,k)}{D_z(k)} - \frac{E_z^s(i+1,j,k) - E_z^s(i,j,k)}{D_x(i)}\right) \tag{2-46}$$

$$H_z^s(i,j,k) = \frac{1}{i\omega\mu}\left(\frac{\partial E_y^s}{\partial \mathrm{x}} - \frac{\partial E_x^s}{\partial \mathrm{y}}\right) = \frac{1}{i\omega\mu}\left(\frac{E_y^s(i+1,j,k) - E_y^s(i,j,k)}{D_x(i)} - \frac{E_x^s(i,j+1,k) - E_x^s(i,j,k)}{D_y(j)}\right) \tag{2-47}$$

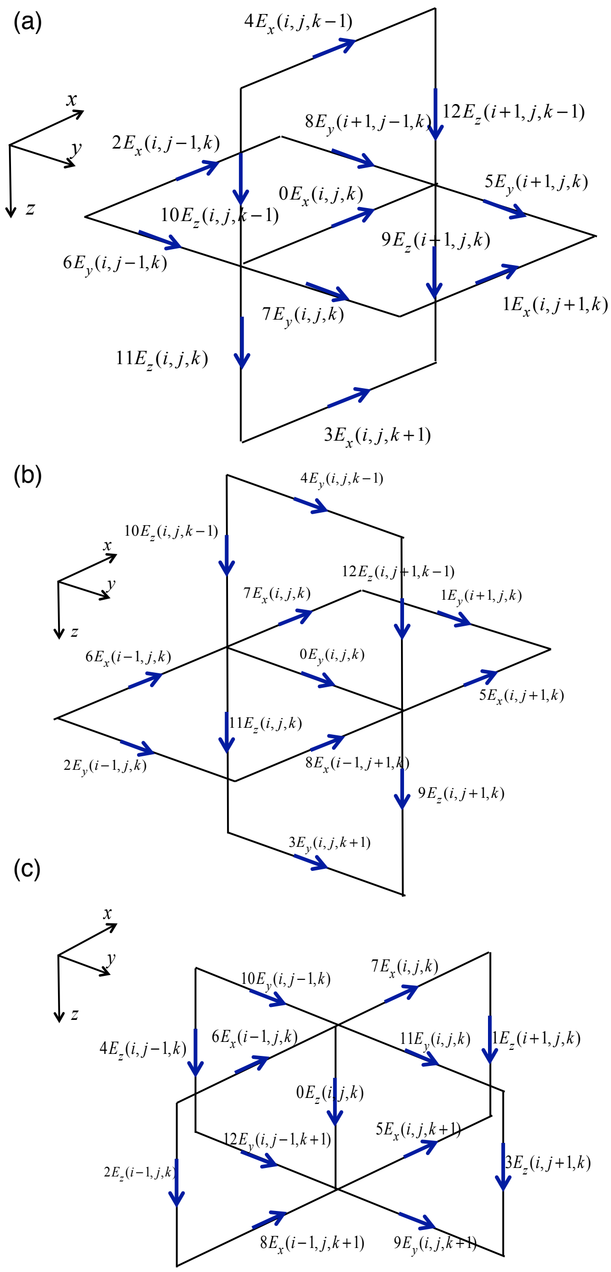

Figure 2.7. Basic staggered-grid discretization. 13 electric fields are used for each component. (a) x-component, (b) y-component and (c) z-component.

2.4.4 Solving linear equation

The system of equations **A** in eq. (2-44) is solvable using iterative method (Mackie & Madden 1993, Smith 1996, Sasaki & Meju 2009, Farquharson & Miensopust 2011, Ansari & Farquharson 2014) and direct solver (Börner *et al.* 2008, Blome *et al.* 2009, Streich 2009, da Silva *et al.* 2012, Grayver *et al.* 2013, Oldenburg *et al.* 2013, Puzyrev *et al.* 2016). Iterative solvers require much less memory. Moreover, they are rapid computing systems for a small RHS. For marine CSEM modeling, the system should be solved for large RHS arising from many transmitter numbers. For large RHS, the direct solver can be faster than the iterative method.

A multicore parallel sparse direct solver PARDISO (Schenk & Gärtner 2004) is used to solve the system in eq. (2-44) accurately. With the direct solver, once the matrix **A** is factored, solving the factored system can be done quickly for numerous sources as RHS (Puzyrev *et al.* 2016). The principle of direct solvers, comprising a single expensive matrix factorization followed by inexpensive solutions for RHS, lends itself to multisource CSEM modeling. Another advantage is that direct solvers can avoid uncertainties in pre-conditioning and convergence for iterative solvers, especially for low-frequency EM difficulties (Streich 2009, Oldenburg *et al.* 2013).

2.4.5 Interpolation

CSEM receivers measure several electromagnetic field components in the same position, although the fields are computed at the Yee's grid in our numerical simulation. Interpolation techniques are useful to compute the field values from grid points to receiver locations. Li *et al.* (2017) proposed an interpolation method adapting total field interpolation technique for MT modeling by Mackie & Madden (1993)to interpolation of the primary and secondary fields for CSEM modeling. Interpolation using the combination between primary and secondary fields can improve the accuracy compared to the total field interpolation because total fields vary rapidly near the source and model discontinuities (Streich 2009).

The interpolation method proposed by Li *et al.* (2017) is used for this study because of its accuracy. Electric field components are on the edges of the cell. Magnetic field components are on the cell faces in our modeling, whereas magnetic field components are on the cell edges. Electric field components are on the cell faces in Li *et al.* (2017). The responses at the receiver locations using the interpolation are computed as

$$\mathbf{F}[\mathbf{m}] = \mathbf{Q}^{\mathrm{p}}\mathbf{E}^{\mathrm{p}} + \mathbf{Q}^{\mathrm{s}}\mathbf{E}^{\mathrm{s}} \tag{2-48}$$

where $\mathbf{Q}^{\mathrm{p}}$ and $\mathbf{Q}^{\mathrm{s}}$ denote interpolation operators for the primary and secondary fields. The interpolation of electric and magnetic fields to receiver points uses neighboring eight points around the receiver points shown in Figs. 2.8 and 2.9, respectively.

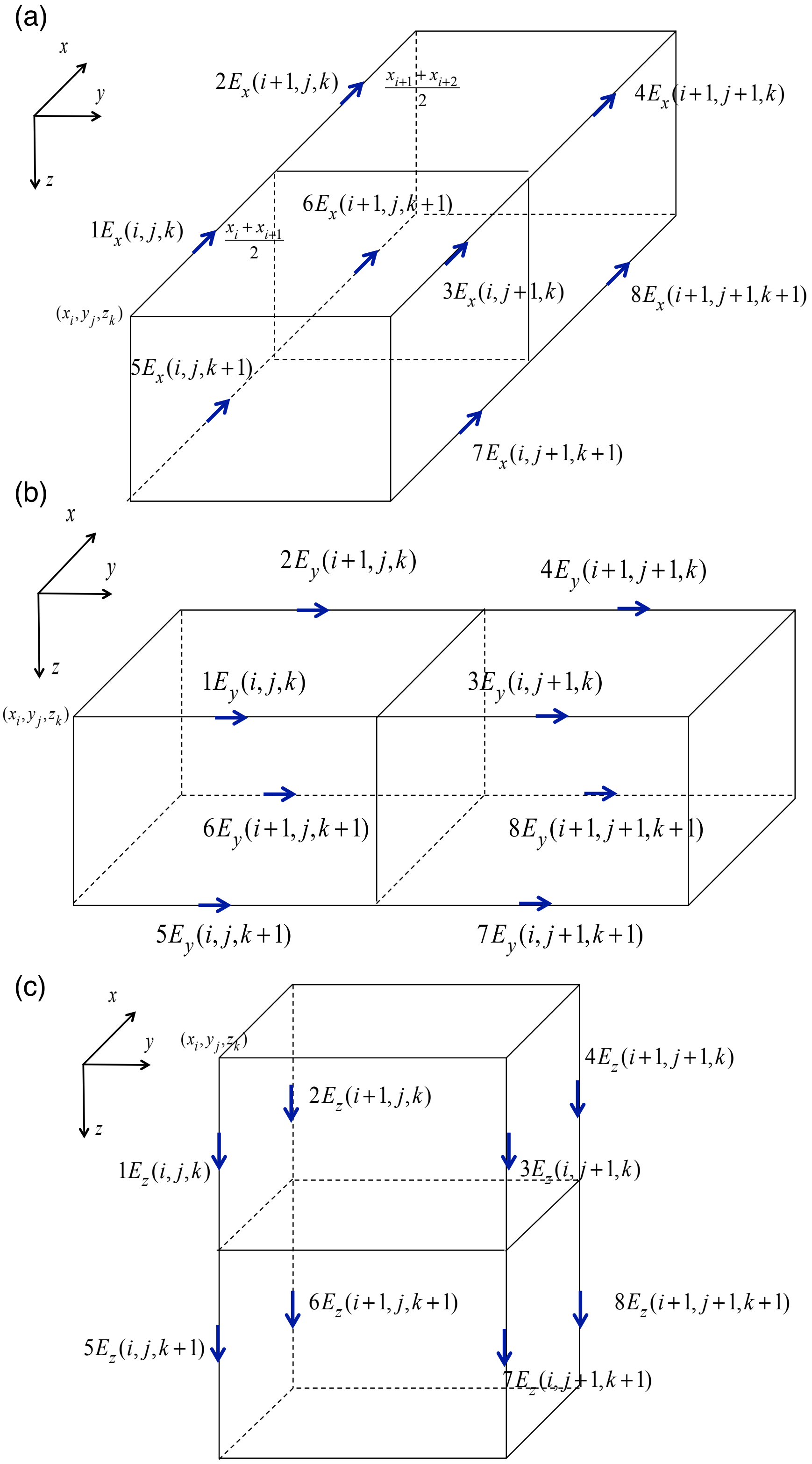

Figure 2.8. Eight points of the electric fields used for interpolation of (a) E_x, (b) E_y, and (c) E_z.

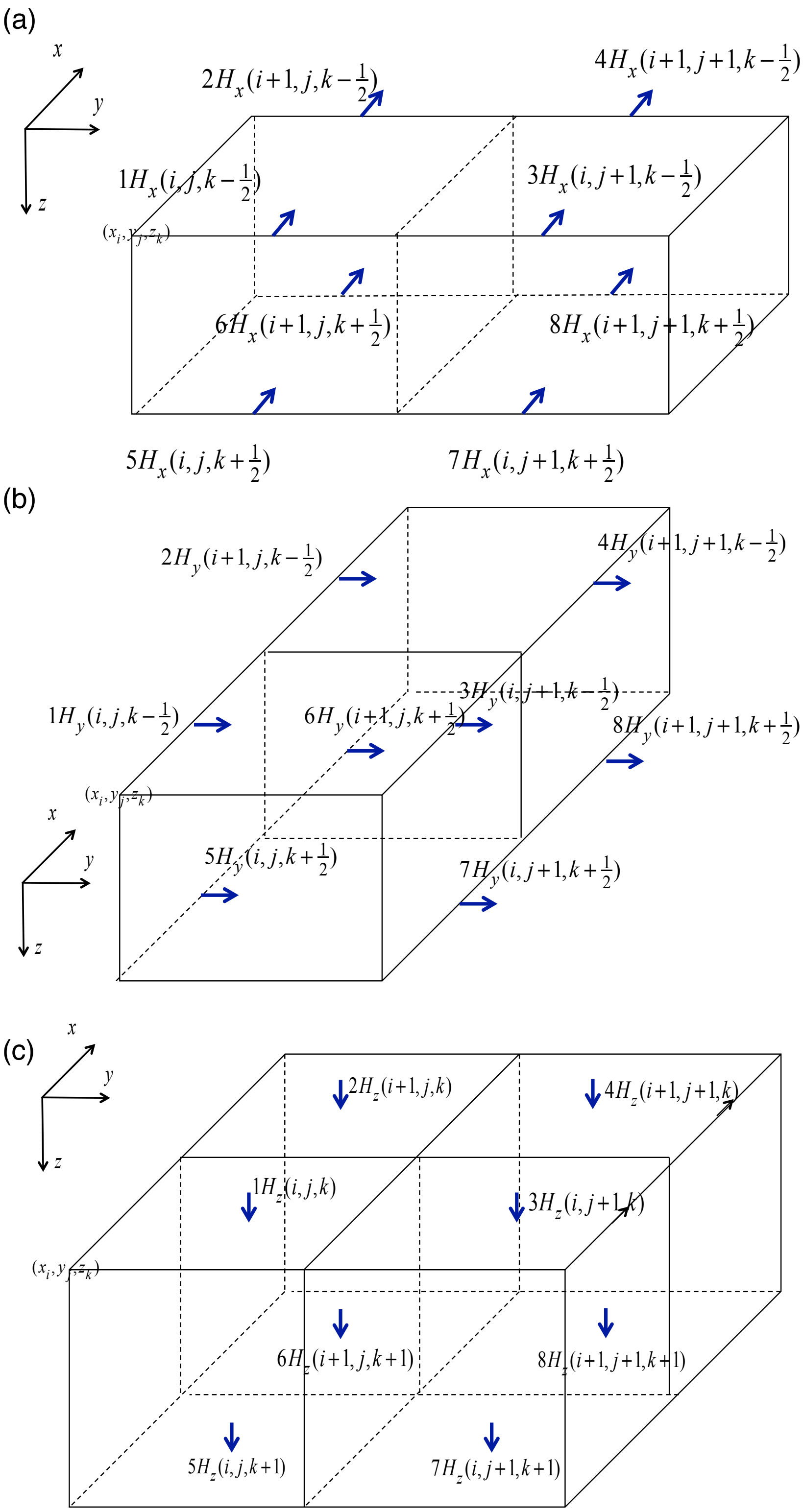

Figure 2.9. Eight points of the magnetic fields used for interpolation of (a) H_x, (b) H_y, and (c) H_z.

2.5 Validation of 3D marine CSEM forward modeling scheme

The forward modeling algorithm is validated using 1D and 3D examples of the oil field model. The forward and inversion are implemented based on Fortran 90. Computations were performed on a machine (@Xeon 2.30 GHz CPU E5-2650 v3; Intel Corp.) with 264 GB of RAM. Discrete matrixes were solved by PARDISO parallelized with 20 threads in OpenMP.

In both examples, the primary fields were calculated in 1D layered earth consisting of air, sea, and seafloor homogeneous half-space. In my forward modeling algorithm, the primary fields must be computed for each grid, entailing additional computation costs. I applied parallel implementation with 20 MPI processes to the computation of the primary field. Once the primary fields are computed, they are stored and reused for each forward calculation.

2.5.1 Models for validation of forward modeling

1D model

A 1D canonical oil reservoir model reported by Weiss & Constable (2006) is used for validation. Our responses by the forward modeling algorithm of 3DDOCSEM can be validated using results from the quasi-analytical 1D algorithm DIPOLE1D (Key 2009). The 1D canonical model consists of an air layer with 10^8 Ohm-m, a sea-water layer with 0.3 Ohm-m resistivity and 1 km thickness, and a reservoir with 100 Ohm-m resistivity embedded into a seafloor layer with 1 Ohm-m resistivity (Fig. 2.10a). The oil reservoir is buried at a depth 1 km below the seafloor with 100 m thickness. A transmitter using a HED oriented along the y-direction is x=5,000, y=0 m at a height 50 m above the seafloor. There, 50 receivers are deployed on the seafloor at 200 m intervals from y=200 to 10,000 m at x=5,000 m.

The forward modeling calculation was performed on a grid of 98 × 98 × 65 cells including several boundary cells to minimize boundary effects. For the horizontal cells, a 200 m grid was used in the interest region $\{(x, y)$: 0 km < x, y < 10 km$\}$. A 100 m grid was used in the region close to the transmitter $\{(x, y)$: 2 km < x, y < 8 km$\}$. I append several boundary cells at each side, growing in size at a stretching factor of 2.0. For the vertical grid, fine grids are used close to the transmitters. The grid size grows gradually with increasing distance from the transmitters

3D model

To demonstrate the general performance, a 3D canonical oil example is considered (Fig. 2.10b). The model consists of an air layer with 10^8 Ohm-m, a seawater layer with 0.3 Ohm-m resistivity and 1 km thickness, and a reservoir with 100 Ohm-m resistivity embedded into a seafloor layer with 1 Ohm-m resistivity. The reservoir is a cuboid with 4 km length, 4 km width, and 100 m height at depth of 1 km below the seafloor. The center of the reservoir corresponds to x=5,000, y=5,000. A transmitter using a HED oriented along y-direction is x=5,000, y=5,000 m at a height 100 m above the seafloor. Also, 50 receivers are deployed on the seafloor at 200 m intervals from y=0 to 10,000 m at x=5,000 m (expect y=5,000 m). The same grid design as that of the 1D example was used for this 3D example.

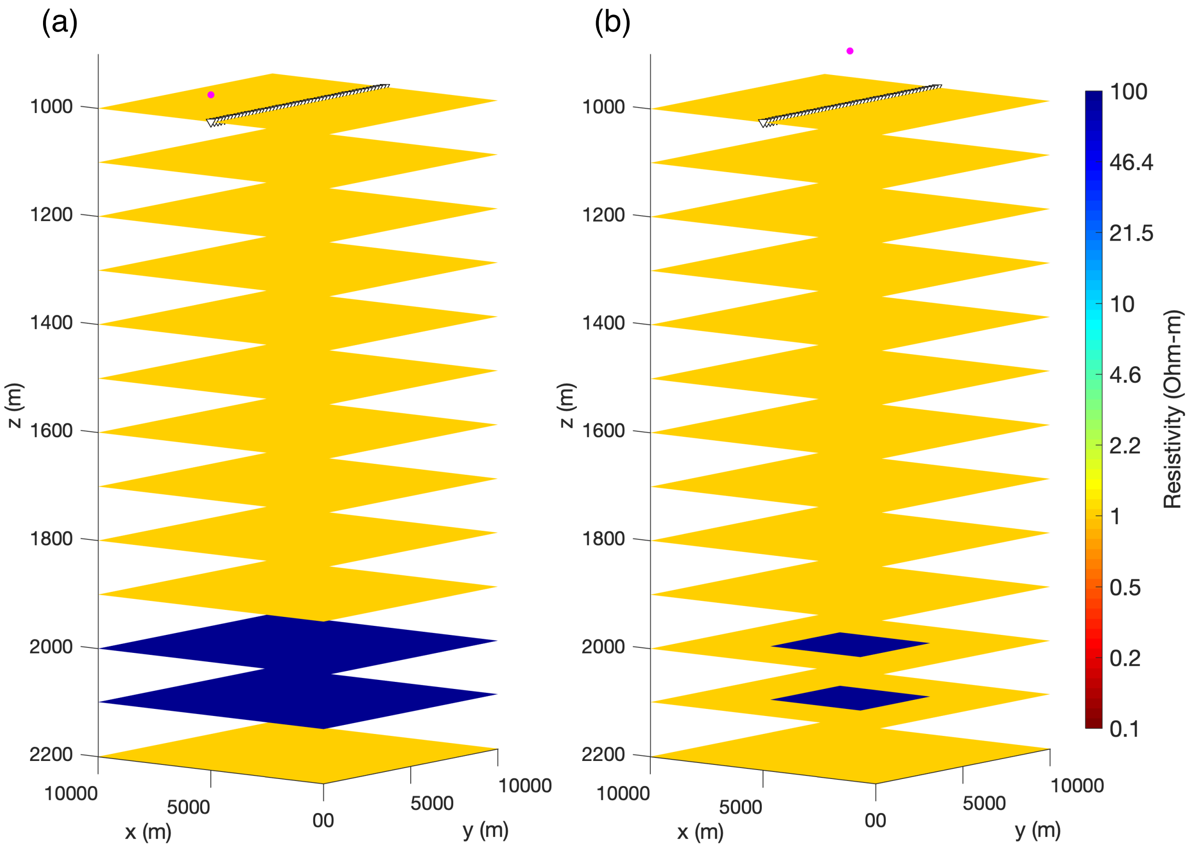

Figure 2.10. Models for validating the developed forward modeling algorithm. Circles ○ and triangles ▽ show the transmitter and receiver positions, respectively. (a) A 1D canonical oil reservoir model consisting of air, sea, oil reservoir embedded into seafloor layer. (b) A 3D canonical oil reservoir model same to Fig. 7 in Li *et al.* (2018). There are air layer, sea layer, and a canonical oil reservoir of the volume $\{(x,y,z)$: 3 km $< x, y <$ 7 km, 2 km $< z <$ 2.1 km$\}$ embedded into a seafloor half-space. The depth is from the sea surface. The seafloor is at a depth of 1000 m.

2.5.2 Results of validation

1D model results

Primary fields are calculated by solving the Hankel transform in 1D layer earth. Therefore, 1D quasi-analytical solutions of the Hankel transform must be sufficiently accurate. The computed 1D quasi-analytical solutions at a frequency of 0.25 Hz were compared to 1D analytical solutions using DIPOLE1D for the model presented in Fig. 2.10a (Fig. 2.11). The maximum error between our quasi-analytical solution and DIPOLE1D for the amplitude for E_y, E_z and H_x is 4.0×10^{-6}%; the absolute error of the phase is less than $2.0 \times 10^{-6\circ}$. This result indicates that our quasi-analytical 1D algorithm is sufficient accurate.

Solutions from the forward modeling algorithm of 3DDOCSEM were compared to 1D analytical solutions by DIPOLE1D (Fig. 2.11). The numerical error at a range of less than 10 km is no more than 1.4% for the amplitude for E_y, E_z and H_x. The absolute error of the phase at a range of less than 10 km is no more than 0.6°. The numerical error of 10–12 km is less than 3% for the amplitude. The responses are erratic at a range of more than 12 km, where the receivers are close to the boundary area. This validation implied that our code can compute accurate solutions when the offset between the source and receiver is less than 12 km. This is usually within the range of our CSEM survey. The same test at a frequency of 1.0 Hz was also conducted. Similar results were obtained. The numerical error at a range of less than 10 km is also no more than 2% for the amplitude for E_y, E_z, and H_x. The responses are erratic in cases where the receivers are close to the boundary area.

By extending the interest region to y=14 km on a grid of 98 × 118 × 65 cells, the forward modeling was able to obtain numerical error less than 3% at a range of 14 km. This result implied that our code can have a more accurate solution at a large offset by extending the interest region, but with greater computation time. The computation time of the forward modeling calculation increased because of the finer grid of 98 × 118 × 65 cells. The linear equations solved using PARDISO took 592 s and 871 s, respectively, with grids of 98 × 98 × 65 and 98 × 118 × 65.

The 3DDOCSEM user must construct a mesh design for forward modeling. The optimal mesh design depends on survey arrays and resistivity models. For automatic mesh generation, adaptive mesh refinement techniques guided by a goal-oriented error estimator have been applied to electromagnetic modeling (Ren *et al.* 2013, Key 2016). The forward problem is solved on iteratively refined meshes until the solution meets a specified tolerance. Mesh refinement is guided by a goal-oriented error estimator based on how the error in each mesh influences the accuracy of the electromagnetic responses at the receiver locations (Key 2016). Future studies will apply the automatic mesh generation technique to our forward modeling algorithm and thereby free the user from the burden of having to design an accurate forward modeling grid.

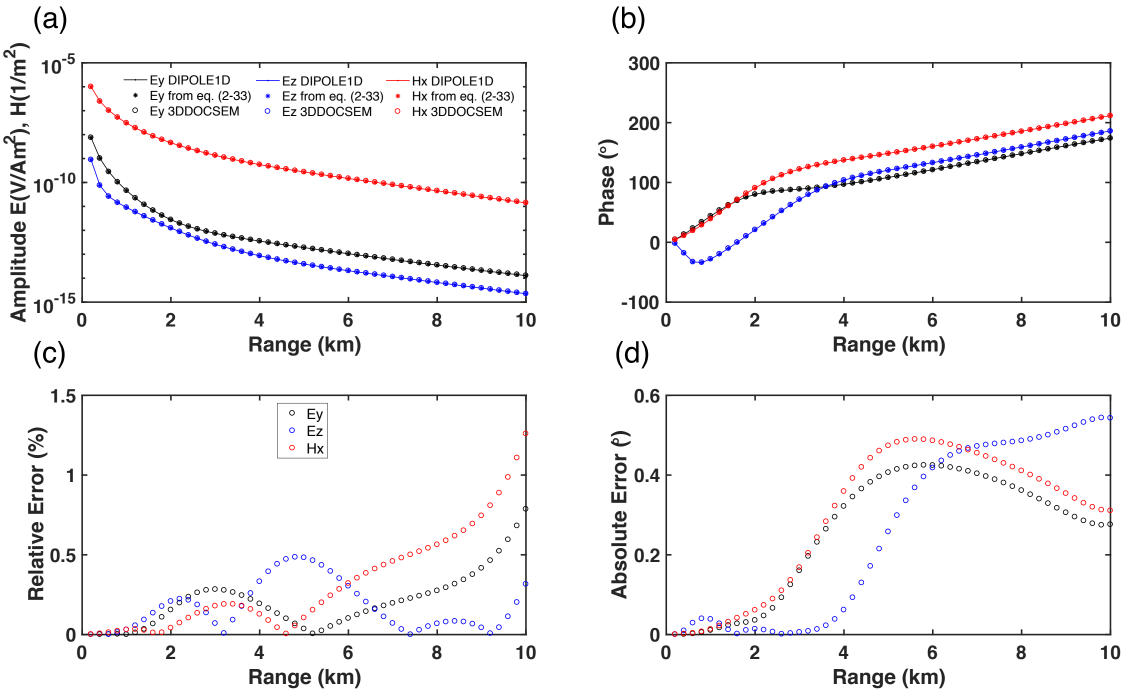

Figure 2.11. Numerical solutions at a frequency of 0.25 Hz. The range shows the transmitter-receiver offset. (a) Amplitude of the electric field **E** (V/Am^2) and magnetic field **H** (1/m^2). (b) Phase of the electric field **E** and magnetic field **H** (°). Solid lines show the response from DIPOLE1D (Key 2009). * and ○ shows responses from my 1D quasi-analytical solutions of the Hankel transform in Eq. (2-33) and 3DDOCSEM, respectively. The colors black, blue and red are for E_y, E_z and H_x. (c) Relative error of amplitude for **E** and **H** between solutions from 3DDOCSEM and DIPOLE1D. (d) Absolute error of phase for **E** and **H**.

3D model results

Fig. 2.12 presents my solutions compared to 3D solutions obtained using the forward modeling algorithm of Li *et al.* (2018) at a frequency of 0.25 Hz. The discrepancy between our responses and solutions obtained by Li *et al.* (2018) is no greater than 2.2% in amplitude for E_y, E_z, and H_x. The absolute error of the phase is less than 1.8° for E_y, E_z, and H_x. I conclude that my forward modeling can produce sufficient accurate responses for the 1D and 3D cases. However, the reader is reminded that the solutions by Li *et al.* (2018) cannot be treated as exact as for analytical 1D solutions, but are used as reference solutions. The discrepancy might derive from the difference in boundary conditions (Dirichlet vs. Perfectly matched layer), the staggering scheme (Electric field components vs. Magnetic field components are on the edges), mesh design, or all of the above.

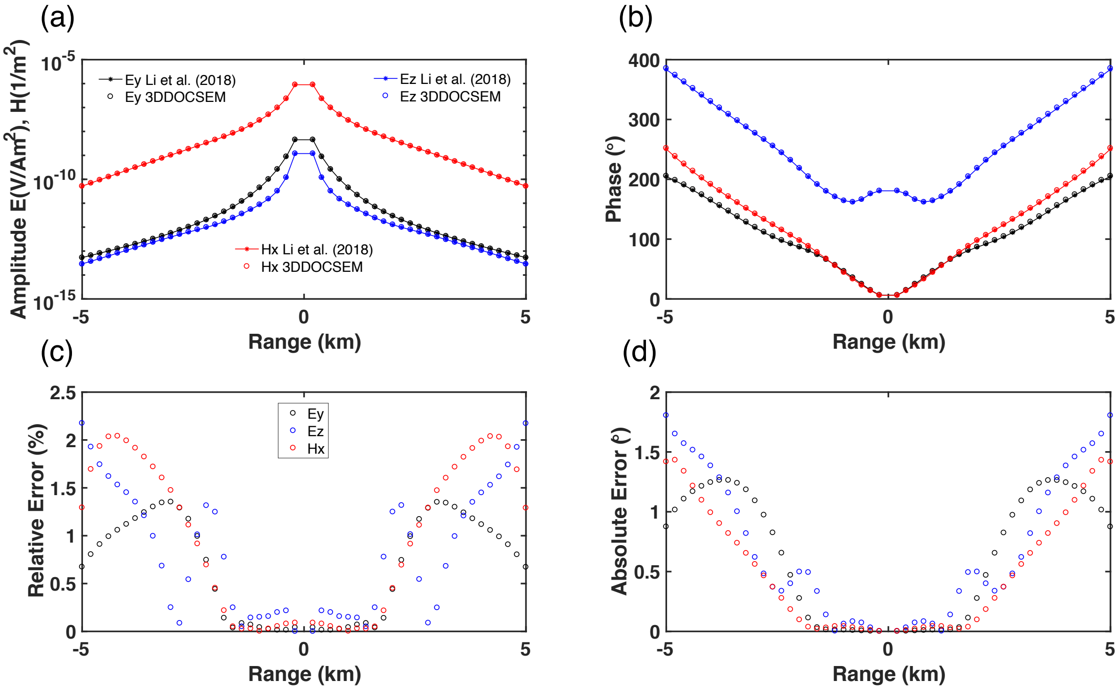

Figure 2.12. Numerical solutions at a frequency of 0.25 Hz. The range shows the transmitter-receiver offset. (a) Amplitude of the electric field **E** (V/Am^2) and magnetic field **H** (1/m^2). (b) Phase of the electric field **E** and magnetic field **H** (°). ○ shows responses from 3DDOCSEM. Solid line shows the responses from Li *et al.* (2018). The colors black, blue and red are for E_y, E_z and H_x. (c) Relative error of amplitude for **E** and **H** between solutions from 3DDOCSEM and responses from Li *et al.* (2018). (d) Absolute error of phase for **E** and **H**.

2.6 Conclusions

I developed a 2D marine ERT forward modeling scheme. The FEM with the unconstructed meshes were applied to the marine 2D ERT forward modeling scheme. The detailed bathymetry can be precisely modeled with unconstructed meshes. The precise modeling of bathymetry enables high-resolution ERT surveys for the near-seafloor exploration. Furthermore, the forward problem was solved with a scattered field approach. The scattered field approach can remove its singularity problems at transmitter positions. Thus, relatively rough meshes can be used near the transmitter positions. The performance of the forward modeling scheme was investigated by comparing forward responses with analytical solution from the two-layer model. It showed the forward modeling scheme could produce enough accurate solutions. The maximum error was less than 2%, which is less than the observation errors.

A 3D marine CSEM forward modeling scheme was also developed. The FDM with the scattered field approach is used for the CSEM forward modeling. Similar to the ERT forward problems, the relatively rough mesh could be used for the modeling due to the scattered field approach. The linear equation in the 3D CSEM modeling was solved by a multicore parallel sparse direct solver PARDISO. The direct solver enables the fast computation of solving forward problems. The performance of the forward modeling scheme was investigated using 1D and 3D examples. Numerical experiments with 1D and 3D examples showed that the forward modeling code could produce accurate solutions at a range of transmitter and receiver less than 10 km.

I conclude that the developed forward modeling schemes can produce accurate solutions efficiently. The inversion algorithms are developed with the forward modeling schemes.

Chapter 3

Development of efficient inversion algorithms

3.1 Introduction

Inversion algorithms convert observed data to model parameters (Fig. 2.1). Interpretations based on inverted images are more reliable than just looking at the data. For both ERT and CSEM surveys, electrical resistivity or conductivity of the sub-seafloor is estimated in inversion procedures. Resistivity distribution can be modeled into 1D, 2D or 3D depending on subsurface geology. There are two approaches to geophysical inverse problems, stochastic and deterministic approaches. The stochastic approach can provide a posterior distribution of the model parameters, making it a good tool to estimate the model uncertainties. Markov Chain Monte Carlo sampling methods have been applied to the 1D inversion of CSEM and DCR data (Ray & Key 2012, Blatter *et al.* 2019). However, the application of a stochastic approach to the multidimensional inversion algorithms of CSEM and ERT data is not yet practical due to the huge computational cost associated with the Monte Carlo sampling methods. On the other hand, the deterministic approach minimizes an objective function using gradient-based methods to seek a model that fits the misfit to a certain threshold. The deterministic approaches have been applied to the multidimensional inversion of EM and ERT data because of the high efficiency (Siripunvaraporn *et al.* 2005, Commer & Newman 2008, Key 2016).

Various deterministic inversion algorithms for CSEM and ERT data such as NLCG (Commer & Newman 2008, Egbert & Kelbert 2012), QN (Haber 2004, Wang *et al.* 2018), and GN (Grayver *et al.* 2013, Schwarzbach & Haber 2013) have been developed. NLCG and QN algorithms are limited memory optimization algorithms. These algorithms can be run on low memory machines but they usually exhibit linear convergence. If the inversion algorithms are developed with direct forward solvers, the limited memory optimization algorithms are not necessarily optimal because the iteration number of inversion is proportional to the expensive factorization of the direct solvers. GN algorithm shows much faster quadratic convergence, thus it is well suitable for a combination of direct solvers for the forward modeling. Using the above optimization methods, one must select the regularization parameter in advance of running inversion. The convergence rate also strongly depends on the parameter in NLCG and QN.

The Occam algorithm, a variant of GN, specifies the minimum norm model with a specific misfit by automatically adjusting the regularization parameter (Constable *et al.* 1987). Because of greater robustness than the algorithms above, the Occam algorithm has been used for various electromagnetic data and for 3D CSEM data. The GN type inversion including Occam algorithm requires solving normal equation $M \times M$ in the mode-space approach or $N \times N$ in the data-space approach, where M and N

respectively denote the quantities of model and data parameters. Zhang & Key (2016) applied the 3D mode-space Occam inversion algorithm to CSEM data. However, M is frequently larger than N for the 3D CSEM inversion (*e.g.* M=2,463,768 and N=16,088 in Wang *et al.* 2018). The data-space approach can reduce both CPU time and memory if $M < N$. Siripunvaraporn *et al.* (2005) reduced computation costs by application of the data-space approach to the 3D Occam inversion algorithm for MT data.

The Occam inversion algorithm is used for both ERT data and CSEM data due to its robustness. For the 2D inversion of ERT data, the number of the model parameters is comparable with the number of data. I apply the model-space approach to the 2D inversion algorithm of ERT data. For the 3D inversion of CSEM data, the number of the model parameters is frequently much larger than the number of data. I apply the data-space approach to the 3D inversion algorithm of CSEM data.

3.2 2D towed marine ERT inversion algorithm

3.2.1 Model-space Occam inversion algorithm

Occam inversion algorithm seeks the model with minimum norm at an appropriate misfit revel. A brief review of the Occam inversion algorithm is given below. The regularized inverse problem seeks to minimize the functional

$$U = (\boldsymbol{m} - \boldsymbol{m}_0)^T \mathbf{C}_m^{-1}(\mathbf{m} - \mathbf{m}_0) + \lambda^{-1}\{(\mathbf{d} - \mathbf{F}[\mathbf{m}])^T \mathbf{C}_d^{-1}(\mathbf{d} - \mathbf{F}[\mathbf{m}]) - \chi_*^2\} \qquad \textbf{(3-1)}$$

Here $\mathbf{m}$ is a vector $\log\sigma$, $\mathbf{m}_0$ a prior model, $\mathbf{C}_m$ a model covariance matrix, $\mathbf{d}$ stands for the observed apparent resistivity data as $\log\rho_a$, $\mathbf{F}[\mathbf{m}]$ the forward model response, $\mathbf{C}_d$ a data covariance matrix, $\chi*$ the desired level of misfit, and λ^{-1} a Lagrange multiplier. The standard method for minimizing U in eq. (3-1) is to take the derivative to model and set it equal to zero. Because the derivative of $\mathbf{F}[\mathbf{m}]$ is nonlinear in ERT methods, the resulting equation is solved iteratively by creating a sequence of models, each of which gradually provides a better fit to the data. After linearizing about an initial model $\mathbf{m}_k$, the equation for the next model in the sequence $\mathbf{m}_{k+1}$. The model update iterations are continued in this manner until the target misfit $\chi*$ has been reached. The resulting equation for the model-space approach proposed by Constable *et al.* (1987) is

$$[\lambda \mathbf{C}_m^{-1} + \mathbf{J}_k^T \mathbf{C}_d^{-1} \mathbf{J}_k](\boldsymbol{m}_{k+1} - \mathbf{m}_0) = \mathbf{J}_k^T \mathbf{C}_d^{-1} \hat{\mathbf{d}}_k \qquad \textbf{(3-2)}$$

where

$$\hat{\mathbf{d}}_k = \mathbf{d} - \mathbf{F}[\boldsymbol{m}_k] + \mathbf{J}_k(\boldsymbol{m}_k - \mathbf{m}_0) \qquad \textbf{(3-3)}$$

Expression $\mathbf{J}_k$ is the linearized model response gradient or Jacobian matrix.

3.2.2 Jacobian matrix

The Jacobian matrix $N \times M$. stores gradient of the responses with respect to its model parameters.

$$\mathbf{J} = \frac{\partial \mathbf{F}[\mathbf{m}]}{\partial \mathbf{m}} \qquad \textbf{(3-4)}$$

In this ERT inversion algorithm, the forward responses are $\log\rho_a$ and model parameters are $\log\sigma$. The element of Jacobian is rewritten as

$$\mathbf{J}^{ij} = -\frac{\sigma_j}{\phi^{A_i,M_i} - \phi^{A_i,M_i} - \phi^{A_i,M_i} + \phi^{A_i,M_i}} \sum_{p=1}^{n} g_p \frac{\partial}{\partial \sigma_j}\left(\tilde{\phi}_{k_{y_p}}^{A_i,M_i} - \tilde{\phi}_{k_{y_p}}^{A_i,M_i} - \tilde{\phi}_{k_{y_p}}^{A_i,M_i} - \tilde{\phi}_{k_{y_p}}^{A_i,M_i}\right) \quad \textbf{(3-5)}$$

The derivative is

$$\frac{\partial}{\partial \sigma_j} \tilde{\boldsymbol{\phi}}_{k_{y_p}}^{A_i} = -\mathbf{K}^{-1} \frac{\partial \mathbf{K}}{\partial \sigma_j} \tilde{\boldsymbol{\phi}}_{k_{y_p}}^{A_i} \quad \textbf{(3-6)}$$

The interesting points are only two point *M* and *N*. By multiplying interpolation operator **Q** to eq. (3-6),

$$\frac{\partial}{\partial \sigma_j} \tilde{\boldsymbol{\phi}}_{k_{y_p}}^{A_i} = -\boldsymbol{Q}\mathbf{K}^{-1} \frac{\partial \mathbf{K}}{\partial \sigma_j} \tilde{\boldsymbol{\phi}}_{k_{y_p}}^{A_i} \quad \textbf{(3-7)}$$

Each row of **Q** has one non-zero element that correspond to the position electrodes and its value is 1. When coefficient matrix is symmetric, equation can be transposed.

$$\frac{\partial}{\partial \sigma_j} \tilde{\boldsymbol{\phi}}_{k_{y_p}}^{A_i} = -\mathbf{K}^{-1}\boldsymbol{Q}^T \frac{\partial \mathbf{K}}{\partial \sigma_j} \tilde{\boldsymbol{\phi}}_{k_{y_p}}^{A_i} \quad \textbf{(3-8)}$$

3.2.3 Model covariance

The model roughness operator **R** stabilizes the inversion by providing a measure of the model variations. In this thesis, the roughness operator **R** gives the differences of adjacent parameter cells. I consider the k_{th} parameter cell and its adjacent parameter cell through its i_{th} face. The number of the k_{th} parameter cell is inputted into diagonal. The i_{th} face is inputted -1. This term gives a smoothness constraint to stabilize the inversion.

$$\mathbf{C}_m^{-1} = \mathbf{R}^T\mathbf{R} \quad \textbf{(3-9)}$$

3.3 Synthetic data examples for 2D marine ERT inversion algorithm

3.3.1 SMS model

The performance of the 2D marine ERT inversion algorithm was investigated using synthetic data. I consider a model of a homogeneous half-space of 1 Ohm-m containing a 0.1 Ohm-m conductive object simulating a SMS deposit (Fig. 3.1a). The seawater of resistivity 0.3 Ohm-m has about 1000 m depth. The ERT system shown in Fig. 1.6 is towed at a depth of 990 m. Apparent resistivity data is calculated at every 10 m in horizontal distance, resulting in total *N*=641 apparent resistivity data. The inversion domain is limited to the interesting seafloor region, excluding sea-layer and resulting in *M*=10,175 unknown model parameters. The starting model for the example is a homogeneous half-space with a resistivity of 1 Ohm-m. 2% Gaussian noise was added to the data and the error bar was set to 2% of the data. The target RMS misfit is 1.0, which means that the averaged misfit is within the assumed error.

The initial RMS misfit for the starting model was 18.1. The inversion reached the target misfit at three iteration numbers (Phase I) and one additional iteration was conducted to remove the unnecessary structures (Phase II). The inverted model from the synthetic data is displayed (Fig. 3.1b). The result shows the inversion algorithm sufficiently recovered positions and resistivity values of the conductive anomaly. The resistivity structure of the conductive anomaly is spread vertically compared to the true structures. The resistivity values of the recovered anomaly are closer to the real value in the shallow parts than the deeper parts. This is due to the smaller sensitivity to deep parts.

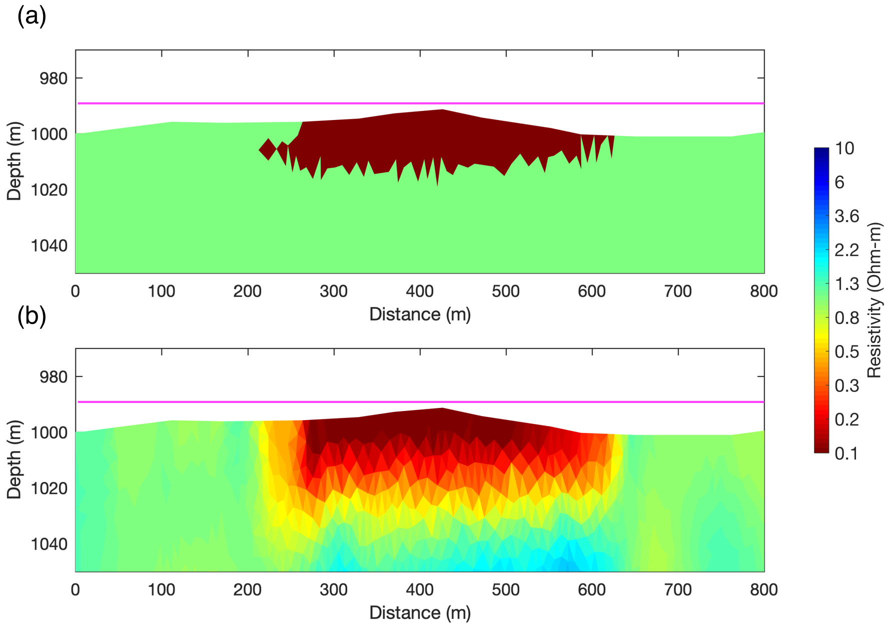

Figure 3.1. Hypothetical SMS model with seafloor topography. 0.1 Ohm-m conductive object simulating a SMS deposit is embedded into a homogeneous half-space of 1 Ohm-m. The depth is from the sea surface. Magenta lines show a position of the towed system (a) True model used for generating synthetic data sets. (b) Inverted model from the synthetic ERT data.

3.3.2 Influence of cable length on penetration depth

Distribution of SMS is partly revealed by high-resolution bathymetry data and drilling surveys (JOGMEC 2013). A realistic SMS model based on drilling results in the Izena hydrothermal field by JOGMEC (2013) is used for the generation of synthetic tests. The synthetic model consists of sea-water and half-space and two conductive anomalies embedded into a half-space model (Fig. 3.2). The mound SMS is a trapezoid (upper side is 15 m, lower side is 105 m, and height is 30 m). The buried SMS is distributed as a step-like structure, whose width is 300 m. The resistivity of seawater is 0.316 Ohm-m, sediment is 1.0 Ohm-m and SMS is 0.21 Ohm-m. The position of the towed system is shown in Fig. 3.2. The towed system is rolled up and down for crossing the mound SMS. An angle of the towed system is

±45° when it is rolled up and down. Data obtained during the time is not used because the towed cable is not straight. Apparent resistivity data is obtained at each 5 m in horizontal distance, resulting in total of 903 apparent resistivity data. The apparent resistivity data is contaminated with Gaussian random noises whose standard deviation is shown in Table. 3.1.

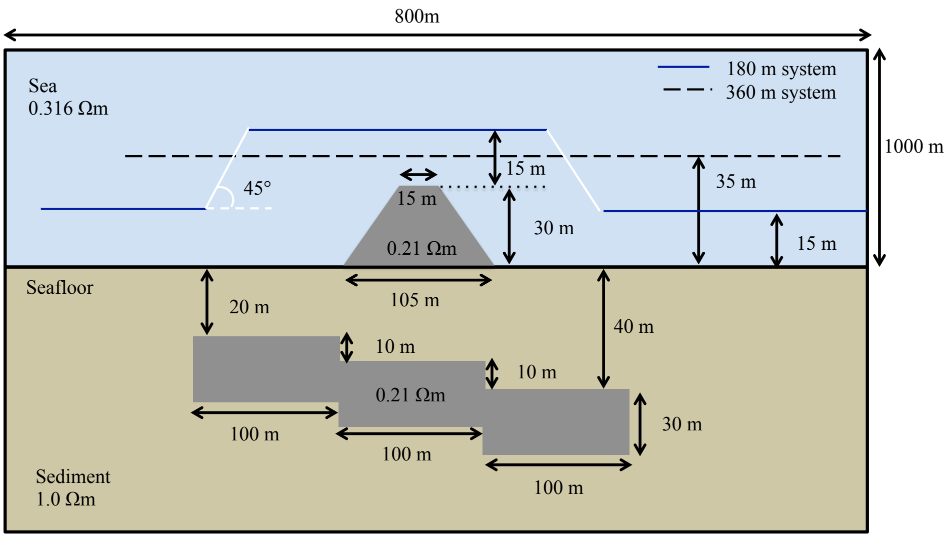

Figure 3.2. A hypothetical model including complex seafloor topography and more realistic SMS distribution. Blue and white lines show the position of 180 m length towed system. When the system is located along the white lines, the towed cable behind the system cannot be straightly stretched, therefore the data along the white lines are not used. The black dashed line shows a position of 360 m length towed system.

Table 3.1. Electrodes sets and errors for the synthetic tests.

Electrode pairs	P1-P2	P2-COM1	COM1-P3	P3-P4	P5-P6	P6-COM2	COM2-P7	P7-P8
n level	2	3	4	5	6	7	8	9
TxRx distance (m)	30	45	60	75	90	105	120	135
Data standard errors (%)	1.0	1.5	1.5	2.0	2.0	2.5	2.5	3.0

The Occam inversion algorithm developed by Ishizu *et al.* (2019b) is applied to the synthetic data. The FDM is used for the forward modeling algorithm. The synthetic model is discretized into the mesh of 180 × 84 (horizontal × vertical direction). A 0.8 Ohm-m half-space was used as an initial model and prior models. The initial RMS misfit for the starting model was 6.6. After the second iteration RMS reached 1. Phase II in the Occam inversion algorithm is conducted with one additional iteration. The inverted model is shown in Fig. 3.3a. The inversion algorithm sufficiently recovered the mound SMS model. The shape and value are similar to the true structure. The buried SMS was not recovered due to the weak sensitivity of the ERT system to deeply buried structures.

To image the buried SMS using the towed ERT system, the cable is extended to 360 m from 180 m. In this test, C1 and C2 are located 15 m and 30 m behind of towed system and the potential electrodes are extended from 60 m to 360 m with 15 m spacing leading to total of 21 electrodes points. The apparent resistivity data are obtained at every 5 m in a horizontal direction, which is the same data spacing to the previous test. The model shown in Fig. 3.2 is discretized 183 × 94 (horizontal × vertical direction). The number of calculated apparent resistivity data is 1,800. The apparent resistivity data was contaminated with Gaussian random noises. Noise revels for the data with potential electrodes from 60 m to 180 m are shown in Table 3.1. Noise revels for the data with potential electrodes from 180 m to 360 m are 3% of the calculated apparent resistivity. A 0.8 Ohm-m half-space was used as an initial model and prior models. The initial RMS misfit for the starting model was 8.7. The inversion reached the target misfit at three iteration numbers (Phase I) and one more iteration was conducted to obtain minimum norm with the target misfit. (Phase II). The inverted model is shown in Fig. 3.3b. The buried SMS deposit was imaged in addition to the mound SMS. This result showed the sensitivity to the buried SMS was increased by extending the cable length 180 m to 360 m. However, the resolution to buried SMS is still low and the resistivity is 0.55 Ohm-m. The concentration of the electric current into the mound SMS obstructs its deep penetration. The results show that extending towed cable is effective to image the buried SMS, but the buried SMS has a much lower resolution than the mound SMS.

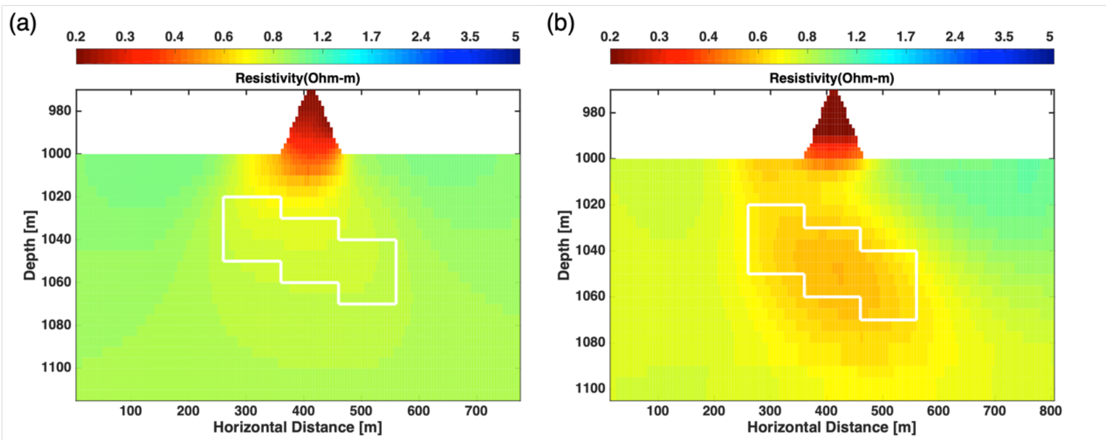

Figure 3.3. Inversion result using synthetic data generated from the model in Fig. 3.2. (a) A towed cable with a length of 180 m is used. (b) A long towed cable with a length of 360 m is used. Solid white lines indicate the boundaries of the buried low resistive body. The depth is from the sea surface.

However, towing long cable at a low altitude from the seafloor is not simple in the complex bathymetry. Precise towing plan based on a detailed bathymetry map is necessary for towing long cable at low attitude. With the long cable, the adjustment of the towed height causes slack of the cable. Thus, it is also required to monitor the cable attitude in real-time. On the other hand, combination with CSEM surveys can increase the penetration depth. The shallow resistivity structures below the seafloor can be imaged using the deep towed ERT system and deep the seafloor can be imaged using CSEM surveys with stationary receivers on the seafloor.

3.4 3D inversion algorithm of CSEM survey

3D CSEM inversion algorithm is developed using the data-space Occam algorithm because of its robustness and efficiency. A noteworthy merit of the algorithm is the great reduction of matrix dimensions to $N \times N$ size using the following methods.

3.4.1 Data-space Occam inversion algorithm

The data-space approach (Siripunvaraporn & Egbert 2000, Siripunvaraporn *et al.* 2005, Kordy *et al.* 2016) replaces eq. (3-2) by a linear equation with N unknowns. When eq. (3-2) is left-multiplied by $\mathbf{C}_m$, one obtains

$$\boldsymbol{m}_{k+1} - \boldsymbol{m}_0 = \mathbf{C}_\mathrm{m}\mathbf{J}_k^T\beta_{k+1} \quad \textbf{(3-10)}$$

where β_{k+1} is an unknown expansion coefficient vector of the basis functions $\mathbf{C}_m\mathbf{J}_k^T$

$$(\lambda\boldsymbol{C}_\mathrm{d} + \mathbf{J}_k\mathbf{C}_\mathrm{m}\mathbf{J}_k^T)\beta_{k+1} = \hat{\mathbf{d}}_k \quad \textbf{(3-11)}$$

Similarly to the standard model-space Occam inversion algorithm, in the data-space approach, I solve for β_{k+1} using eq. (3-11), update the model using eq. (3-10), and then compute the misfit. eq. (3-10), update the model, and then compute the misfit. The solutions obtained from both approaches, *i.e.*, from eq. (3-2) for the model-space approach and from eqs. (3-11) and (3-10) for the data-space approach, are expected to be identical if all parameters used are the same. The major difference between eqs. (3-2) and (3-11) is that the dimensions of the system of equations to be solved can be reduced from $M \times M$ in the model-space approach to $N \times N$ in the data-space approach. In fact, N is usually much less than M in practical cases for the 3D marine CSEM inversion problem. This transformation greatly reduces computational costs of both memory and CPU time (Siripunvaraporn & Egbert 2000, Siripunvaraporn *et al.* 2005).

At every iteration of the Occam algorithm, I search for the λ that gives the model with the minimum misfit in phase I or at the desired misfit in phase II (Constable *et al.* 1987, Siripunvaraporn & Egbert 2000, Key 2009). In phase I, the Nelder–Mead search method proposed by (Nelder & Mead 1965) through $\log_{10}\lambda$ is used to find λ with the minimum misfit. In phase II, Brent's method is used to find the largest λ providing the desired level of the misfit. If the minimum search fails to find a model with a lower misfit, then a reduced step of updating the model is taken using model $\mathbf{m}'_{k+1}$ as shown below.

$$\mathbf{m}'_{\mathrm{k}+1} = \alpha\mathbf{m}_{\mathrm{k}+1} + (1-\alpha)\mathbf{m}_{\mathrm{k}} \tag{3-12}$$

Initially, step size α is set as 1. Then α is successively cut in half until a better-fitting model is obtained.

3.4.2 Jacobian matrix

By taking the derivative of eq. (2-48) with respect to the model parameters, one can obtain the sensitivity matrix as

$$\mathbf{J} = \frac{\partial\mathbf{F}[\mathbf{m}]}{\partial\mathbf{m}} = \frac{\partial\mathbf{Q}^{p}}{\partial\mathbf{m}}\mathbf{E}^{p} + \frac{\partial\mathbf{Q}^{p}}{\partial\mathbf{m}}\mathbf{E}^{\mathrm{p}} + \mathbf{Q}^{\mathrm{s}}\mathbf{A}^{-1}\mathbf{G} \tag{3-13}$$

where **G** is defined as presented below.

$$\mathbf{G} = \left[\left(-\frac{\partial\mathbf{A}}{\partial\mathrm{m}_1}\mathbf{E}\right)\left(-\frac{\partial\mathbf{A}}{\partial\mathrm{m}_2}\mathbf{E}\right)\cdots\left(-\frac{\partial\mathbf{A}}{\partial\mathrm{m}_{N_P}}\mathbf{E}\right)\right] \tag{3-14}$$

This formulation would require M times forward solutions to compute the sensitivity matrix. However, by transposing eq. (3-13), because **A** is symmetric, I obtain the following.

$$\mathbf{J}^{T} = (\mathbf{E}^{p})^{T}\left(\frac{\partial\mathbf{Q}^{p}}{\partial\mathbf{m}}\right)^{T} + \left(\mathbf{E}^{S}\right)^{T}\left(\frac{\partial\mathbf{Q}^{S}}{\partial\mathbf{m}}\right)^{T} + (\mathbf{G})^{T}(A)^{-1}\left(\mathbf{Q}^{S}\right)^{T} \tag{3-15}$$

The sensitivity matrix is obtainable by solving the transposed discrete system **A** N times. This is the usual 'reciprocity' trick for the efficient calculation of sensitivities (Egbert & Kelbert 2012). The full sensitivity matrix is calculated using the sparse direct solver. Multiple forward solutions can be computed cheaply using the direct solvers. Therefore, computation of the full sensitivity matrix becomes affordable (Grayver *et al.* 2013). Once the sensitivity matrix is factorized, it can be stored and reused for the parameter searching process of λ at each iteration in the Occam inversion algorithm.

3.4.3 Model covariance

In the data-space approach, model covariance $\mathbf{C}_m$ is necessary for computation instead of its inverse $\mathbf{C}_m^{-1}$ in a model-space counterpart. Two approaches are used with model covariance. In one approach, model covariance $\mathbf{C}_m$ is defined directly assuming some correlation functions such as Gaussian function (Siripunvaraporn *et al.* 2005). In the other approach, one defines the inverse of model covariance $\mathbf{C}_m^{-1}$, which is often made using the first or second derivative of smoothing. Then, one obtains the model covariance $\mathbf{C}_m$ by inverting the matrix $\mathbf{C}_m^{-1}$ (Kordy *et al.* 2016, Usui *et al.* 2017, Minami *et al.* 2018). The latter approach is applied to our inversion. The model covariance is never constructed explicitly. The product with sensitivity matrix $\mathbf{C}_m\mathbf{J}_k^T$ is necessary for the data-space approach. The regularization $\mathbf{C}_m^{-1}$ is defined as the first derivative roughness penalty. Regularization is non-negative definite and singular. To make it positive definite, a small value ε is added to its diagonal before inversion (Kordy *et al.* 2016). For inverting the matrix $\mathbf{C}_m^{-1}$ and multiplying to $\mathbf{J}_k^T$, PARDISO is used.

3.5 Synthetic data examples for 3D marine CSEM inversion algorithm

The performance of our CSEM inversion algorithm was investigated using synthetic data. A model for generating the synthetic CSEM data is a homogeneous half-space containing conductive and resistive objects, respectively simulating gas hydrate and a SMS deposit. To illustrate the ability of the inversion algorithm to image more realistic SMS structures, the other model is a homogeneous half-space containing a conductive pyramid and reverse pyramid structures, respectively simulating mound and stock-work SMS.

3.5.1 Two-block model

Fig. 3.4a shows a model of a homogeneous half-space of 1 Ohm-m containing two anomalous objects for generating synthetic data. A 10 Ohm-m resistive and 0.1 Ohm-m conductive box with 500 × 500 × 200 m dimensions is embedded with its top at 1,100 m depth. The resistive and conductive anomalies respectively simulate gas hydrate and SMS deposits. An air layer of resistivity 10^8 Ohm-m is present at the top of the model. Seawater depth with resistivity of 0.3 Ohm-m is 1,000 m. Sediments below the seafloor are homogeneous, with resistivity of 1 Ohm-m.

First, 28 receivers are deployed on the seafloor to record the electric fields. Then, 70 transmitters using an HED oriented along the y-direction are towed at a height of 50 m above the seafloor. Observed data were generated by forward modeling responses on a grid of 67 × 67 × 58 cells including several boundary cells to minimize boundary effects. For the horizontal cells, a 50 m grid was used in the interest region. I appended several boundary cells at each side, growing in size at a stretching factor of 2.0. For the vertical grid, fine grids of 20 m spacing were used in the region of 1,000–1,400 m below the sea surface. The grid size increases gradually with increasing distance from the transmitters.

The inversion domain is limited to the interesting seafloor region, excluding boundary cells and air, and resulting in M=142,175 unknown model parameters. The starting and prior model for the example is a homogeneous half-space with resistivity of 1 Ohm-m. The inputted data use a combination $\log_{10}$ scaled amplitude and linear scaled phase of E_y. The combination can accelerate inversion convergence in the inversion iteration compared to a combination of real and imaginary of an electric field (Wheelock *et al.* 2015). The component for source–receiver distances larger than 300 m at frequencies of 0.1, 0.5, and 3.0 Hz results in a N=11,376 data number. 3% Gaussian noise was added to the data. The error bar was set to 3% of the data. The target RMS misfit is 1.0, which indicates that the averaged misfit is within the assumed error.

The initial RMS misfit for the starting model was 7.2. Before inverting $\mathbf{C}_m^{-1}$, the small value $\varepsilon=10^{-4}$ was added to its diagonal to make it positive definite. The inversion reached the target misfit at three iteration numbers (Phase I). Then two more iterations were conducted to remove the unnecessary structures (Phase II). Vertical slices of the inverted model from the synthetic data are displayed in Fig.

3.5b. Results show that the inversion algorithm sufficiently recovered positions and resistivity values of both anomalies. The tops of both anomalies are clearly distinguishable from the homogeneous half-space. Horizontal shapes of both anomalies of top parts were also recovered well. The imaged bottom of the anomalies is not as clear as the top. This low-resolution feature for deeper parts is typical of electromagnetic exploration. Adding more frequency data might help the inversion algorithm constrain the bottom depth. The imaged conductive anomaly is larger than the true structure. The imaged resistive anomaly is smaller than the true structure. The result implies that the inversion algorithm might overestimate conductive anomalies and underestimate restive anomalies.

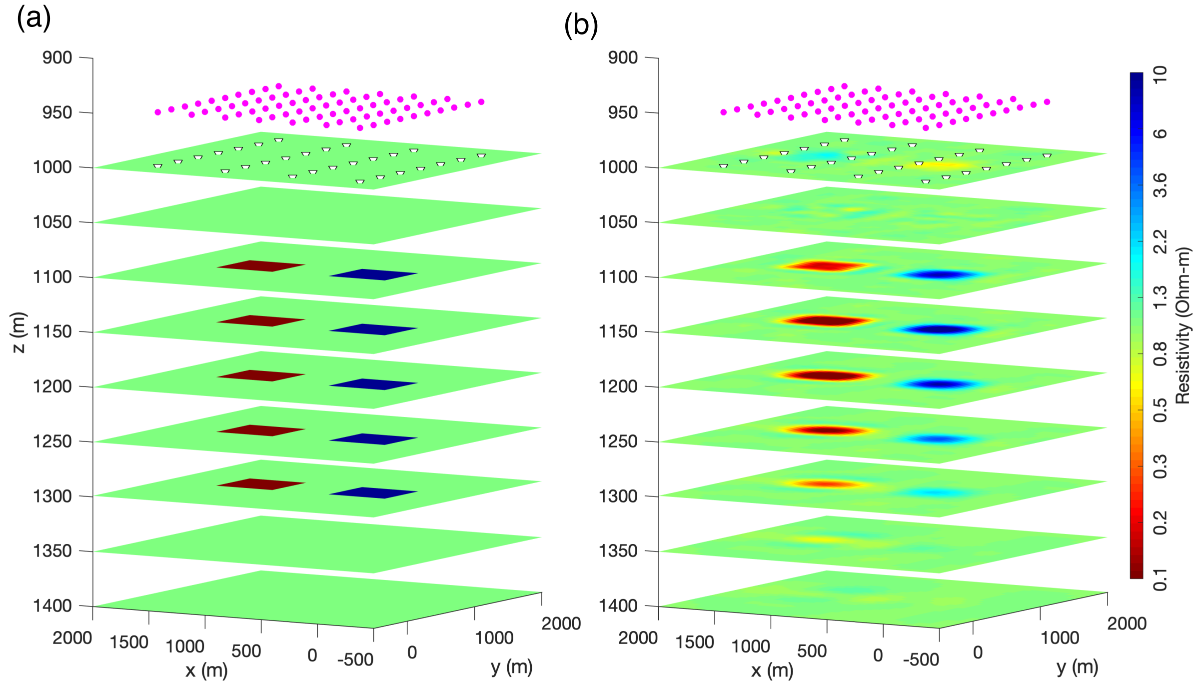

Figure 3.4. (a) Vertical slices of the model used for demonstrating the inversion test. A 10 Ohm-m resistive and 0.1 Ohm-m conductive box with dimensions 500 × 500 × 200 m are embedded with its top at a depth of 1100 m. *z* is depth from the sea surface. The seafloor is at a depth of 1000 m. White triangles and pink circles indicate receivers and transmitters, respectively. (b) Inverted model from the synthetic data.

The model number M=142,175 is much larger than the data number N=11,376. The data-space approach can reduce the computation time in this case. The inversion algorithm includes making the sensitivity matrix and searching the process for λ at each iteration. Each search process requires about five trial values of λ leading to five implementations of the forward modeling algorithm. Solving the discrete equations eq. (3-13) with PARDISO includes reordering, factorization, and a solving process. The reordering, factorization, and the solving process respectively took 9.30 s, 143.9 and 79.9 s (total 233.2 s) when the matrix size was 849,355 × 849,355 and the RHS number was 126. The forward modeling algorithm requires solving of the discrete equations at each frequency. Discrete equations are solved three times corresponding to the frequency number. An implementation of the forward modeling took about 700 s. Fast forward modeling algorithm using PARDISO enables an efficient inversion algorithm. The computation time of the inversion at each iteration was around 1 hour. A model space approach entails considerable computational costs of both memory and CPU time. By transformation from model space M=142,175 to data space N=11,376 its computational costs are reduced considerably, allowing us to invert 3D CSEM datasets in a short time.

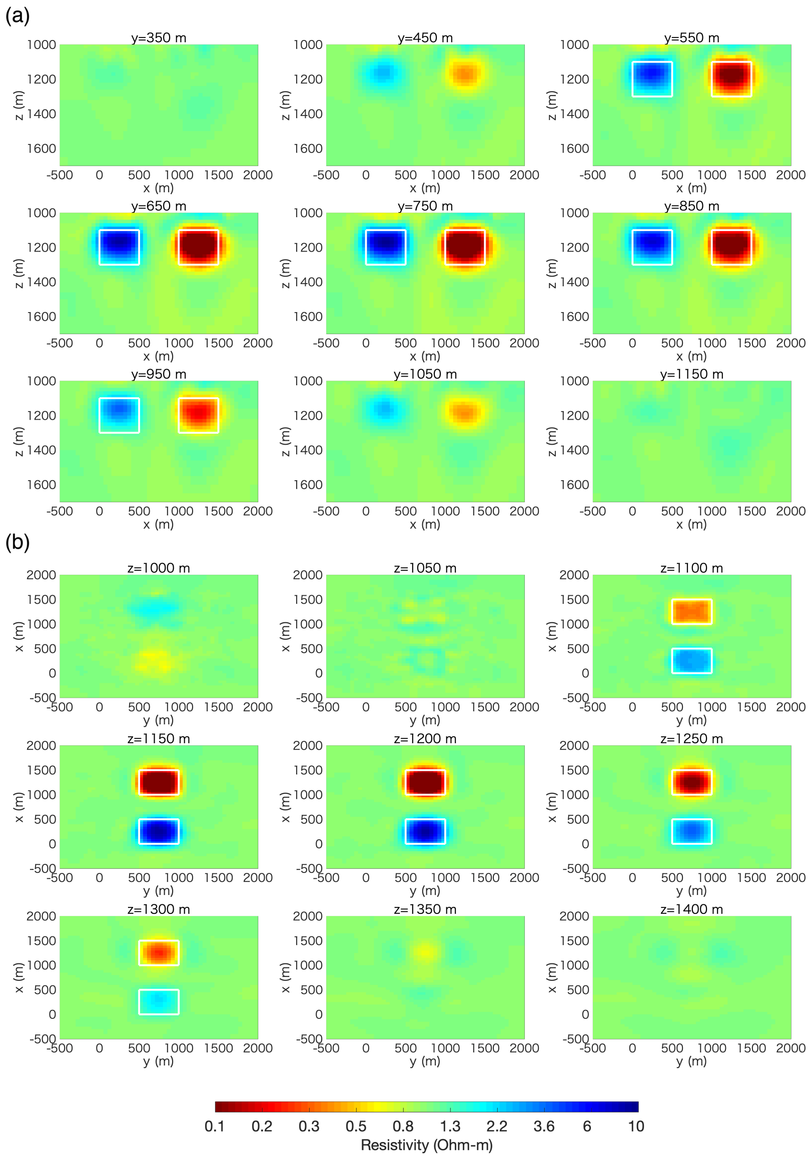

Figure 3.5. Cross section of the inverted model shown in Fig. 3.4. Slices of the model in (a) y direction, (b) z direction. Solid white lines indicate boundaries of the resistive and conductive box. z is depth from the sea surface (z = 0 m.). The seafloor is at a depth of z = 1000 m.

3.5.2 Pyramid model

The horizontal size of the conductive anomaly as SMS of the earlier example is the same in the vertical direction. For a more realistic SMS model, I respectively consider conductive pyramid and reverse pyramid structures simulating mound and stock-work SMS. This model is also used for showing the ability of the inversion algorithm to recover the top and bottom of anomalies for the different sizes. Fig. 3.5a presents a model of a homogeneous half-space of 1 Ohm-m containing a 0.1 Ohm-m pyramid and a 0.1 Ohm-m reverse pyramid. The pyramids with dimensions 500 × 500 × 200 m are embedded with the top at 1,100 m depth. An air layer of resistivity 10^8 Ohm-m is present at the top of the model. Seawater depth with resistivity of 0.3 Ohm-m is 1,000 m. The survey configuration for generating data is the same as in a test presented in Fig. 3.4. Here, 3% Gaussian noise was added to the data. The error bar was set to 3% of the data.

The initial RMS misfit for the starting model was 5.5. The inversion reached the target misfit at four iterations (Phase I). Then one more iteration was conducted to remove the unnecessary structures (Phase II). Vertical slices of the inverted model from the synthetic data are displayed in Fig. 3.6b. The top of the pyramid structure on the left side of Fig. 3.6b with dimensions of 500 × 500 × 40 m can be imaged similarly to the preceding section. The resistivity value and shape are close to the real structure. However, the top of the reverse pyramid structure on the right side with dimensions of 100 × 100 × 40 m was poorly resolved. The recovered resistivity value is around 0.5 Ohm-m. The value might lead to underestimation of the SMS existence.

The bottom of the reverse pyramid structure on the left side with dimensions of 100 × 100 × 40 m was not imaged. The bottom of the pyramid structure on the right side with dimensions of 500 × 500 × 40 m was imaged well. Results showed a small target with dimensions of 100 × 100 × 40 m, which was poorly imaged at 100 m depth. It could not be imaged at all at 300 m depth. The results imply that the ability of the inversion algorithm for recovering target structures depends strongly on the structure size and depth. On this CSEM array, where transmitters and receivers are situated respectively in the seawater and on the seafloor, electromagnetic attenuation limits the sensitivity of small features at depth. Sensitivity to recovering small features at depth can be improved by deploying transmitters and receivers near the targets (Wilt *et al.* 1995). That requires boreholes for deploying transmitters and receivers near the target, leading to an increase in survey costs.

In addition to the two models, the inversion algorithm was applied to synthetic data generated from models of several kinds to test the efficiency of our code. Based on the test results, I conclude that our inversion algorithm is ready to perform with actual field data.

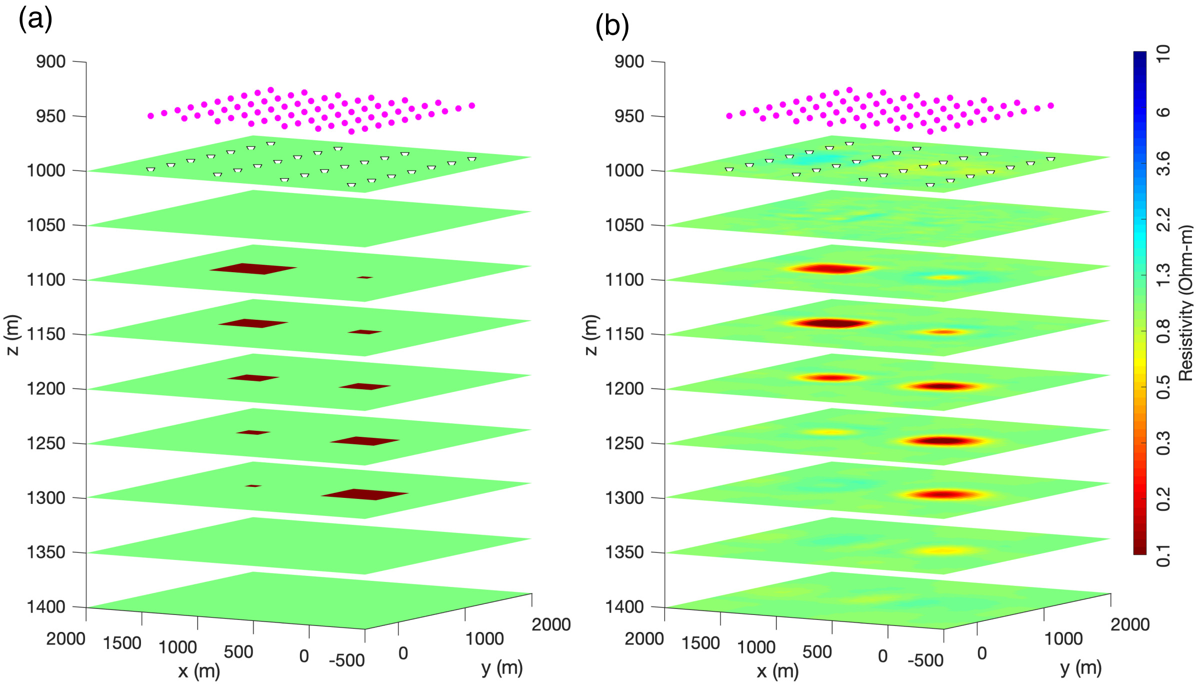

Figure 3.6. (a) Vertical slices of the pyramid model used for the demonstrating the inversion test. A 0.1 Ohm-m conductive pyramid and the reverse are embedded into 1.0 Ohm-m half-space. The pyramids with dimensions 500 × 500 × 200 m are embedded with its top at a depth of 1100 m. White triangles and pink circles indicate receivers and transmitters, respectively. z is depth from the sea surface. The seafloor is at a depth of 1000 m. (b) Inverted model from the synthetic data.

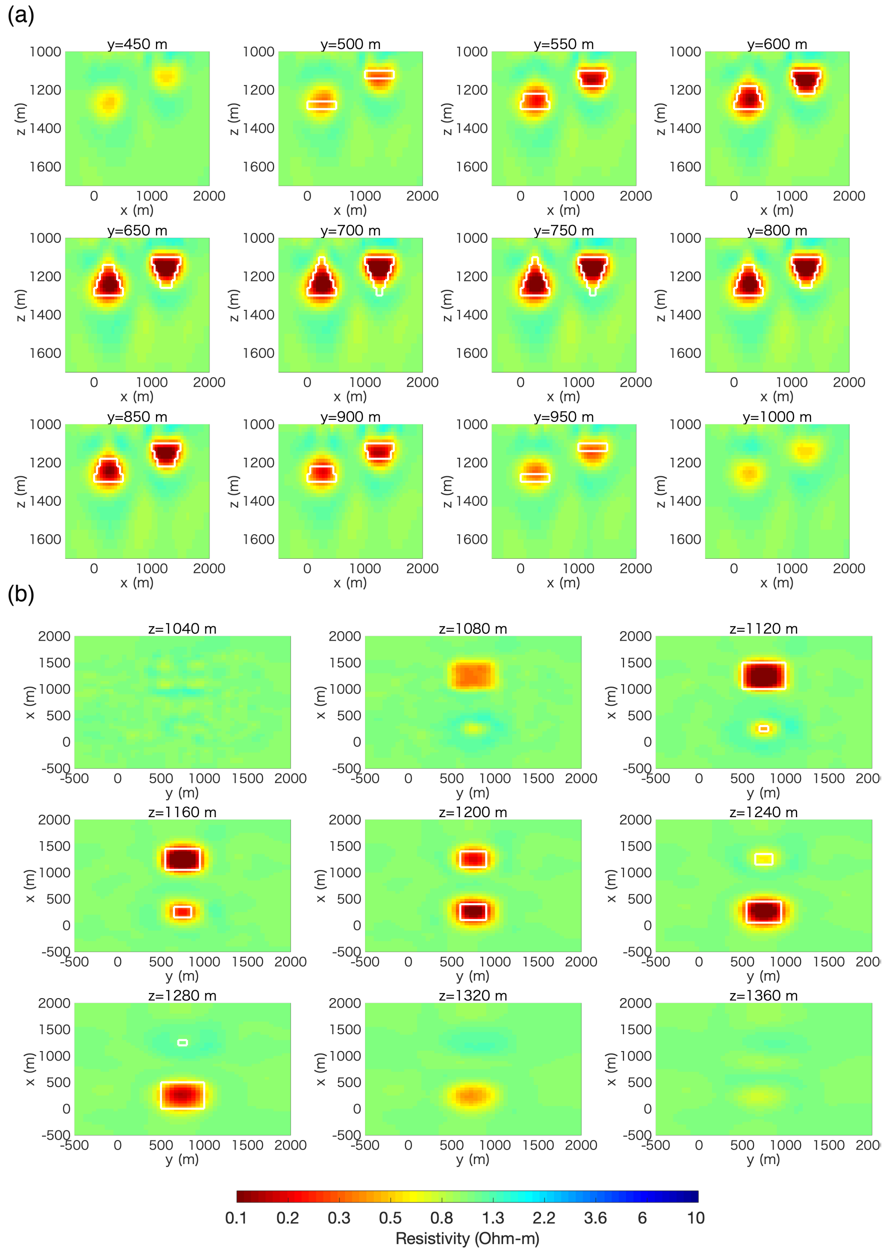

Figure 3.7. Cross section of the inverted model shown in Fig. 3.6. Slices of the model in (a) y direction, (b) z direction. Solid white lines indicate the boundaries of the pyramid and its reverse pyramid. z is depth from the sea surface (z = 0 m.). The seafloor is at a depth of z = 1000 m.

3.5.3 Hydrocarbon model

CSEM surveys in the frequency domain have been used to investigate resistivity structures for the exploration of hydrocarbon reservoirs (Eidesmo *et al.* 2002, Yamane *et al.* 2009, Hesthammer *et al.* 2010, Myer *et al.* 2015). In this subsection, the performance of the inversion algorithm for imaging deeply buried hydrocarbon reservoirs are investigated using the synthetic data. I consider a model of a homogeneous half-space of 1.0 Ohm-m containing a shallow and a deep reservoir (Fig. 3.8a). A 20 Ohm-m shallow reservoir with dimensions 2000 × 2000 × 200 m is embedded with its top at a depth of 1500 m. A 50 Ohm-m deep reservoir with dimensions 4000 × 4000 × 300 m is embedded with its top at a depth of 3000 m. An air layer of resistivity 10^8 Ohm-m is present at the top of the model. The seawater of resistivity 0.3 Ohm-m has 1000 m depth.

200 transmitters using a HED oriented along y-direction are towed at height 50 m above the seafloor. 21 receivers are deployed on the seafloor for recording the electric fields. I generate observed data by the forward modeling scheme on a grid of 62 × 62 × 67 cells including several boundary cells to minimize boundary effects. For the horizontal cells, a 200 m grid was used in the interest region. I append several boundary cells at each side, growing in size at a stretching factor of 2.0. For the vertical grid, fine grids of 50 m were used in the region from 1000 m to 2000 m below the sea surface. The grid size gradually grows with increasing distance from the transmitters.

The inversion domain is limited to the interesting seafloor region, excluding boundary cells, air and resulting in M=120,050 unknown model parameters. The starting model for the example is a homogeneous half-space with a resistivity of 1 Ohm-m. The data are inverted using a combination $\log_{10}$ scaled amplitude and linear scaled phase of E_y. The component for source-receiver distances larger than 300 m at frequencies of 0.2 and 1.0 Hz results in N=16, 548 data number. 2% Gaussian noise was added to the data and the error bar was set to 2% of the data. The target RMS misfit is 1.0, which means that the averaged misfit is within the assumed error.

The initial RMS misfit for the starting model was 8.5. The inversion reached the target misfit at eight iteration numbers (Phase I) and one more iteration was conducted to remove the unnecessary structures (Phase II). Y slices of the inverted model from the synthetic data are displayed in Fig. 3.8b. The inversion algorithm could delineate both anomalies. However, the inverted structures are bigger than true shapes. This is due to low resolution at deep area combined with the smoothness constraint. Conductive artifacts were recovered above the deeply buried resistor. Conductive artifacts were also recovered above deeply buried resistors in other CSEM inversion applications (Key 2009). The smoothing cut is effective to recover thin deeply buried resistors properly and remove the conductive artifacts.

The time and cost of the CSEM surveys strongly depend on the number of deployed receivers. 21 receivers (7 receivers × 3 lines) were used in the previous test. If data set with less receiver number than 21 can sufficiently constrain the target structures, it is possible to reduce the number of receivers leading to lower survey cost and time. I investigate the performance of inversion from data set with 7 receivers. The three receiver lines are decreased to one line. The synthetic data were generated from the same mesh design with the previous test. 2% Gaussian noise was added to the data and the error bar was set to 2% of the data. The N=8,822 data number is reduction.

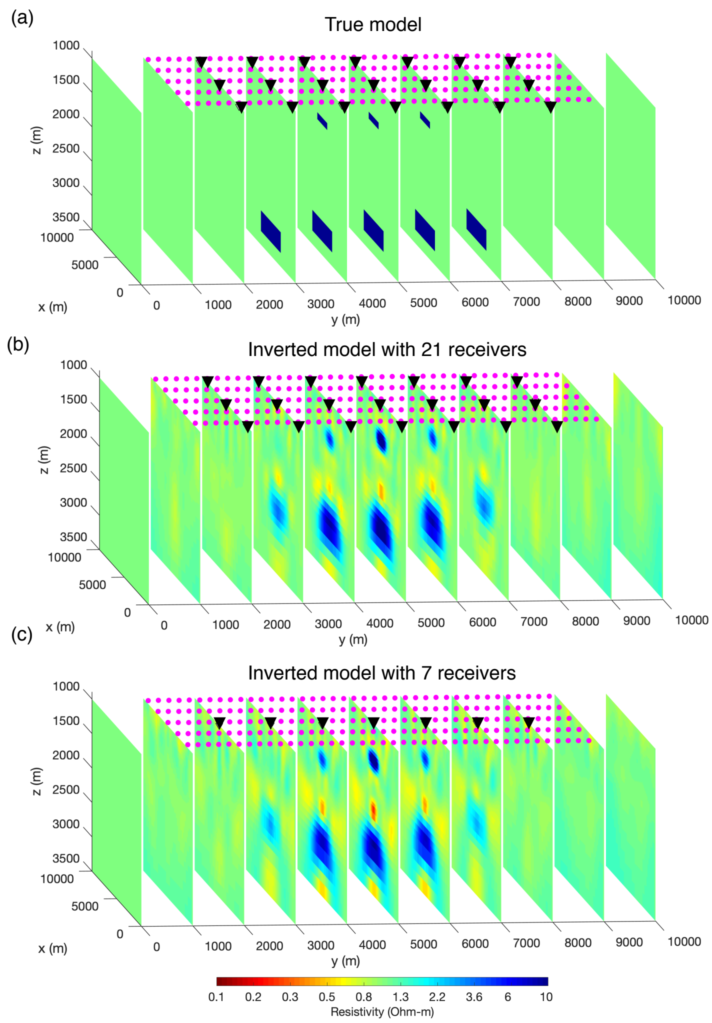

Figure 3.8. (a) Hydrocarbon model used for demonstrating the inversion test. A 20 Ohm-m reservoir and a 50 Ohm-m reservoir are embedded into 1.0 Ohm-m half-space. Black triangles and pink circles indicate receivers and transmitters, respectively. z is depth from the sea surface (z = 0 m). The seafloor is at a depth of 1000 m. (b) Inverted model from the synthetic data with 21 receivers. (c) Inverted model from the synthetic data with 7 receivers.

The initial RMS misfit for the starting model was 13.1. The inversion reached the target misfit at nine iteration numbers (Phase I) and three more iteration numbers was conducted to remove the unnecessary structures (Phase II). Y slices of the inverted model from the synthetic data are displayed in Fig. 3.8c. The inversion algorithm could delineate both shallowly and deeply buried resistors. The recovered model is close to the model with 21 receivers. This result shows the data set with 7 receivers are more optimal for recovering the target structures than 21 receivers. Decreasing receiver number from 21 to 7 can significantly save CSEM surveys cost. A feasibility study is valuable for designing optimal survey array for specific target structures.

3.5.4 Influence of small values to Cm^{-1} on inversion results

I investigated ε influences on inversion results by inputting different values from 10^{-15} to 10^{1} for inverting $\mathbf{C}_m^{-1}$ using the same data set with Fig. 3.6a. The cross-section of the inverted model at y=550 m and y=700 m are shown in Fig. 3.9. Inversion performances are evaluated using L_2 norm of model difference vector defined as below

$$\Delta = \|\mathbf{m}^* - \mathbf{m}\|_2 \quad \textbf{(3-16)}$$

where $\mathbf{m}^*$ is a true model and m is an inverted model through $\log_{10}\sigma$. The RMS misfit, iteration number of phases I and II, and the model difference vector Δ of each inversion results are summarized in Table 3.2.

The inversion algorithm with 10^{-2} to 10^{-12} obtained a very similar model with the target misfit. This result demonstrates that the wide range of ε is useful for inverting $\mathbf{C}_m^{-1}$ without affecting inversion results. With very small ε less than 10^{-13}, the inversion algorithm is unable to recover a model with the target misfit. This result is attributable to the fact that ε was unable to regularize the inverse problem properly. Larger ε makes $\mathbf{C}_m^{-1}$ closer to the diagonal matrix, which imposes similarity to the prior model. The default value is selected as $\varepsilon=10^{-4}$ for the inversion algorithms based on this test. However, widely various ε from 10^{-2} to 10^{-12} are acceptable. The computation time for inverting the matrix $\mathbf{C}_m^{-1}$ and multiplying to $\mathbf{J}_k^T$ took just 150 s with M=142,175 and N=11,376 using PARDISO with 20 OpenMP threads.

Table 3.2. Influence of ε on inversion performance. The RMS misfit, iteration number of phases I and II, and the model difference vector Δ of each inversion results are summarized.

ε	10^{-15}	10^{-11}	10^{-4}	10^{-1}	10^{0}	10^{1}
RMS misfit	1.3	1.0	1.0	1.0	1.0	1.0
Δ	52.0	43.1	43.1	42.0	47.6	51.3
Iteration number (Phase I)	10	4	4	4	6	7
Iteration number (Phase II)		5	5	5	8	8

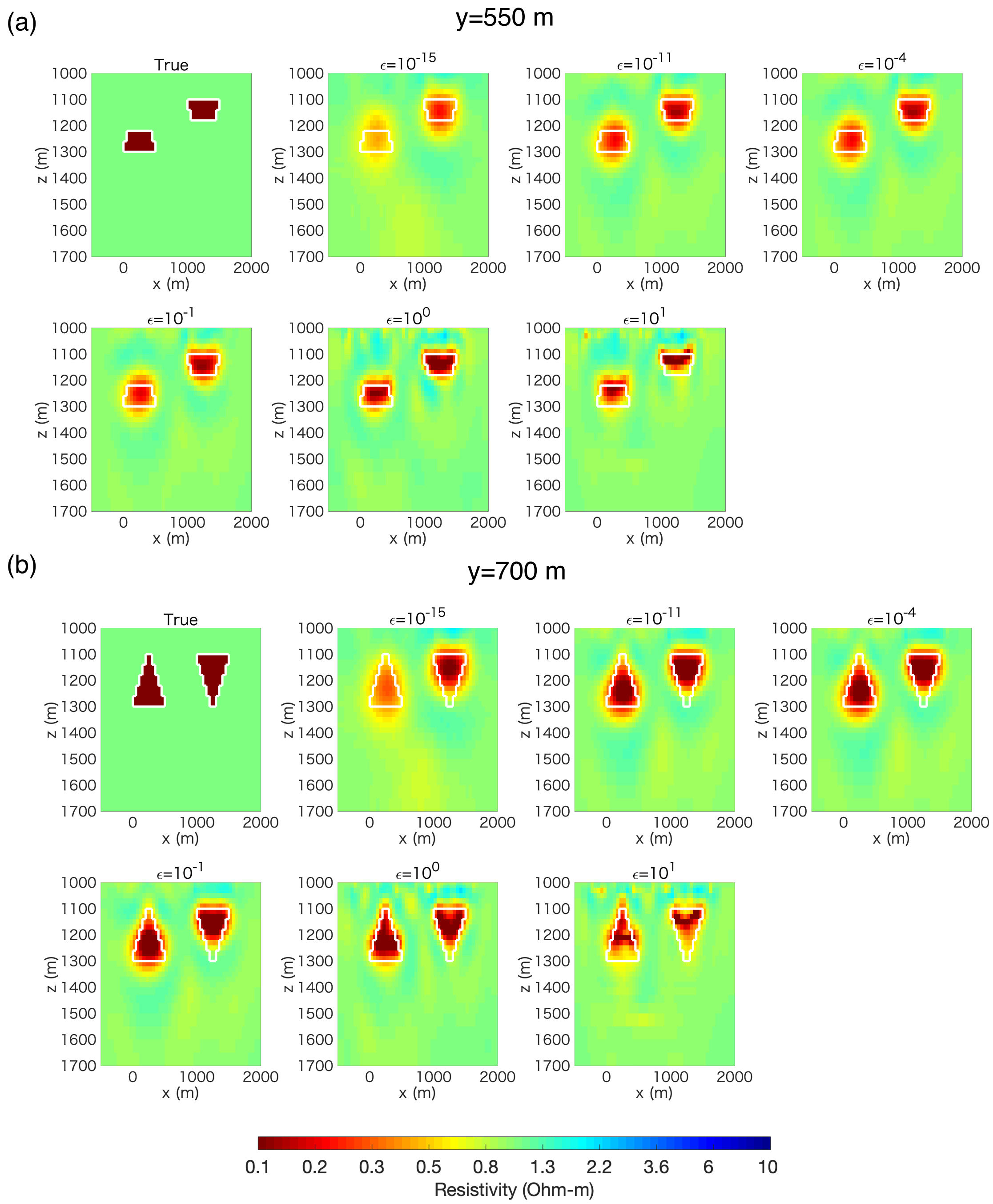

Figure 3.9. Influence of small values ε to $\mathbf{C_m}^{-1}$ on inversion results. Slices of the model at: (a) y = 550 m, (b) y = 750 m. Solid white lines indicate the boundaries of the pyramid and its reverse pyramid.

3.5.5 Influence of noise level on inversion results

I investigated the influences of noise revel on inversion results using the same data set with Fig. 3.6a. The synthetic data were contaminated with Gaussian noise of different revel from 3% to 20%. The cross-sections of the inverted model in the y-direction are shown in Fig. 3.10. The RMS misfit, iteration number of phases I and II, and the model difference vector Δ of each inversion results are summarized in Table 3.3. The inverted model from synthetic data contaminated with 3% Gaussian noise is closest to the true model. Performance of the inverted model from synthetic data contaminated with 5% Gaussian noise is similar to one with synthetic data contaminated with 3% Gaussian noise. The inverted structures of the right reverse pyramid are well resolved with 10% Gaussian noise. However, the resistivity value of the inverted structures of the left pyramid is 0.3 Ohm-m, which is higher than the true value. The inverted structures of the right reverse pyramid are very smooth with 20% Gaussian noise. The left pyramid was poorly imaged. To image the pyramid structures sufficiently, the noise revel must be smaller than 10%.

Table 3.3. Influence of noise level on inversion results. The RMS misfit, iteration number of phases I and II, and the model difference vector Δ of each inversion results are summarized.

Noise revel (%)	3	5	10	20
RMS misfit	1.0	1.0	1.0	1.0
⊿	43.1	44.9	50.0	58.7
Iteration number (Phase I)	4	4	2	1
Iteration number (Phase II)	5	5	4	2

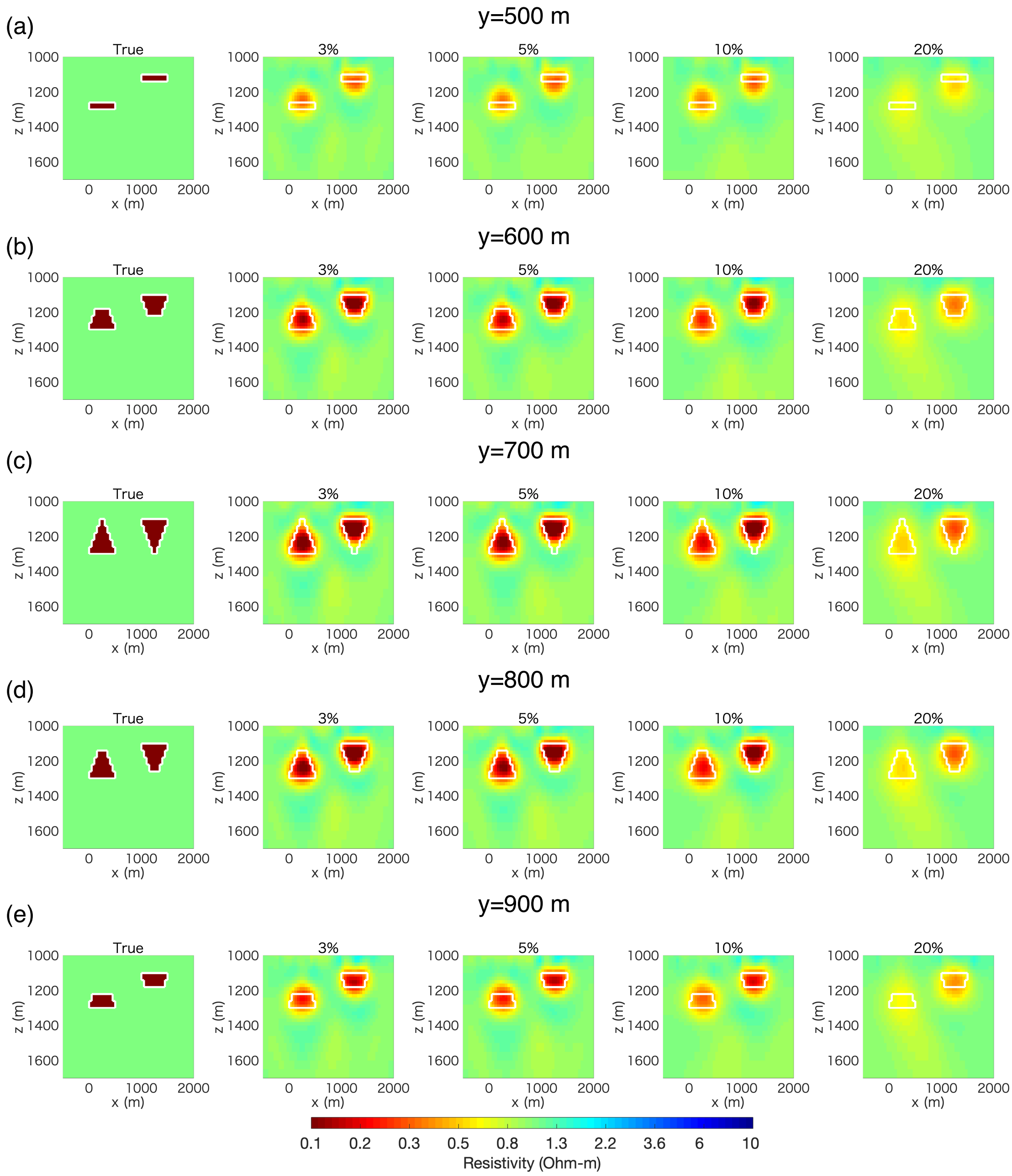

Figure 3.10. Influences of noise revel on inversion results. Slices of the model at: (a) y = 550 m, (b) y = 600 m, (c) y = 700 m, (d) y = 800 m, and (e) Y=900 m. Solid white lines indicate boundaries of the pyramid and its reverse pyramid.

3.5.6 Model covariance based on Gaussian correlation function

In the data-space approach, model covariance is required for computation instead of its inverse in model-space counterpart. There are two ways to make the model covariance. In a way, model covariance is directly defined assuming some correlation function such as Gaussian function (Siripunvaraporn *et al.* 2005). In the other way, one defines inverse of model covariance, which is often made using the first or second derivative of smoothing, then gets the covariance by inverting the matrix adding a small positive value to its diagonal before inverting (Kordy *et al.* 2016, Usui *et al.* 2017, Minami *et al.* 2018). If the first way is applied, I can use the model covariance (called as geostatistical regularization) to include prior correlation information .

To improve the inversion towards finding a geologically consistent model, geostatistical regularization including prior correlation information has been applied to inversion of gravity data (Chasseriau & Chouteau 2003), MT data (Siripunvaraporn & Egbert 2000, Siripunvaraporn *et al.* 2005), airborne time-domain electromagnetic data (Christensen *et al.* 2009), static ERT data (Linde *et al.* 2006, Hermans *et al.* 2012, Jordi *et al.* 2018), and time-lapse ERT data (Hermans *et al.* 2016). Jordi *et al.* (2018) applied geostatistical regularization to ERT inversion with unstructured meshes and showed it is less dependent on mesh sizes compared to standard smoothness constraint made using the first derivative of smoothing.

For the geostatistical regularization of inversion algorithms of geophysical methods, Gaussian function (Chasseriau & Chouteau 2003, Siripunvaraporn *et al.* 2005), exponential function (Linde *et al.* 2006, Jordi *et al.* 2018), spherical functions (Hermans *et al.* 2016) and von Karman function (Maurer *et al.* 1998, Christensen *et al.* 2009) have been used. Exponential and spherical correlation functions are suitable for modeling with heterogeneous structures. On the other hand, the Gaussian correlation function can work for smoothing. The detailed features of correlation functions are summarized in (Chiles & Delfiner 2009). For the smoothing effects, I apply the Gaussian correlation function to the geostatistical regularization where three anisotropic main correlation length (*x*-, *y*-, and *z*- directions) can be used. The Gaussian correlation function can be calculated as follows

$$\mathrm{G}_{3D}(x,y,z) = \frac{1}{\sqrt{2\pi s_x^2}} \frac{1}{\sqrt{2\pi s_y^2}} \frac{1}{\sqrt{2\pi s_z^2}} \exp\left(-\frac{{D_{x,ij}}^2}{2L_x^2} - \frac{{D_{y,ij}}^2}{2L_y^2} - \frac{{D_{z,ij}}^2}{2L_z^2}\right) \tag{3-17}$$

Following the geostatistical analysis, the matrix $\mathbf{D}_x$, $\mathbf{D}_y$, and $\mathbf{D}_x$ contain the lag distances. For example, $\mathbf{D}_{x,ij} = |x_i - x_j|$ is the distance of the *i*th cell center to *j*th the center. s_x^2, s_y^2, s_z^2 are the variance, L_x, L_y, L_z are the correlation length in the *x*, *y*, *z* directions.

In the Occam inversion algorithm, the parameter searching of λ automatically adjusts the amplitude of the variances, thus I set s_x, s_y, s_z as 1 S/m. If L is too big, inversion does not recover small structures. On the other hand, using small L, $\mathbf{C}_m$ becomes a diagonal matrix, which means the model parameters are assumed to be completely uncorrelated (Maurer *et al.* 1998). In the cases prior information such as borehole and geological data are available, the correlation length can be calculated from prior information using geostatistical approach (Linde *et al.* 2006, Hermans *et al.* 2012).

The 3D Gaussian correlation function can be split into a pair of the 1D functions as

$$\mathrm{G}_{3D}(x,y,z)=\frac{1}{\sqrt{2\pi s_x^2}}\exp\left(-\frac{{D_{x,ij}}^2}{2L_x^2}\right)\frac{1}{\sqrt{2\pi s_y^2}}\exp\left(-\frac{{D_{y,ij}}^2}{2L_y^2}\right)\frac{1}{\sqrt{2\pi s_z^2}}\exp\left(-\frac{{D_{z,ij}}^2}{2L_z^2}\right) \quad \textbf{(3-18)}$$

This splitting makes computation efficient. Furthermore, the explicit model covariance is not factorized. Instead, I only factorize the multiplication of the covariance and transpose Jacobian $\mathbf{C}_m\mathbf{J}_k^T$.

In some cases particularly for near-surface applications, covariance parameters can be calculated from semi-variogram analysis of prior information such as borehole logs (Linde *et al.* 2006, Hermans *et al.* 2012). However, for large-scale applications such as CSEM and MT surveys, prior correlation length is frequently not available. In the situation, it is necessary to get a handle on the influences of the correlation length of Gaussian function on the inversion results to choose a reasonable correlation length (Siripunvaraporn & Egbert 2000). I examine influences of the correlation length of geostatistical regularization on the inversion results based on numerical tests using the newly developed inversion algorithm.

A numerical test is conducted for investigating performance of the inversion algorithm with model covariance based on Gaussian correlation function. I use synthetic data and model same with Fig. 3.4. The dimension of both 10 Ohm-m resistive and 0.1 Ohm-m conductive anomalies is Δx=500 × Δy=500 × Δz=200 m. For comparing inversion performances using the different correlation length of $L_{x,y,z1}=(\Delta x, \Delta y, \Delta z)\times 0.02$; $L_{x,y,z2}=(\Delta x, \Delta y, \Delta z)\times 0.05$; $L_{x,y,z3}=(\Delta x, \Delta y, \Delta z)\times 0.125$; $L_{x,y,z4}=(\Delta x, \Delta y, \Delta z)\times 0.25$; $L_{x,y,z5}=(\Delta x, \Delta y, \Delta z)\times 0.375$; $L_{x,y,z6}=(\Delta x, \Delta y, \Delta z)\times 0.5$; $L_{x,y,z7}=(\Delta x, \Delta y, \Delta z)\times 0.75$. The model difference vector Δ between the inverted model and true model is shown in Fig. 3.11a. The inverted models are shown in Fig. 3.12 and Fig. 3.13. Inversion with the correlation length with L_3, L_4, and L_5 imaged both resistive and conductive boxes at a similar performance with traditional smoothing regularization. Inversion with the correlation length with L_4 performed somewhat smaller the model difference vector Δ than with traditional smoothing regularization. Inversion with the correlation length from L_1 and L_2 imaged both anomalies with oscillations due to the small correlation between each model parameter. Even inversion with small correlation length performed well for the resistive anomalies, but the conductive anomalies are recovered with small oscillations. Inversion with L_6 and L_7 produced artifacts in addition to target structures and resulted in large model error without reaching target RMS misfit.

To identify the best correlation length set, the correlation length L_z along the vertical direction was changed from 2 to 200 m. The L_x and L_y is set to be 125 m based on result in the previous test. The model difference vector Δ between the inverted model and true model is shown in Fig. 3.11b. The inverted models with different vertical correlation length are shown in Fig. 3.14 and Fig. 3.15. Inversion with the correlation length with L_z=50 m to L_z=125 m imaged both resistive and conductive boxes at a better performance than the traditional smoothing regularization. Inversion with the small correlation length L_z=2 m imaged both anomalies without oscillations. This means that the horizontal correlation length with L_x=125 m and L_y=125 m working as smoothing constraint. The target structures extend vertically with larger vertical correlation length. This is due to larger smoothing effects on the vertical direction.

Similarly, a test was conducted with different correlation length L_x from 10 to 500 m. The L_y and L_z was set to be 125 and 75 m based on result in the previous tests. The model difference vector Δ between the inverted model and true model is shown in Fig. 3.11c. The inverted models with different x correlation length are shown in Fig. 3.16 and Fig. 3.17. Inversion with the correlation length with L_x=10 m to L_x=200 m imaged both resistive and conductive boxes at a better performance than the traditional smoothing regularization. Inversion with the small correlation length L_x=2 m imaged both anomalies with a small oscillations. The target structures extend horizontally in x direction with larger vertical correlation length. The same test conducted with different correlation length L_y from 10 to 500 m. The model difference vector Δ between the inverted model and true model is shown in Fig. 3.11d.

The test showed that inversion algorithm with reasonable correlation length could outperform the inversion algorithm with the traditional smoothing constraint. Thus, if the correlation length of the target resistivity model is known from the other information such as borehole data, the constraint with the correlation length can improve the inversion performance. And wide range of the correlation length had comparable performance with the traditional constraint. This is helpful for the prior correlation length has some uncertainty.

It is also useful to run inversion with a set of different correlation lengths to find where data can constrain or not. If data sufficiently constrain structures, the structures can be obtained by all inversion with different correlation lengths. In the numerical tests, some artefacts were only imaged by the inversion results with very large correlation length. However, they were not obtained by inversion with the other correlation length. If inversion with only bigger correlation length imaged structures, which are not required in inversion with the other small correlation length, the structures might be artefacts. This is a supplement way to distinguish the artefacts in addition to sensitivity tests. If the sufficient prior information such as geologic and borehole data are available, correlation length of model covariance can be estimated from the information. It can improve the inversion towards finding a geologically consistent model.

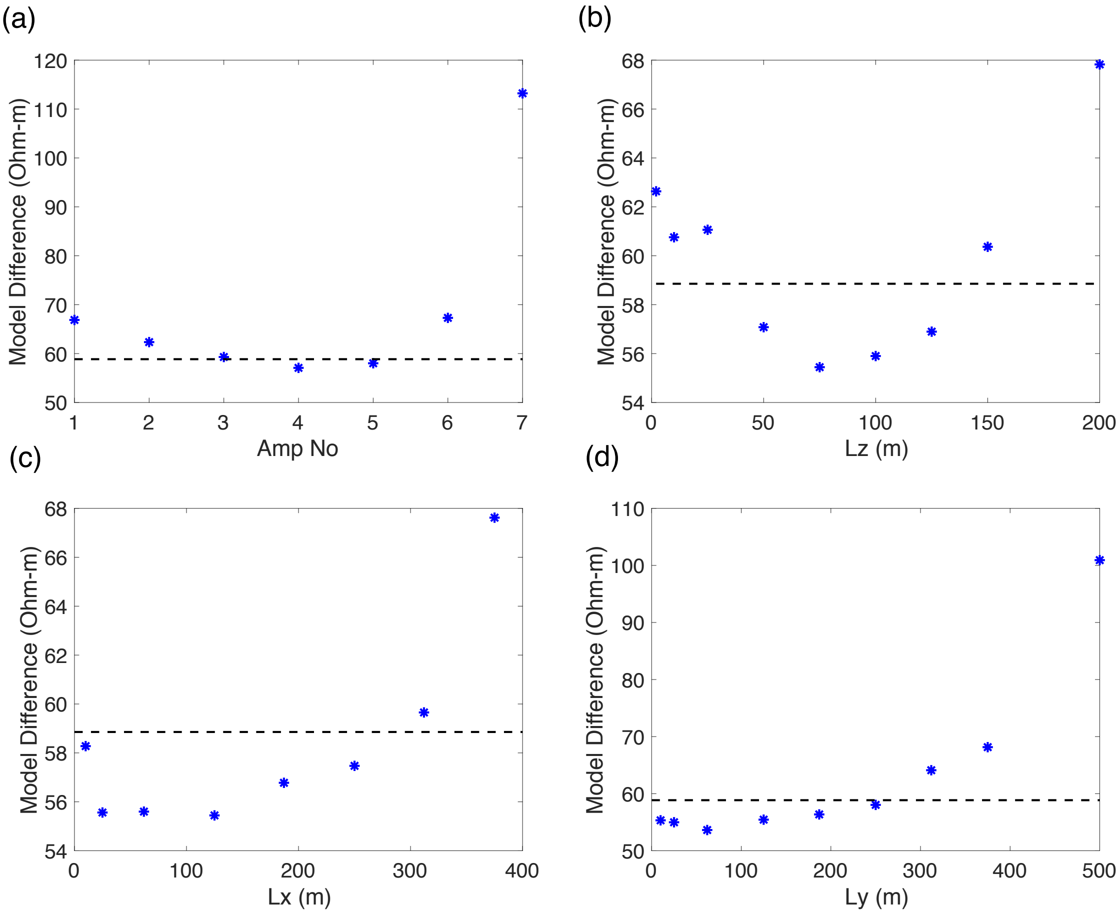

Figure 3.11. Model difference Δ for different correlation length from L1 to L7. The dashed line indicates Δ for inversion results using traditional smoothing constraint. (a) Amplitude of L1 to L7, (b) z-direction from $L_z = 2$ to Lz = 200 m, (c) L_x, and (d) L_y.

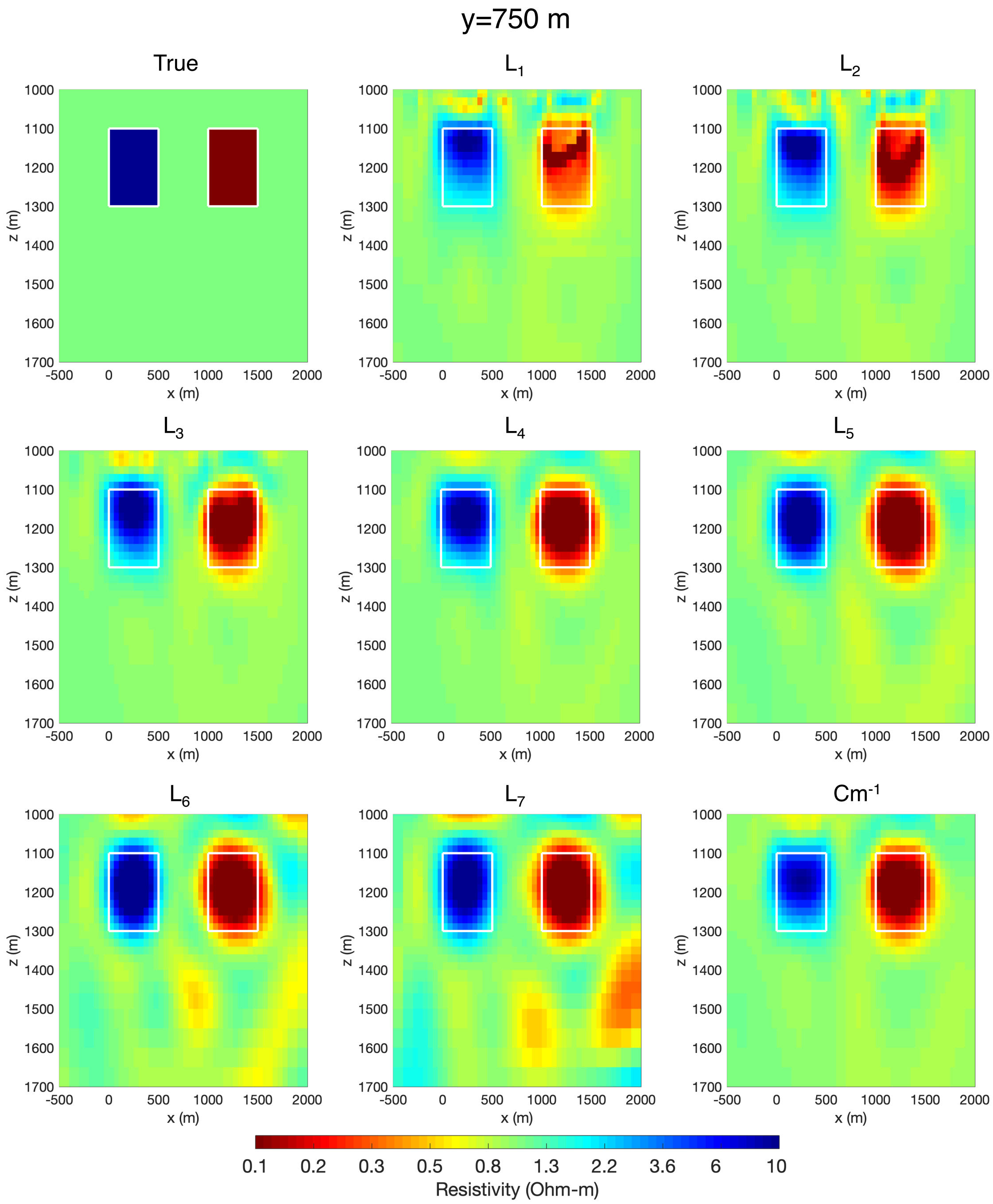

Figure 3.12. Cross sections at y = 750 m of the inverted models with the different correlation length and true model. The inverted model using the traditional smoothing constraint is also shown in the panel. Solid white lines indicate boundaries of the resistive and conductive box.

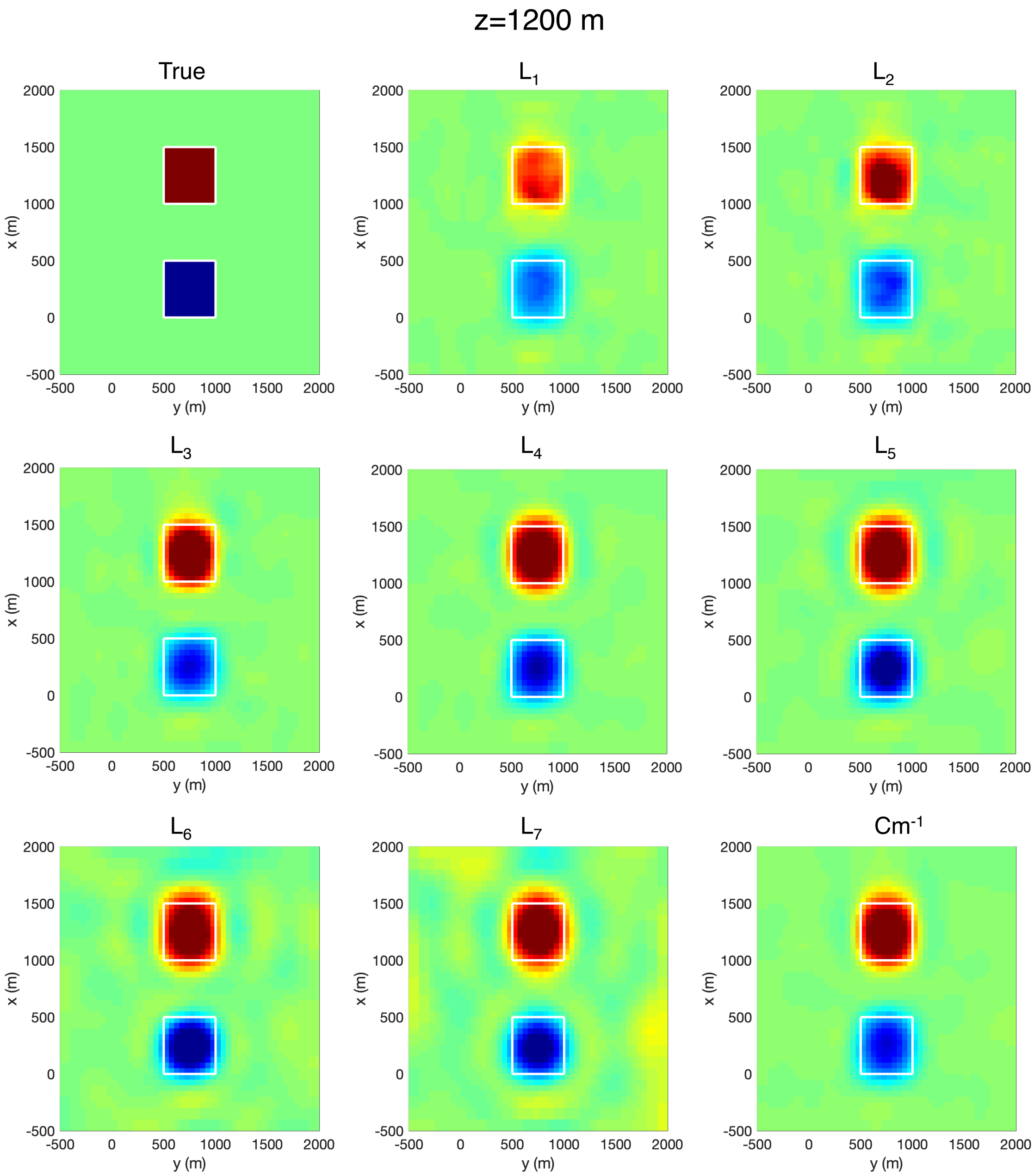

Figure 3.13. Cross sections at z = 1,200 m of the inverted models with the different correlation length and true model. The inverted model using the traditional smoothing constraint is also shown in the panel. Solid white lines indicate boundaries of the resistive and conductive box.

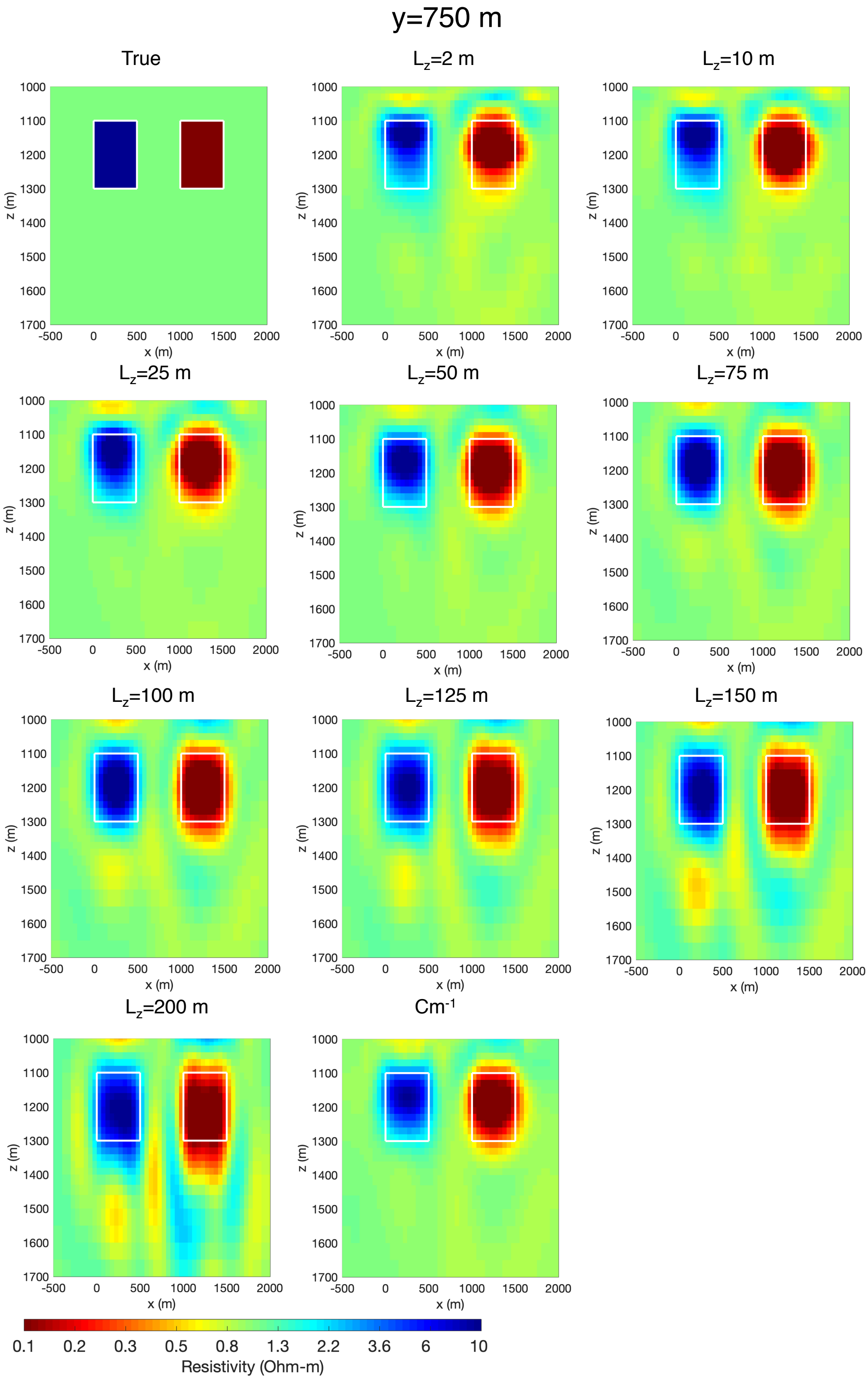

Figure 3.14. Cross sections at y = 750 m of the inverted models with different correlation length in z-direction from L_z = 2 to Lz = 200 m. The inverted model using the traditional smoothing constraint is also shown in the panel. Solid white lines indicate boundaries of the resistive and conductive box.

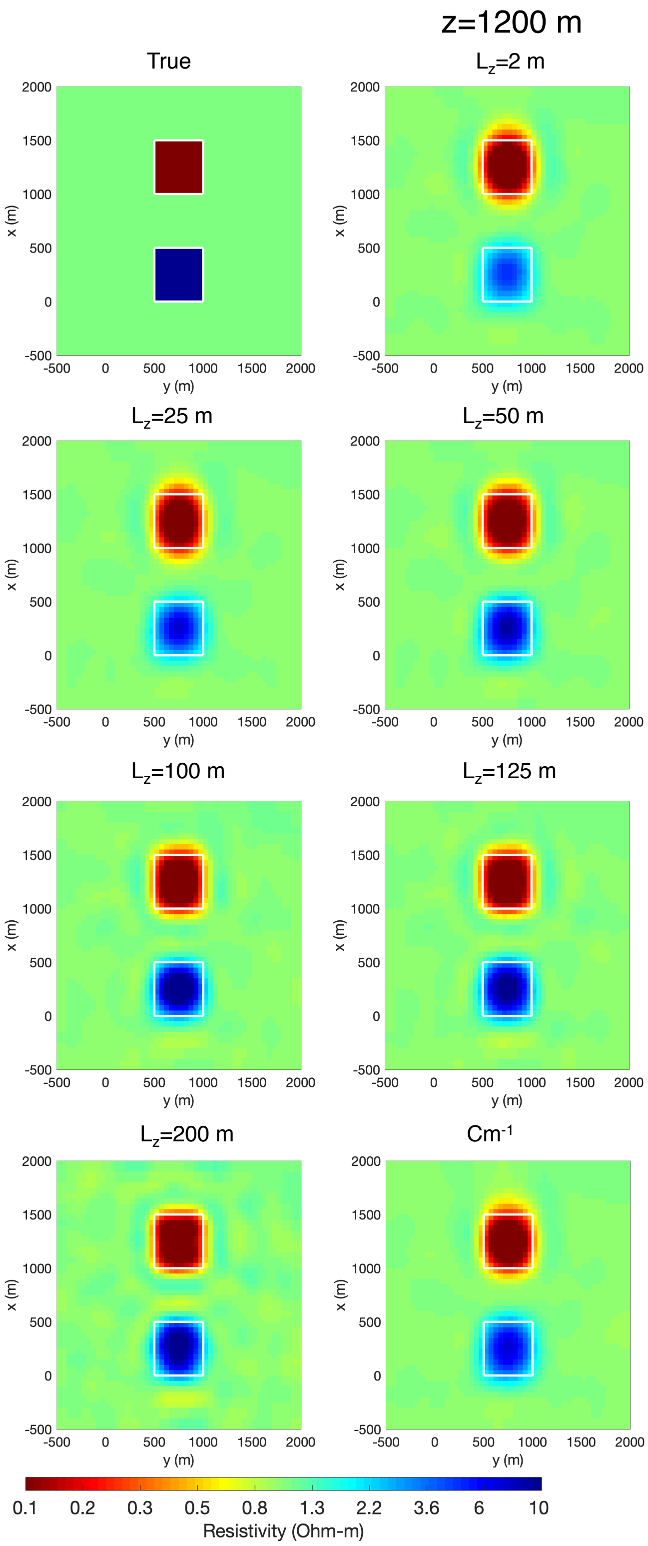

Figure 3.15. Cross sections at z = 1,200 m of the inverted models with different correlation length in z-direction from L_z = 2 to Lz = 200 m. The inverted model using the traditional smoothing constraint is also shown in the panel. Solid white lines indicate boundaries of the resistive and conductive box.

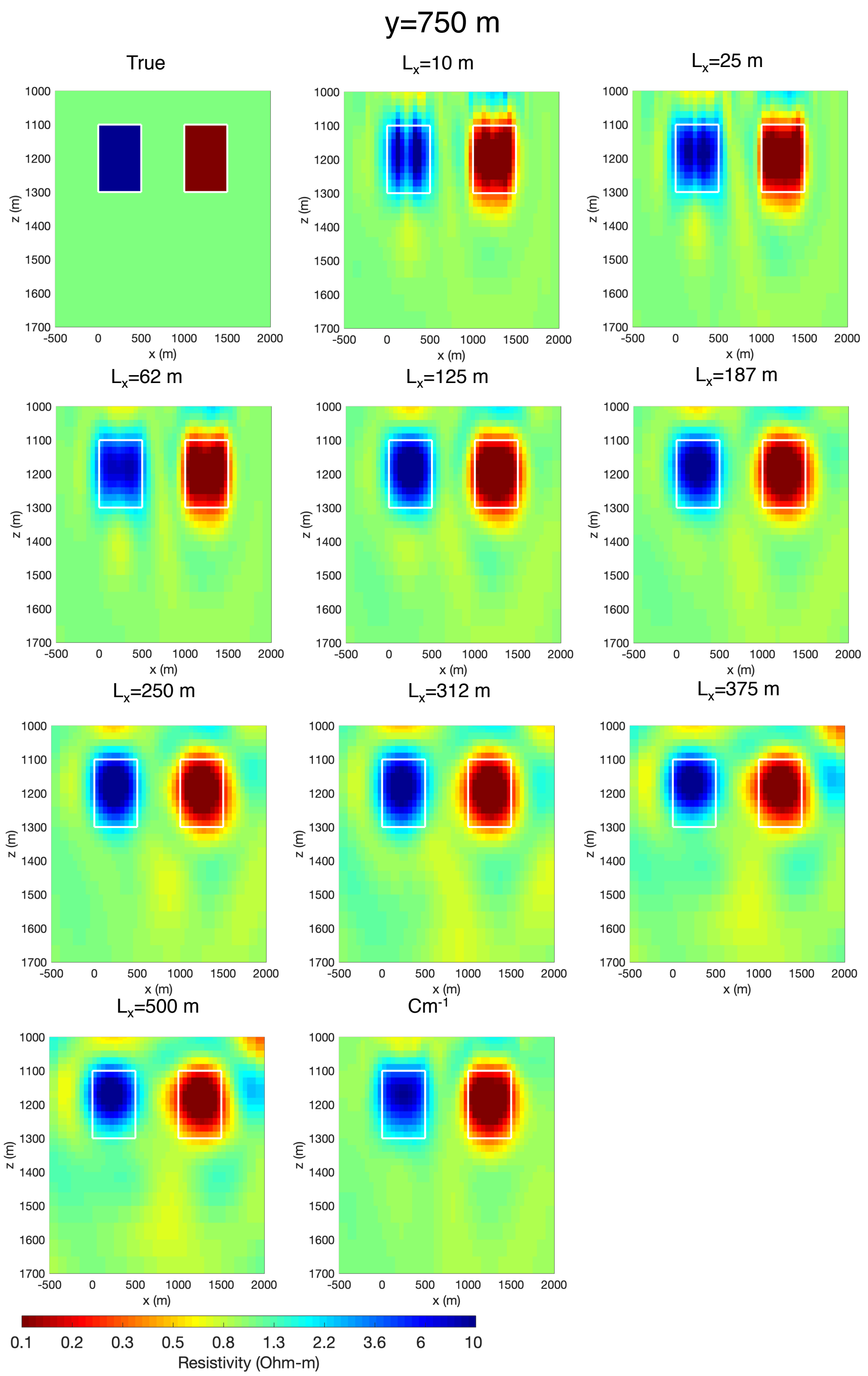

Figure 3.16. Cross sections at y = 750 m of the inverted models with different correlation length in x-direction from L_x = 10 to L_x = 500 m. The inverted model using the traditional smoothing constraint is also shown in the panel. Solid white lines indicate boundaries of the resistive and conductive box.

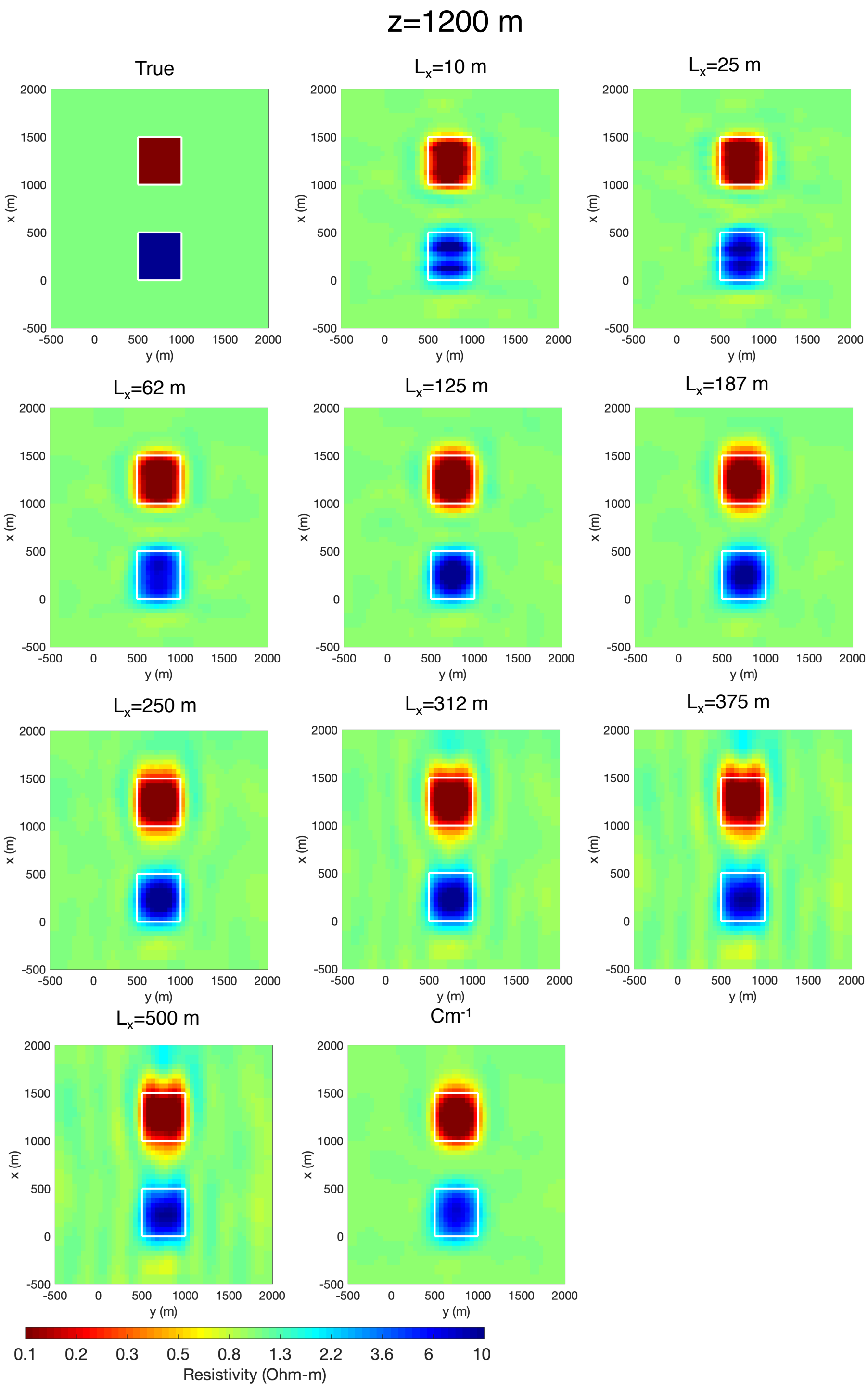

Figure 3.17. Cross sections at z = 1,200 m of the inverted models with different correlation length in x-direction from L_x = 10 to L_x = 500 m. The inverted model using the traditional smoothing constraint is also shown in the panel. Solid white lines indicate boundaries of the resistive and conductive box.

3.6 Synthetic data examples for CSEM inversion of towed and ocean-bottom receiver data

I develop an combined CSEM inversion algorithm of towed and ocean-bottom electric field receiver data to investigate shallow and deep resistivity structures in hydrothermal fields.

3.6.1 Towed CSEM data

Fig. 3.18a shows a model of a homogeneous half-space of 1 Ohm-m containing anomalous objects for generating synthetic data. The seafloor is at a depth of z = 1,000 m below the sea surface (z = 0 m). Four 0.1 Ohm-m conductive and a 10 ohm-m anomalies with 30 m thickness are on the seafloor. The resistive and conductive anomalies respectively simulate gas-bearing rocks and SMS deposits. A buried 0.1 Ohm-m conductive box with 300 × 400 × 50 m dimensions lies at a depth of z = 1,060 m. This conductor represent a buried SMS deposit. An air layer of resistivity 10^8 Ohm-m is present at the top of the model. Seawater resistivity is 0.3 Ohm-m. Sediments below the seafloor are homogeneous, with resistivity of 1 Ohm-m.

I consider a CSEM survey array consisting of towed transmitters and receivers. Three towed receivers at 50, 100, and 150 m offset behind the transmitter center record electric field data. Although this system is very similar to ERT survey system in Fig. 1.6, the electric responses are treated as CSEM data for more precision than a direct current assumption. A transmitter using an HED oriented along the y-direction and three inline receivers is towed at a height of 20 m above the seafloor. 5 towing lines run parallel to each other. There are 250 transmitting points with 50 points in each tow line. A spatial spacing of the transmitting points is 30 m. Observed data were generated by forward modeling responses on a grid of 46 × 113 × 59 cells including several boundary cells to minimize boundary effects. For the horizontal cells, a 20 m grid was used in the interest region. I appended several boundary cells at each side, growing in size at a stretching factor of 2.0. For the vertical grid, fine grids of 5 m spacing were used in the region of z = 1,000–1,070 m. The vertical grid size increases gradually with increasing distance from the transmitters.

The inversion domain is limited to the interesting seafloor region, excluding boundary cells and air, and resulting in M=97,440 unknown model parameters. The starting and prior model for the example is a homogeneous half-space with resistivity of 1 Ohm-m. The inputted data use a combination $\log_{10}$ scaled amplitude and linear scaled phase of E_y. The component at frequencies of 0.125 and 1.0 Hz results in a N=3,000 data number. 3% Gaussian noise was added to the data. The error bar was set to 3% of the data. The target RMS misfit is 1.0, which indicates that the averaged misfit is within the assumed error.

The initial RMS misfit for the starting model was 3.0. The inversion reached the target misfit at two iteration numbers (Phase I). Then a more iteration was conducted to remove the unnecessary structures (Phase II). Vertical slices of the inverted model from the synthetic data are displayed in Fig.

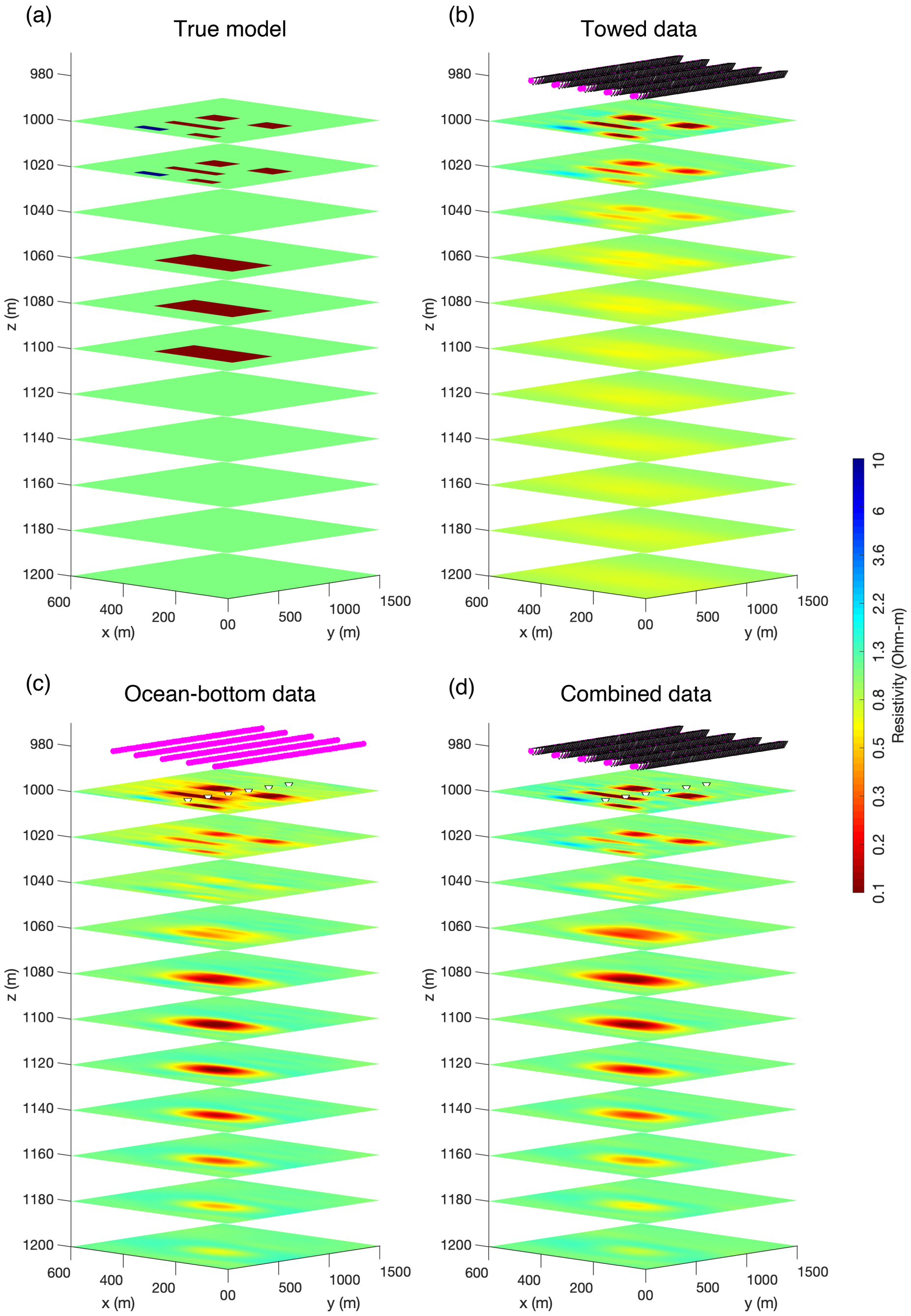

Figure 3.18. (a) Vertical slices of the model used for demonstrating the inversion test. *z* shows depth from the sea surface. Circles and triangles respectively show the transmitter and receiver positions. (b) Inverted resistivity model from towed receiver data. (c) Inverted resistivity model from ocean-bottom receiver data. (d) Inverted resistivity model from combined towed and ocean-bottom receiver data. Four 0.1 Ohm-m conductive and a 10 ohm-m anomalies with 30 m thickness are on the seafloor. A buried 0.1 Ohm-m conductive box with 300 × 400 × 50 m dimensions is embedded with its top at a depth of *z* = 1,050 m.

3.18b. Results show that the inversion algorithm sufficiently recovered positions and resistivity values of both conductive and resistive anomalies on the seafloor. However, a buried conductor was not resolved. The result implies that towed CSEM data have high sensitivity and resolution for resolving the shallow anomalies. The penetration depth was constrained by the offset between the transmitters and receivers. The 150 m maximum offset in this array results in a poor sensitivity to the buried conductor. In the next section, I consider inversion of the ocean-bottom receiver data to investigate its ability of resolving buried structures.

3.6.2 Ocean-bottom CSEM data

I consider CSEM survey data consisting of towed transmitters and deployed ocean-bottom receivers. 6 receivers are deployed on the seafloor to record the electric fields. Then, 250 transmitters using an HED oriented along the *y*-direction are towed at a height of 20 m above the seafloor. Observed data were generated by forward modeling responses on the same grid with previous section from the synthetic model shown in Fig 3.18a. The $\log_{10}$ scaled amplitude and linear scaled phase of E_y for source–receiver distances larger than 300 m at frequencies of 0.125 and 1.0 Hz results in a N=5,128 data number. 3% Gaussian noise was added to the data. The error bar was set to 3% of the data. The target RMS misfit is 1.0. The starting and prior model for the example is a homogeneous half-space with resistivity of 1 Ohm-m. Unknown model parameters M is 97,440.

The initial RMS misfit for the starting model was 7.9. The inversion reached the target misfit at five iteration numbers (Phase I). Then three more iteration was conducted to remove the unnecessary structures (Phase II). Vertical slices of the inverted model from the synthetic data are displayed in Fig. 3.18c. Results show that the inversion algorithm of ocean-bottom receiver data recovered conductors on the seafloor with artefacts. A resistor on the seafloor was not recovered. A imaged buried conductor are clearly distinguishable from the homogeneous half-space. This result implies that longer offset data increase sensitivity to buried structures, but low spatial converge of data cannot resolve the small heterogenous on the seafloor. In the next section, I consider the CSEM inversion of towed and ocean-bottom receiver data to recover resistivity images covering the shallow and deep structures.

3.6.3 Towed and ocean-bottom CSEM data

I consider a CSEM inversion of combined towed and ocean-bottom receiver data. Observed data were generated by forward modeling responses on the same grid with previous section from the synthetic model shown in Fig 3.18a. The observed data consist of towed receivers data (N=3,000) and the ocean-bottom receiver data (N=5,128) resulting in N=8,128 data number. 3% Gaussian noise was added to the data. The error bar was set to 3% of the data. The target RMS misfit is 1.0. Unknown model parameters M is 97,440.

The initial RMS misfit for the starting model was 6.5. The inversion reached the target misfit at four iteration numbers (Phase I). Then two more iteration was conducted to remove the unnecessary structures (Phase II). Vertical slices of the inverted model from the synthetic data are displayed in Fig. 3.18d. The inversion resolved the conductors and resistor on the seafloor. A imaged buried conductor are clearly distinguishable from the homogeneous half-space. The result implies that the CSEM inversion of combined towed and ocean-bottom receiver data can recover shallow and deep resistivity structures.

3.6.4 Comparison of inversion results

The inversion performance of these CSEM data described in previous sections are compared. Fig. 3-19 shows 2D cross-sections of inverted resistivity models to see small differences. The inversions of the towed receivers data and combined data sufficiently recovered positions and resistivity values of both conductive and resistive anomalies on the seafloor. The inversion of the ocean-bottom receiver data produced artefacts on the seafloor. This result shows that the towed CSEM data has great sensitivity to the shallow anomalies on the seafloor. Using high spatial converge data from the towed receivers improves inversion ability of resolving shallow resistivity structures.

The inversion of the ocean-bottom receiver data and combined data recovered the buried conductor. The inversion of towed CSEM data was not able to image the buried conductor. The ocean-bottom receiver data including long transmitter–receiver offset help the inversion recover the buried structures. The inversion of combined data could recover anomalies on the seafloor and also a buried anomaly. A noteworthy fact is that inversion of combined data resolved the top of buried conductor better than inversion of only ocean-bottom receiver data. This result implies that artefact on the seafloor might have influences on the buried structures.

To investigate influences of seafloor local anomalies on the buried conductor, I remove the anomalies on the seafloor. The synthetic data was generated from a model without seafloor anomalies shown in Fig. 3.20a. The same data array with test of Fig. 3.18c was used in this test, resulting in a N=5,128 data number. 3% Gaussian noise was added to the data. The error bar was set to 3% of the data. The target RMS misfit is 1.0.

The initial RMS misfit for the starting model was 3.4. The inversion reached the target misfit at two iteration numbers (Phase I). Then two more iteration was conducted to remove the unnecessary structures (Phase II). Vertical slices of the inverted model from the synthetic data are displayed in Fig. 3.20b. Results show that the inversion algorithm of ocean-bottom receiver data recovered buried conductor. Fig. 3.21 shows 2D cross-sections of inverted resistivity models to see small differences. The inversion recovered the top of the anomaly with similar performance to the inversion of combined data in Fig. 3.18d. However, the inversion of ocean-bottom receiver data in Fig. 3.18c could not recover the top clearly compared to these two inversion results. This result implies that the small artifacts had influences on the buried structures. By resolving the shallow resistivity structures and removing the unnecessary effects on the buried structures, inversion of combined data also could improve the buried structures.

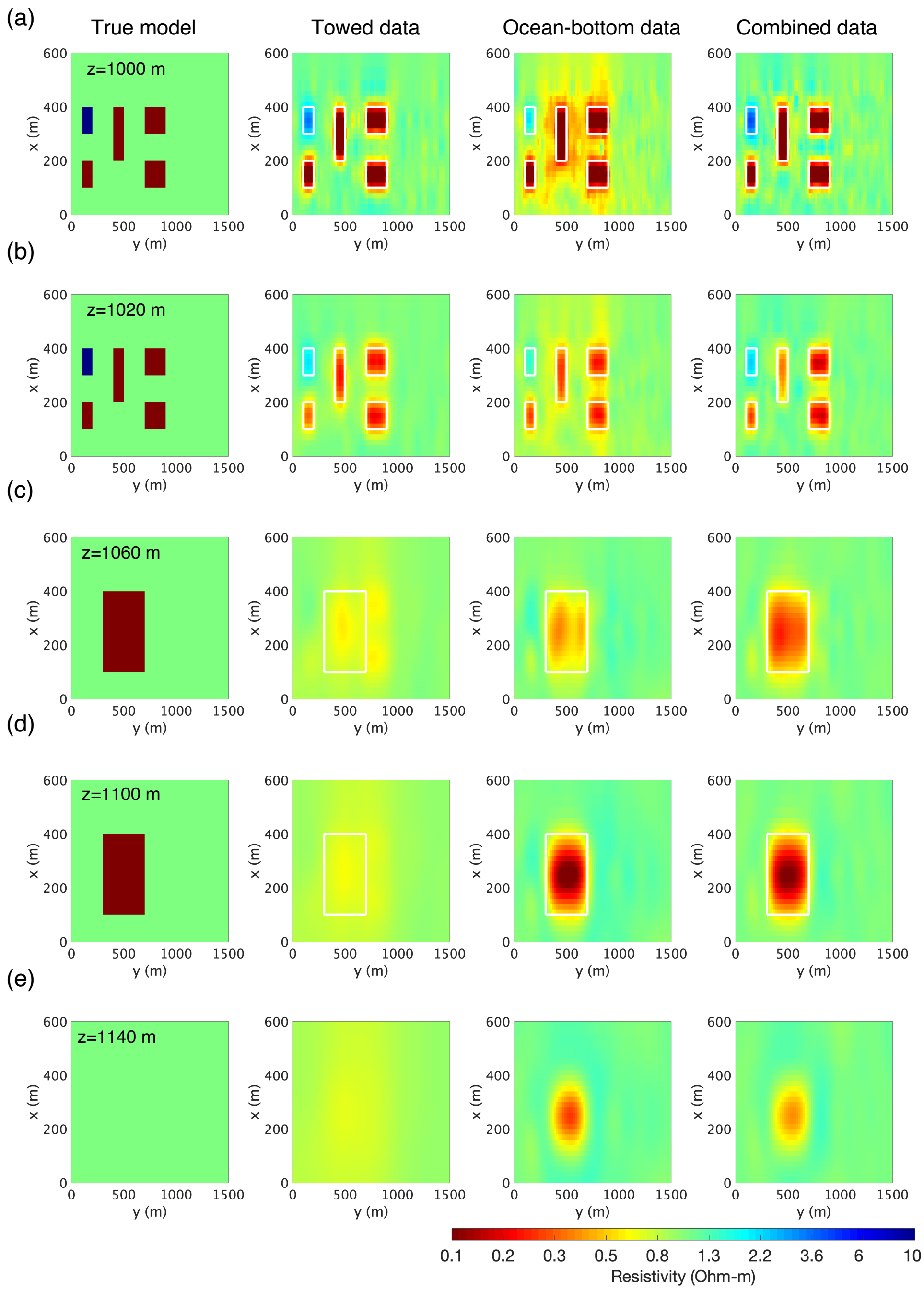

Figure 3.19. Cross-section of the inverted model shown in Fig. 3.18. 2D images of inverted resistivity models at *z* = (a) 1,000 m (seafloor), (b) 1,020 m, (c) 1,060 m, (d) 1,100 m, and (e) 1,140 m. Solid white lines indicate the boundaries of the true anomalies.

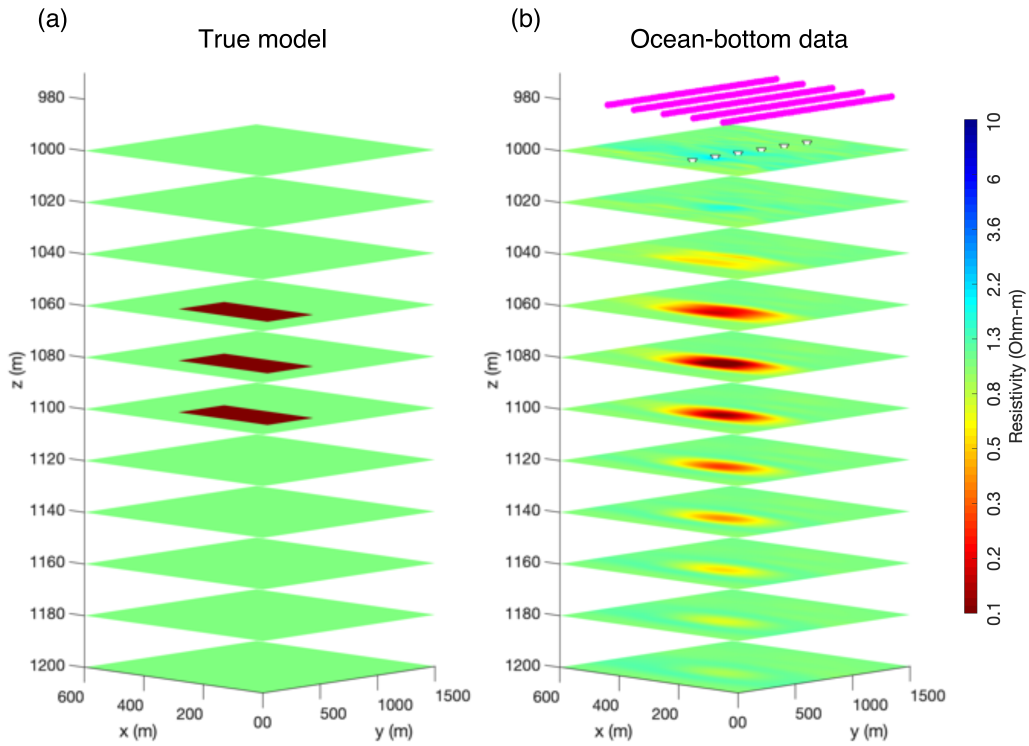

Figure 3.20. (a) Vertical slices of the model used for demonstrating the inversion test. *z* shows depth from the sea surface. Circles and triangles respectively show the transmitter and receiver positions. (b) Inverted resistivity model from ocean-bottom data.

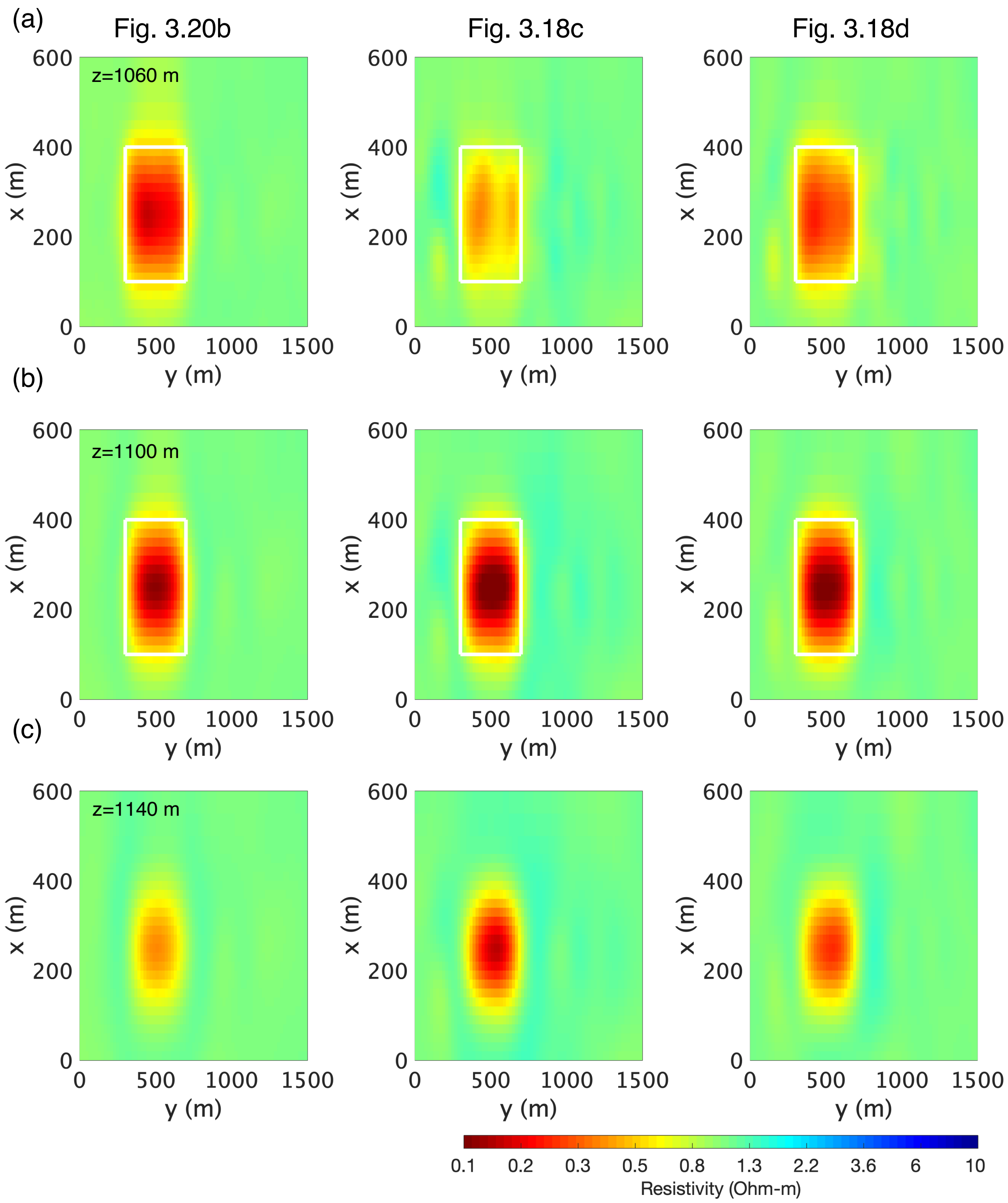

Figure 3.21. Cross-section of the inverted model shown in Fig. 3.20b, 3.18c, and 3.18d. 2D images of inverted resistivity models at z = (a) 1,060 m, (b) 1,100 m, and (c) 1,140 m. Solid white lines indicate the boundaries of the true anomalies.

3.7 Conclusions

I developed an Occam inversion algorithm for the 2D marine ERT survey and an Occam inversion algorithm for the 3D CSEM survey. Both Occam inversion algorithms could obtain the minimum-norm model with target misfits after a few iteration numbers. I applied the model-space approach to the inversion algorithm for the 2D marine ERT survey because the number of model parameters is comparable with the number of data in the inverse problem of the 2D ERT survey. For the 3D CSEM inversion problem, the number of model parameters is frequently much larger than the number of data Dimension of coefficient matrix for updating models could be reduced, from $M \times M$ in the model-space approach, to $N \times N$ in the data-space approach.

The 2D marine ERT inversion algorithm could image the shallowly existing conductive anomalies after a small number of iterations. The results from the numerical tests showed the inversion algorithm of the ERT data with 180 m cable length could image SMS deposits placed up to a depth of 45 m below the seafloor. This survey system can record apparent resistivity data each 5 to 10 m in horizontal distance. The towing line length is over 20 km during 8 hours operation. Thus, high-resolution images near the seafloor by the 2D marine ERT inversion algorithm are useful in mapping SMS distributions. The numerical tests with 360 m cable length showed the inversion algorithm could image SMS deposits placed up to a depth of 75 m below the seafloor. I showed the penetration depth is controlled by the cable length of the towed system based on the numerical tests. The penetration depth increases with increasing length of the cable. However, the attitude of the longer cable easily becomes unstable, causing large navigation errors.

The 3D marine CSEM inversion algorithm could image conductive and resistive anomalies embedded into a half-space after a small number of iterations. The deeply buried resistors were recovered by the inversion algorithm from the data set including longer Tx-Rx offset array. Furthermore, numerical tests revealed inverted models from the synthetic data with 21 receivers and the synthetic data with 7 receivers were similar. This result indicates the data with 7 receivers is sufficient to constrain a specific target structure. Conducting such numerical tests help to determine an optimal survey array, leading to a reduction of survey cost.

I developed an combined CSEM inversion algorithm of towed and ocean-bottom electric field receiver data to investigate shallow and deep resistivity structures in hydrothermal fields. The inversion of combined data could recover anomalies on the seafloor and also a buried anomaly. A noteworthy merit is that inversion of combined data resolved the top of buried conductor by resolving the shallow resistivity structures.

Chapter 4

Application to observed ERT data for shallow resistivity structures

4.1 Introduction

A map of the internal structures of a seafloor hydrothermal system provides a key to elucidating the SMS deposit generation mechanisms. In past studies, seafloor drilling surveys have been conducted for the lithological studies of SMS deposits. One of the best-studied hydrothermal areas is the TAG hydrothermal field in the mid-Atlantic Ocean (Humphris *et al.* 1995, Petersen *et al.* 2000). Other hydrothermal fields such as in the Iheya North Knoll (Expedition 331 Scientists 2010) and Palinuro Seamount (Petersen *et al.* 2014) were also investigated using boreholes. However, the generation mechanisms of SMS remain unclear because of a lack of detailed internal images of SMS deposits. Although seafloor drilling is a powerful tool, its use is limited because it entails high costs. Even if numerous drillings are conducted, geophysical images have been requested to fill gaps among boreholes.

In the TAG mound, pilot EM surveys revealed sub-seafloor low resistive areas, possibly related to SMS deposits (Cairns *et al.* 1996, Von Herzen *et al.* 1996). Haroon *et al.* (2018) and Gehrmann *et al.* (2019) presented 2D inversion results across the TAG mounds using the towed CSEM survey. However, they had low sensitivity to near-seafloor structures because of the limited number of receivers and their survey configuration. Other new surveys have deeper penetration to tens to hundreds of meters (Safipour *et al.* 2017, 2018, Constable *et al.* 2018, Imamura *et al.* 2018, Müller *et al.* 2018). However, the measurements should be done as stationary (with the fixed source, receivers or both) lacking dense spatial samplings. In fact, high-resolution images of resistivity structures below the seafloor in hydrothermal areas (*e.g.* to 50 m depth with spatial resolution of 10 m) have never been reported, even though such imaging is necessary to discuss the evolution mechanisms of SMS deposits attributable to high spatial heterogeneities that have been inferred from drilling studies.

I specifically examine a deep-towed marine ERT system with multiple electrodes to image such detailed electrical resistivity of SMS deposits (Fig. 1.6). It has higher efficiencies of spatial coverage and resolution in the shallow sub-seafloor depth than other marine EM methods. This survey system was developed first for detecting shallowly existing gas hydrate (Goto *et al.* 2008). The ERT system has often been used for near-surface exploration on land (also designated as direct current resistivity survey) with several stationary electrodes, but this marine ERT system tows multiple electrodes for increasing both the horizontal resolution near the seafloor and the total length of the survey profile.

4.2 Iheya North Knoll hydrothermal field

Target area in this study is the Iheya North hydrothermal field, mid-Okinawa Trough, southwestern Japan (Fig. 4.1). The Iheya North hydrothermal field of the Okinawa Trough is about 150 km NNW distant from Okinawa Island. A hydrothermal area discovered on the Iheya North Knoll in 1995 has since been investigated intensively (Nakagawa *et al.* 2005, Takai *et al.* 2006, Kumagai *et al.* 2010, Masaki *et al.* 2011, Kasaya *et al.* 2015, Miyoshi *et al.* 2015). The IODP Expedition 331 was also conducted in the area by the deep-sea drilling vessel (D/V) Chikyu. Core samples of IODP Expedition 331 strongly resemble the black ores in kuroko deposits of the Miocene age in Japan (Expedition 331 Scientists 2010). More recently, additional drilling was implemented at the CK14–04 and CK16–01 cruises (Expeditions 907, 908) by D/V Chikyu. The accumulated survey data indicate this area as suitable for the detailed imaging of SMS deposits.

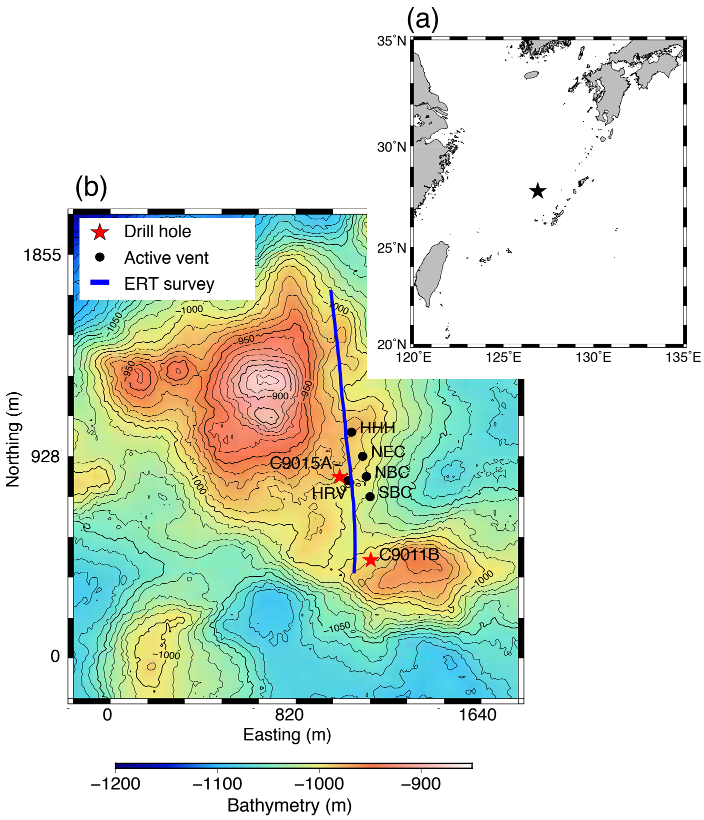

Figure 4.1. Maps of the study area. (a) Location of the Iheya North hydrothermal field, Okinawa Trough, southwestern Japan shown as a black star. (b) Event map of the Iheya North field. Red stars denote the IODP drilling sites (C9015A and C9011B). Black circles denote hydrothermal fluid venting sites (SBC, HRV, NBC, NEC, and HHH). The blue line represents a survey profile with the towed ERT system.

4.3 Observed ERT data

The ERT data were collected during the YK 14–19 cruise survey (R/V Yokosuka, JAMSTEC) at the active hydrothermal region, where hydrothermal fluid venting sites have been observed (Fig. 4.1b). The system was towed from the south to north with altitude of 5–50 m above the seafloor. The electrode pairs of COM1–P3 and P3–P4 (n-levels 4 and 5) were, unfortunately, unavailable because of system troubles. The number of collected data as apparent resistivity was 966. The averaged error values of the observed apparent resistivity are, respectively, 0.14, 0.22, 1.70, 2.04, 2.39, and 3.23% for n-Levels 2, 3, 6, 7, 8, and 9.

The apparent resistivity values from the marine ERT survey are estimated using least-squares method at every 15 s, with segments corresponding horizontally to a sampling rate of 7.5 m. To avoid unwanted effects of the main armored metallic cable and the towed system frame on measurements, I applied calibration factors to the observed data. For calibration, the system was towed at 500 m depth for 7 min, far from the sea surface and seafloor. The obtained apparent resistivity are expected to be equal to the seawater resistivity measured simultaneously with the CTD sensor for the estimation of calibration factors. The seawater resistivity by CTD was 0.280 Ohm-m. The measured apparent resistivity was in the range of 0.251–0.258 Ohm-m for n-Levels of 2–9. Therefore, the calibration factor was calculated as 1.09–1.12 for n-Levels of 2–9. This fact suggests that armored cable between the vessel and the deep-tow system can decrease about 9–12% in the observed apparent resistivity.

The apparent resistivity obtained using the marine ERT system indicates electrically conductive features below the seafloor. The pseudo-section of observed apparent resistivity is presented in Fig. 4.2a. At short separations between current and potential electrodes (with n Level of 2–3), low apparent resistivity values are observed at horizontal locations of 200–700 m (A1 in Fig. 4.2a). The values are about 0.3 Ohm-m, which is lower than the seawater resistivity, implying the existence of the conductive zones below the seafloor. Moreover, at horizontal locations of 350–500 m, the lowest apparent resistivity (A2 in Fig. 4.2a) is discovered under the longer separations (*e.g.* n-Level of 7–9). The observed error of apparent resistivity is about 0.14–0.22% at an n-Level of 2–3, and 2.39–3.23% at an n Level of 8–9, so that the low apparent resistivity values at A1 and A2 are valid. They possibly correspond to extremely conductive zones buried deep below the seafloor.

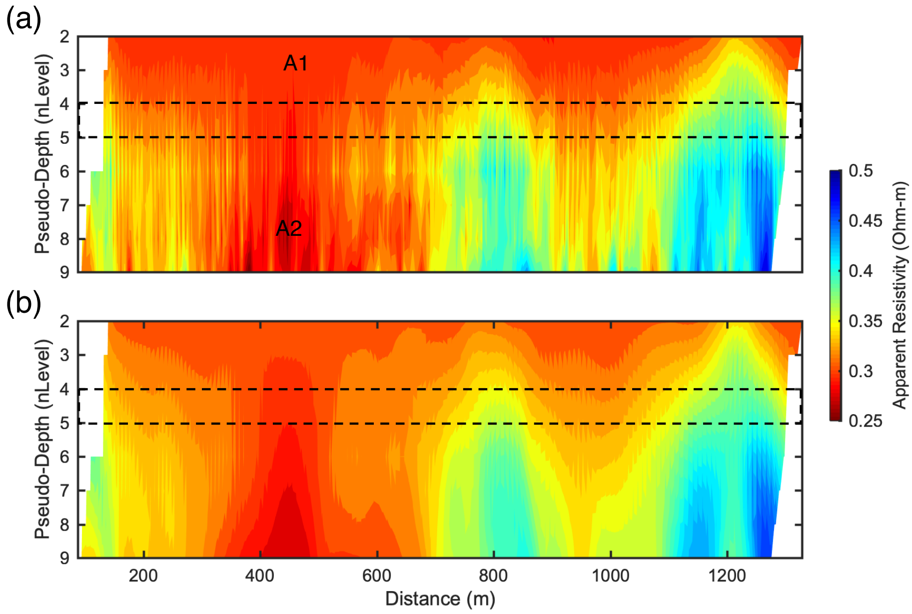

Figure 4.2. (a) Pseudo-section of the observed data. Pseudo-depth shows the n Level of Tx-Rx distance (15 × n). A1 and A2 show the low apparent resistivity areas. (b) Pseudo-section of the response from the inverted model (Fig. 4.3). Missing observed data points at n-levels (4 and 5) enclosed by dashed lines were interpolated from neighboring points.

4.4 Inversion results from the observed 2D ERT data

4.4.1 Inverted model

The initial and prior models for the inversion are 1.0 Ohm-m homogeneous half-space below the seafloor. The grid number for the forward modeling was 16,327; the number of unknown parameters was 6,186 without updating the seawater resistivity. The error floor was set as 2% of the observed apparent resistivity. The average and standard deviation of the sea resistivity measured using CTD during the towing were, respectively, 0.3062 and 0.373 × 10^{-3} Ohm-m. The seawater resistivity was fixed in the modeling as this average.

The inversion result (Fig. 4.3) is consistent with the features inferred from the observed pseudo-section of apparent resistivity. The initial RMS misfit between observed and calculated apparent resistivity values was 6.5. Subsequently, it reached 2.2 after the third iteration through the inversion process. The apparent resistivity pseudo-section calculated from this model (Fig. 2.8b) closely matches with the observed data, especially including good fits to the low apparent resistivity values (A1 and A2 in Fig. 4.2a). Based on synthetic inversion tests with sub-seafloor models having a simple low-resistivity anomaly (Ishizu *et al.* 2019b), the approximate maximum sounding depth of 45 m below the towed cable can be well resolved. In this survey, the area shallower than 1012 m from the sea surface (*i.e.* the averaged towed depth, 967 m, plus 45 m) can be well resolved. Although the area deeper than 1012 m has lower resolution than the shallower part, it still has sensitivity and necessity for explaining the observed ERT data. Based on these sensitivity tests, I chose 0.032 of the normalized sensitivity (maximum value is 1.0; shown in Fig. 4.5) as a threshold of the resolved areas, corresponding to about 1030 m depth below the sea surface.

The inversion result reveals sub-seafloor electric conductive zones of around 0.2 Ohm-m or less. The resistivity section also shows semi-layered structures (Fig. 4.3): the shallow conductive zone (CD1) and the deeply buried one (CD2). The extremely low resistivity value compared to the background one (1.0 Ohm-m) is consistent with resistivity values of SMS deposits measured in the hydrothermally active area (Cairns *et al.* 1996, Von Herzen *et al.* 1996). On the seafloor above CD1 and CD2, several hydrothermal fluid venting sites are observed (Kawagucci *et al.* 2013) together with high heat flow anomalies (Masaki *et al.* 2011). Therefore, CD1 and CD2 might be attributable to conductive SMS deposits or a conductive hydrothermal fluid reservoir below the seafloor.

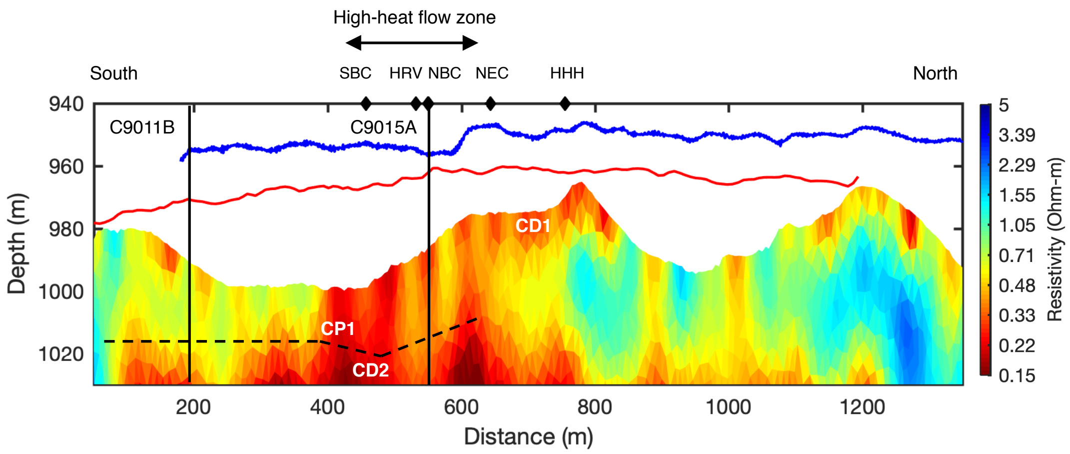

Figure 4.3. Inverted resistivity model from the ERT survey data. Blue and red lines respectively show the head and the tail positions of the deep-towed system. Black lines are locations of seafloor drilling. Black diamonds show the horizontal position of observed hydrothermal vents, presented in Fig. 4.1b. The black dashed line is a strong seismic reflector obtained during cruises KR 10–02 (Tsuji *et al.* 2012). CD1 and CD2 denote conductive zones, which imply SMS deposits. CP1 is a cap rock zone. The black double arrow indicates a high-heat flow zone (Masaki *et al.* 2011).

4.4.2 Comparison with LWD resistivity data

Before conducting sensitivity studies, I compare the inverted resistivity (Fig. 4.3) with borehole C9011B and C9015A data obtained during the CK14–04 cruise (Fig. 4.4). The averaged resistivity values by LWD were about 0.3 Ohm-m along C9015A and about 0.8 Ohm-m along C9011B, respectively. These averaged values agree with the inversion result (Fig 4.3). Therefore, the inverted model is consistent with the LWD results. It is apparently reliable. Proof of the reliability of the inverted resistivity was found from borehole C9011B and C9015A data obtained during the CK14–04 cruise survey. The averaged resistivity values to the depth of about 30 mbsf obtained through LWD were, respectively, about 0.3 Ohm-m along C9015A and about 0.8 Ohm-m along C9011B (Takai *et al.* 2015). These averaged values are agreeable with the inversion result in which C9015A is located in the more conductive seafloor than C9011B.

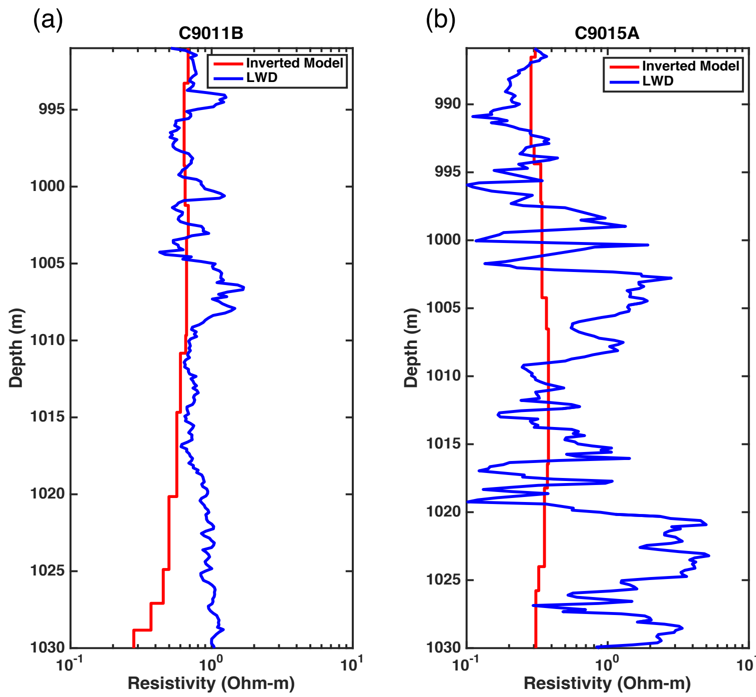

Figure 4.4. Comparison between the inverted resistivity model and LWD resistivity for boreholes: (a) C9011B and (b) C9015A (Takai *et al.* 2015).

4.4.3 Sensitivity test

Sensitivity studies were conducted to assess the ability of the towed ERT survey to map SMS deposits. To estimate the sensitivity, I use the equation proposed by (Schwalenberg *et al.* 2002) below.

$$s_j = \sum_i^j \left\| \frac{1}{e_j} \frac{\partial \mathbf{F}_i[\mathbf{m}]}{\partial m_j} \right\| \tag{4-1}$$

Therein, s stands for the sum of sensitivity; e denotes the error of the data to weight sensitivity. Sensitivity was also divided by the area of each model block in the original form by Schwalenberg *et al.* (2002). The sum of sensitivity calculated from the inverted model in Fig. 4.3 is presented in Fig. 4.5. The sum was normalized by the maximum sensitivity so that the maximum value is 1. A general decrease of sensitivity with depth is observed, which is a general feature of ERT data. Results demonstrate that the high sensitivity area (greater than -1.5 in logarithmic values) is distributed at 1030 m depth from the sea surface and show that much deeper or distant areas have less sensitivity.

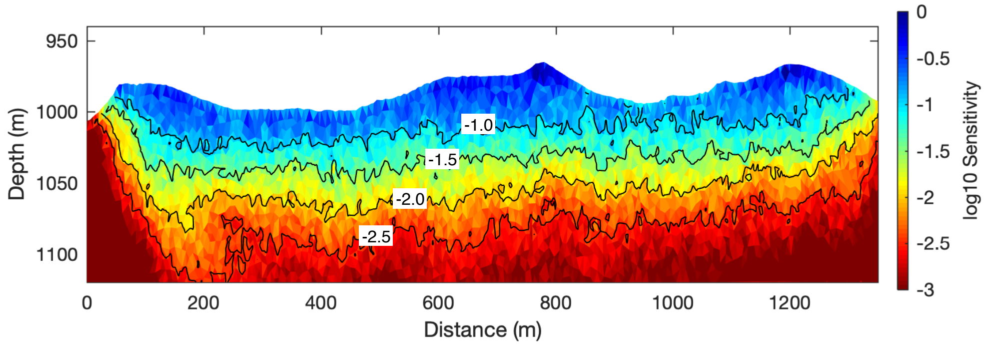

Figure 4.5. Resulting sums of sensitivity weighted by data errors from the inverted model in Fig. 4.3. Sums were normalized by maximum sensitivity so that the maximum value is 1.

Studies were conducted to ascertain how the deep-towed ERT survey can detect conductive zones CD1 and CD2 shown in Fig 4.3. The synthetic test is based on the real field survey in the Iheya North hydrothermal field, Okinawa Trough. The model consists of background and exposed and buried deposits. The background resistivity is 1.0 Ohm-m; both resistivities of the exposed and buried SMS deposits are 0.2 Ohm-m (Figs. 4.6a and b). This model is based on the one inverted from observed data depicted in Fig 4.3. The models include fixed parameters for the seawater (0.3 Ohm-m). The model was used for the forward calculation to obtain the synthetic response. Then 2% Gaussian random noise was added to provide a realistic test of the inversion algorithm. The number of data (synthetic apparent resistivity) is 966 without the electrode pairs P3–P4 and P5–P6 based on the real configuration of the data acquisition. The starting and prior models for the inversion are 1.0 Ohm-m homogeneous half-space, except for the seawater blocks. The grid number for the forward modeling is 16327. The inversion parameter is 6186 without updating seawater.

The calculated response from the model with Gaussian random noise is shown in Fig. 4.6d. The responses have extremely low apparent resistivity zones at 600–800 m with 2–3 *n*-Level, similar to the observed result (A1 in Fig. 4.2a). However, the observed low apparent resistivity (A2 in Fig. 4.2b) was not found in the synthetic response (at large *n*-Level in Fig. 2.12d). The inverted model shown in Fig. 4.6c reached the target RMS misfit 1.0, which means that the averaged misfit is within the assumed error, and that the inversion to the synthetic data is done successfully. However, again, no low-resistivity anomaly at deep parts was imaged, although the inverted model from the real observed data in Fig. 4.2a has a low-resistivity anomaly (CD2).

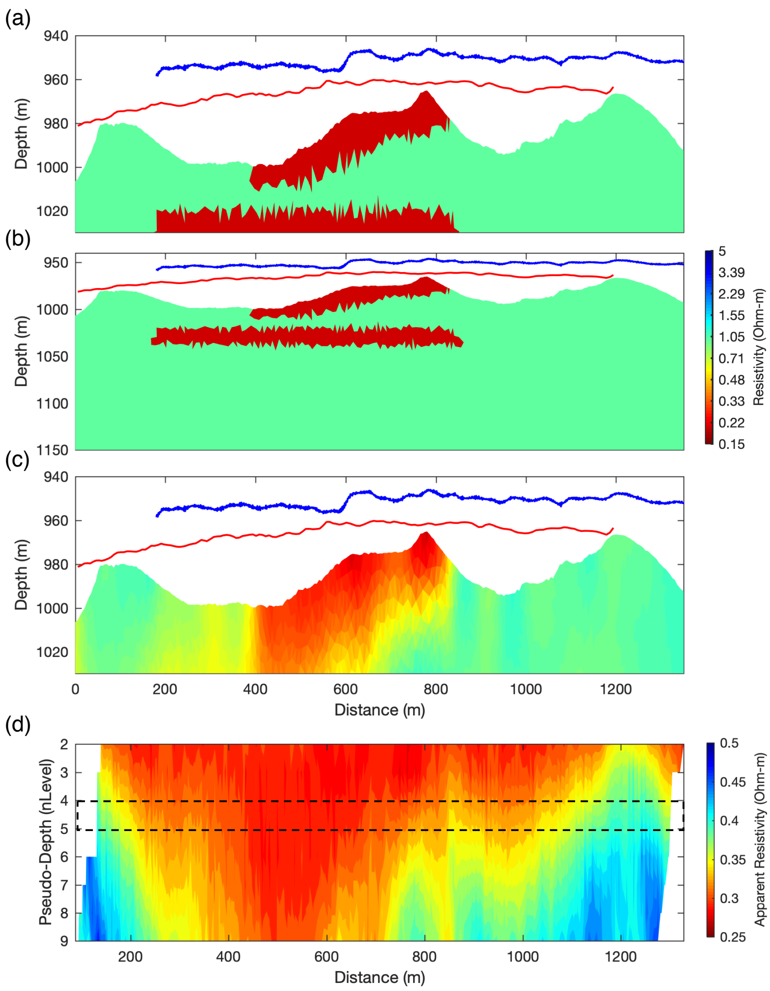

Figure 4.6. Synthetic model based on an actual field survey used to demonstrate the ERT survey performance for inversion. This model includes two conductive SMS deposits and background sub-seafloor. Blue and red lines respectively show the positions of the deep-towed and tail systems. Resistivities of both exposed and buried anomalies are 0.2 Ohm-m. (a) Model for generating synthetic data plotting at same size of Fig. 4.3. (b) Overall view of (a). (c) Inverted model. (d) Pseudo-section of the response from the synthetic model of Fig. 4.6a. Missing observed data points at *n*-levels (4 and 5) enclosed by dashed lines were interpolated from neighboring points.

To understand how the low apparent resistivity, observed as A2 in Fig. 4.2b, can be made, I presumed another model having a thin low-resistivity anomaly and a thicker and lower-resistivity anomaly (Figs. 4.7a and b). The same conditions as those used for forward and inversion procedures (data array, meshes, initial and prior model, and added noises) were used for this test. The response calculated from the model with Gaussian random noise, shown in Fig. 4.7d, indicated the extremely low apparent resistivity zones at 400 m at the 7–9 *n* Level, which is consistent with the low-resistivity zone A2 in Fig. 4.2b. The inverted model presented in Fig. 4.7c reached the target RMS misfit 1.0. This inverted model has a deep low-resistivity anomaly similar to that of CD2 in Fig 4.3. Results from these tests support the inference that the true model of the observed data in the Iheya North hydrothermal field has thin low-resistivity anomaly on the seafloor and buried very-low-resistivity anomaly at a deeper part.

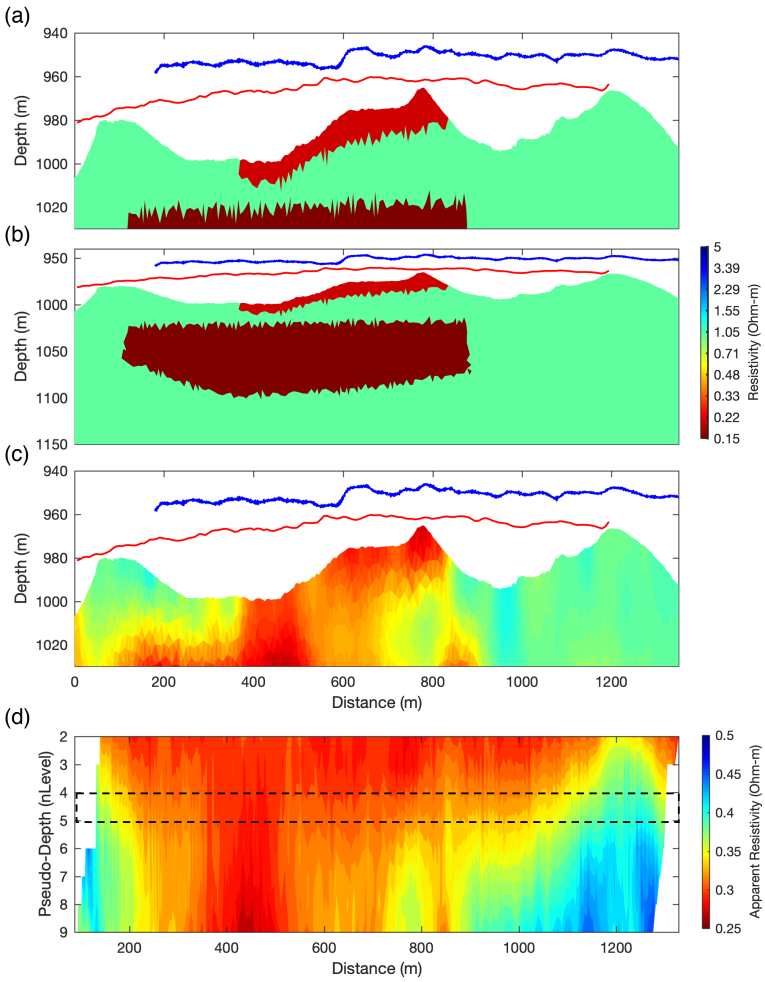

Figure 4.7. Synthetic model based on the real field survey used to demonstrate the ERT survey performance for inversion. This model includes two conductive SMS deposits and the background sub-seafloor. Blue and red lines respectively show the deep-towed and tail system positions. The exposed one is 0.2 Ohm-m; the buried one is 0.05 Ohm-m. (a) Model for generating synthetic data plotting at same size of Fig 4.3. (b) Overall view of (a). (c) Inverted model. (d) Pseudo-section of the response from the synthetic model of Fig. 4.7a. Missing observed data points at *n*-levels (4 and 5) enclosed by dashed lines were interpolated from neighboring points.

I also applied sensitivity tests by forward modeling to evaluate the existence of conductivity anomalies CD1 and CD2 where the conductive region is replaced with the blocks of 1.0 Ohm-m. The test model for CD1 (*i.e.* the conductive zone CD1 is removed) is presented in Fig. 4.8a. The calculated response from model is shown in Fig. 4.8b. The calculated responses tend to plot away from the observed responses at 300–600 m. Results show that RMS misfit increased from 2.17 of the model in Fig 4.3 to

5.02. Furthermore, the test model for CD2 (*i.e.* the conductive zone CD2 is removed) is shown in Fig. 4.9a. The calculated response from the model is shown in Fig. 4.9b. No very low apparent resistivity zone exists, although a low-resistivity zone (A2) was observed in the actual data. The RMS misfit increased from 2.17 to 3.37. Consequently, conductivity anomalies CD1 and CD2 are regarded as important features.

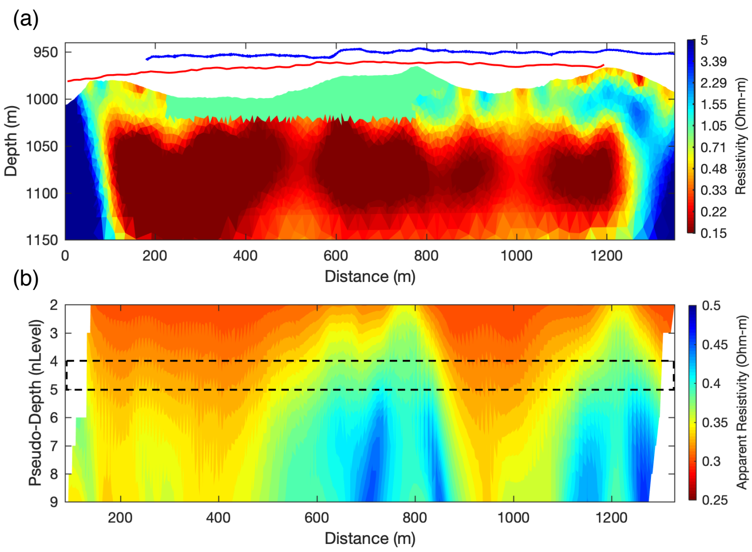

Figure 4.8. (a) Model used for the sensitivity test. The conductive area at the shallow part was replaced by 1.0 Ohm-m. (b) Response calculated from the model. RMS misfit changed from 2.17 to 5.02. Missing observed data points at *n*-levels (4 and 5) enclosed by dashed lines were interpolated from neighboring points.

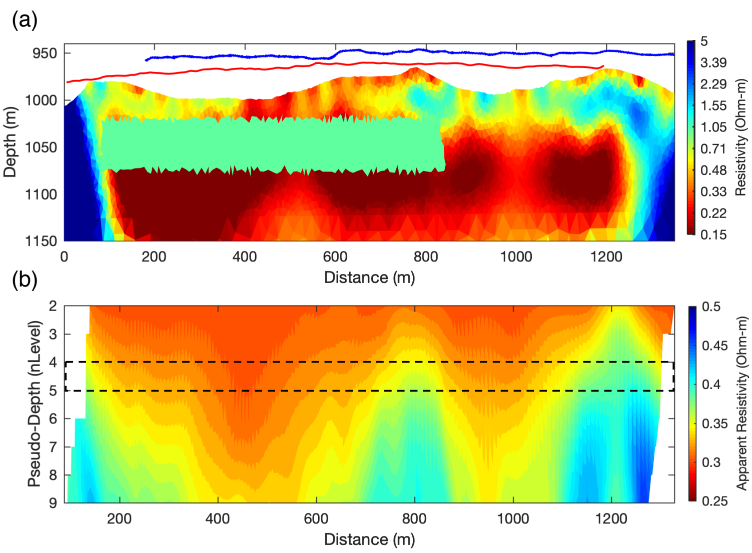

Figure 4.9. (a) Model used for sensitivity tests. The conductive area at the deep part was replaced by 1.0 Ohm-m. (b) Response calculated from the model. RMS misfit changed from 2.17 to 3.37. Missing observed data points at *n*-levels (4 and 5) enclosed by dashed lines were interpolated from neighboring points.

The inverted model in Fig. 4.3 has strong lateral variations near the seafloor. To investigate the ERT inversion ability of resolving small structures near the seafloor, I conducted sensitivity tests using synthetic data. The model consists of background and three small structures. The background resistivity is 1.0 Ohm-m. The small structures (25 m × 10 m) are 0.1 Ohm-m (Fig. 4.10). The model was used for the forward calculation to obtain the synthetic response. The same conditions as those used for forward and inversion procedure (data array, meshes, initial and prior model, and added noises) were used for this test. Inversion well recovered the small structures because the ERT data are much more sensitive to horizontal heterogeneities than vertical ones because of the data horizontal sampling rate 7.5 m with six electrode pairs.

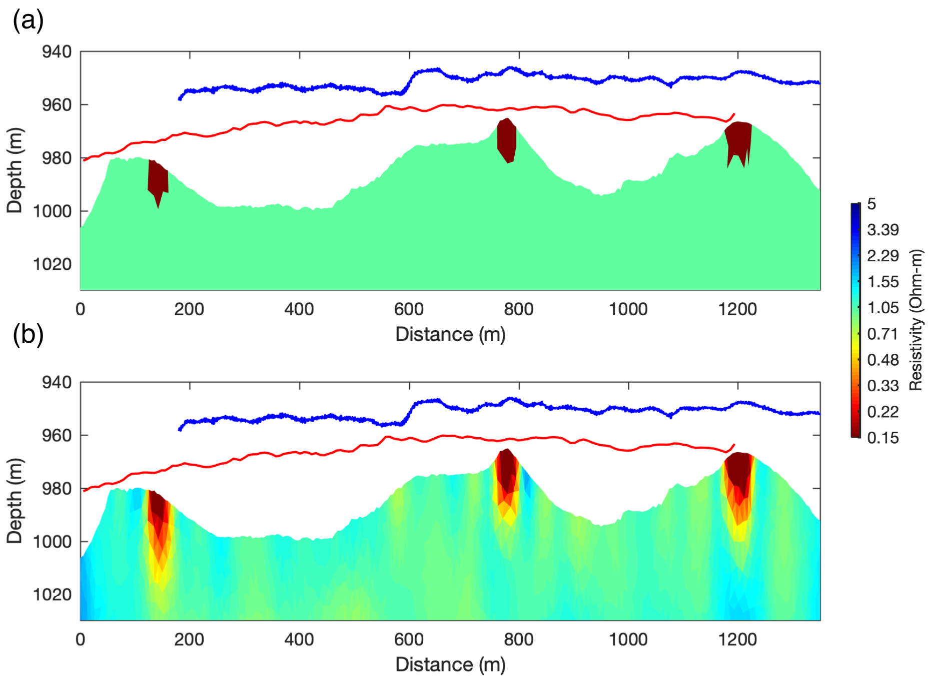

Figure 4.10. Synthetic model based on the real field survey used to demonstrate the ability of resolving small targets. This model includes three conductive SMS deposits (0.1 Ohm-m) and the background sub-seafloor (1.0 Ohm-m). Blue and red lines respectively show positions of the deep-towed and tail systems. (a) Model for generating synthetic data plotting at same size of Fig. 4.3. (b) Inverted model.

4.4.4 Effect of cable attitude

To investigate the cable slack effects, I show the distance between head and tail of towed cable behind the deep tow system, acoustically determined by SSBL (Fig. 4.11). The actual cable length as 192 m. The distance between the head and tail of the cable becomes minimum (187 m) at horizontal distance of 700 m, 2.6% shorter than the cable length. The apparent resistivity for all n-levels is biased by the cable slack. If I simply assume that the electrode location is proportionally shifted due the shortening of electrode array, then 2.6% overestimation of apparent resistivity for all n-levels is predicted as the maximum bias. Fortunately, the value is much less than the spatial variation of apparent resistivity through towing (Fig. 4.2b). In addition, the spatial change of measured distance (Fig. 4.11) has little correlation with the spatial changes of observed apparent resistivity of all n-Levels (Fig. 4.2b). I conclude that electrical responses from the sub-seafloor structures are more significant than the bias error by the cable slack. The effects caused by cable slack are minor in the inversion result.

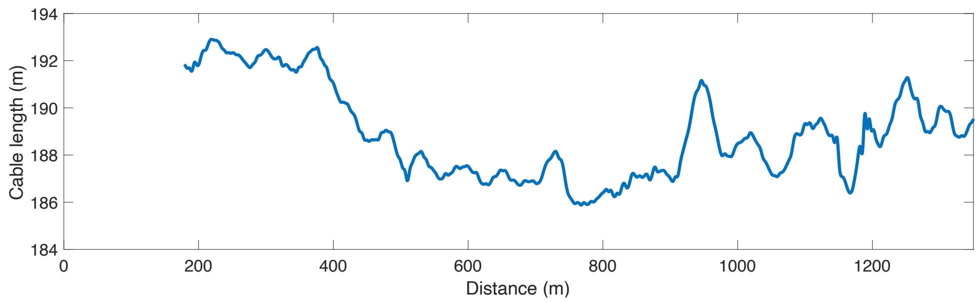

Figure 4.11. Distance between the head and tail position by SSBL. Distance shows the position of the towed system head.

Ishizu *et al.* (2019b) demonstrated using synthetic tests how the inversion results are distorted because of pitching of the towed cable behind the deep tow system (Fig. 4.12). For the tests, a 0.21 Ohm-m conductive block is embedded into a 1.0 Ohm-m homogenous half-space with a flat seafloor. The anomaly is embedded 5–35 m below the seabed. The survey configuration is the same as that shown in Fig. 1.6 where the water depth is 1,000 m and the deep tow system altitude is fixed at 10 m. I varied the pitching of the towed cable within a range of +/- 2 degrees (positive = pitch-up, negative = pitch-down). The apparent resistivity values along towing are calculated using forward modeling. Synthetic data are used for the inversion generated under a condition by which the towed electrodes are arranged horizontally, although the pitching is not always zero. The distortions by the pitching are not severe in the inversion results when the pitching error is less than 2 degrees (Fig. 4.12). Actually, the acoustic positioning error of the cable's tail in the system results in the pitching error of less than 2 degree.

The yaw (or strike) of the towed cable with electrodes can also be ascertained acoustically using SSBL. The angle between the towed cable and the survey profile is shown in Fig. 4.13; the average is 12.8°. In such cases, ERT surveys in real fields frequently found proper subsurface structures. Kwon *et al.* (2005) conducted water-surface ERT surveys with a floating streamer cable to image fault zones beneath a riverbed. In their survey, the parallel ERT profiles are not perpendicular to the known geological strike (intersecting the faults obliquely with horizontal angle of about 70–80°), but their 2D inversion results well-imaged the geological faults as low resistive zones at the proper locations. I believe that the ERT survey can also image the sub-seafloor 2D structure properly, although it might be distorted slightly because of the yawing.

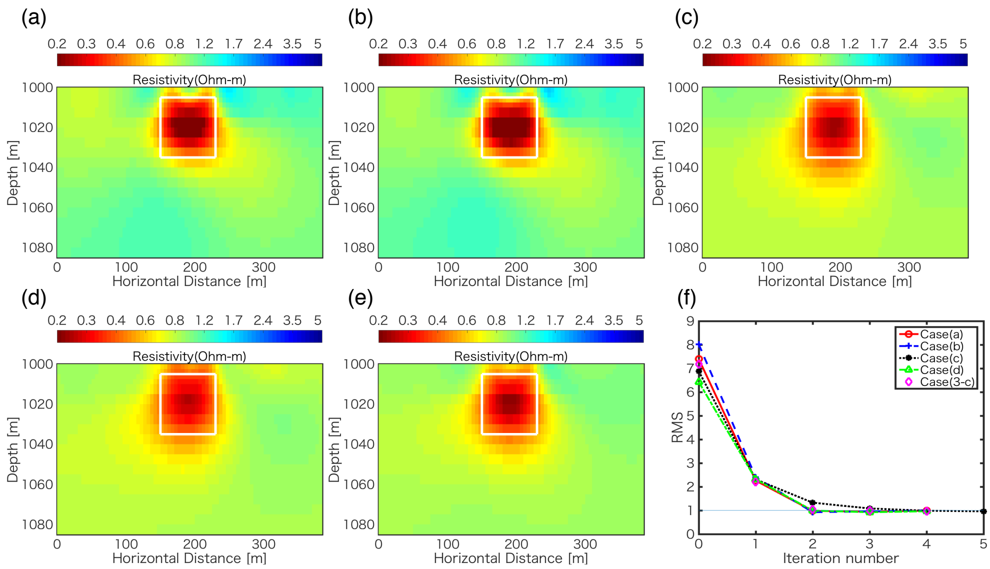

Figure 4.12. Inversion results for synthetic tests show the marine ERT as robust against the pitching of the towed electrode array (Ishizu *et al.* 2019b). In the inversion, the cable is assumed to be towed horizontally, although it tilts with angles of (a) 1 deg, (b) 2 deg, (c) -1 deg, (d) -2 deg, and (e) 0 deg. (f) RMS misfit versus iteration number. White rectangles represent the true locations of the conductive block below the seafloor.

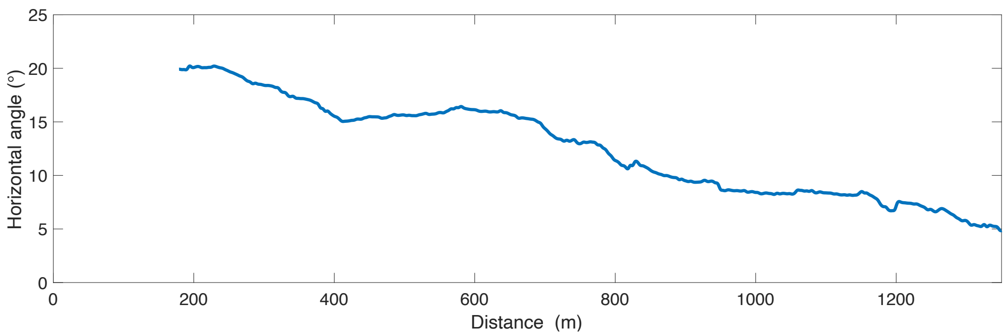

Figure 4.13. Yaw of towed cable behind the deep tow system (horizontal angle between the towed cable and the survey profile). The angle is oriented clockwise. Distance shows the towed system head position.

4.4.5 Effect of 3D topography

The occurrences of SMS deposits are linked to local 3D topography at horizontal distance of 750 m along the towed profile, thus possible distortions of the 3D topographic effects must be considered. An estimated model by 2D inversion of data from a 3D conductive structure might contain artifacts below and next to the conductive mound (CD1). However, I believe that the conductive mound can be resolved as discussed in the numerical studies by Haroon *et al.* (2018). Higher resistivities were recovered around horizontal distance of 1200 m, where there is a strong topography adjacent to the profile (Fig 4.3). However, the adjacent volcanic summit is located far from the towed profile (300 m). There is no large relief around the profile at horizontal distance of 1200 m (Fig. 4.1a). Therefore, the topographic effects are negligible compared to responses from the resistivity structures below the profile.

4.5 Interpretation of resistivity model combined with other geophysical data

Rock resistivity depends on diverse factors such as the porosity, temperature, salinity of pore water, and metal and clay contents. To assess the possibility that low conductivities CD1 and CD2 in Fig 4.3 are attributable to the existence of metal, one must account for these effects on resistivity. In the Iheya North hydrothermal field, average values of porosity measured from core C0016 (at the same location of NBC) were less than 25 and 10%, respectively, at 0–10 and 20–30 mbsf (Takai *et al.* 2015). From ambient seafloor temperatures to around 300 °C, the resistivity of water solutions decreases concomitantly with increasing temperature (Quist & Marshall 1968). This decreased resistivity is attributable to increased mobility of the ions caused by decreased water viscosity. The relation described by Dakhnov (1962), designated as T-model 1 in this study is presented below.

$$\rho_w = \frac{\rho_{w_0}}{1+\alpha(T-T_0)} \tag{4-2}$$

In that equation, ρ_w represents the fluid resistivity at temperature T, ρ_{w0} stands for resistivity of the fluid at temperature T_0, and α denotes the temperature coefficient of resistivity (0.025 °C^{-1}). A similar equation by Chave *et al.* (1991), designated as T-model 2 in this study, is

$$\rho_w = 1/(3+\frac{T}{10}) \tag{4-3}$$

The average temperature and resistivity of the seawater were measured respectively using CTD as 4.08 °C and 0.3062 Ohm-m, during the towing experiment. The highest measured temperature of hydrothermal fluid was about 300 °C at the NBC discharge zone. ρ_w at temperature of 300 °C is 0.0365 Ohm-m based on eq. (4-2), and 0.030 Ohm-m by eq. (4-3). Herein, I estimate the bulk electrical conductivity with these ρ_w values using a rock-physics equation proposed by Ohta *et al.* (2018).

$$\begin{aligned} \sigma_R &= \left(\frac{F_2F_3}{F_3\sigma_w+F_2C_e}+\frac{F_1}{\sigma_w}\right)^{-1}+C_s \\ F_1 &= (1-x)/\Phi^m \\ F_2 &= x/\Phi^m \\ F_3 &= x \end{aligned} \tag{4-4}$$

In those equations, σ_R and σ_w respectively represent bulk conductivity and fluid conductivity, Φ denotes porosity, m is the cementation factor in Archie's law (originally constructed by Archie, 1942), C_s and

C_e respectively stand for surface conductance and conductance of conductive metallic mineral filled in pore spaces, and x is the volumetric ratio of the pore throat including the conductive metallic mineral. The equivalent circuit for a rock physics model is shown in Fig. 4.14. As pointed out by (Revil *et al.* 2015), the SMS deposits normally decrease the overall conductivity as long as they are disconnected, whereas the model by Ohta *et al.* (2018), based on the electrical connections by mixing of SMS and conductive pore water, well explains the observed core-based resistivity features (*e.g.* lower bulk resistivity than the pore water).

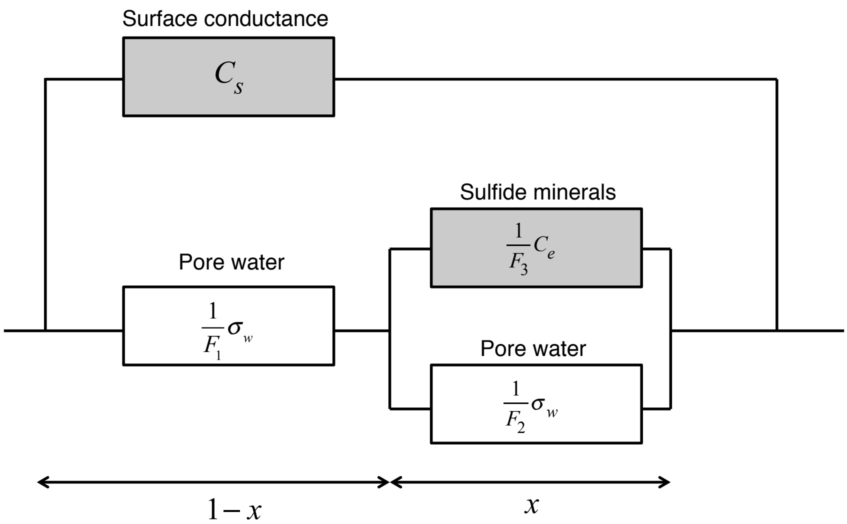

Figure 4.14. Equivalent circuit for a rock physics model (Ohta *et al.* 2018).

According to Ohta *et al.* (2018), a relation between C_e and volumetric ratio of conductive metallic mineral, Φ_v, can be written as

$$\Phi_v = (3.61 \pm 0.78)\ln C_e + (3.86 \pm 3.24) \quad \textbf{(4-5)}$$

based on laboratory measurements. Additionally, from a number of core measurements, (Ohta *et al.* 2018) reported the averaged values of parameters in eq. (4-5): C_s=0.11 S/m, m=1.4, and x=0.94. The bulk resistivity ($1/\sigma_R$) is calculable from eq. (4-5). The relation between bulk resistivity and temperature of pore fluid for each T-model is shown in Fig. 4.15. Some examples are that it is about 0.21 Ohm-m when ρ_w =0.0365 Ohm-m, Φ=10%, and C_e=5 S/m (*i.e.* Φ_v =9.4%; 5.2–14.2% with the parameter errors in eq. (4-5)). Under these temperature and porosity conditions, this value implies that much higher contents of conductive metallic minerals are necessary for bulk resistivity lower than 0.20 Ohm-m. These engender the explanation that conductive metallic minerals contribute strongly to low conductivity CD1 and CD2 in Fig. 4.3.

For explanation of the deeply buried conductive zone (CD2, less than 0.2 Ohm-m), with porosity less than 10% and temperature of 300 °C based on the measured maximum value of hydrothermal fluid at NBC, the rock-physics equation gives the conductive SMS minerals with volume amount greater than 9% (Fig. 4.15). In other words, under the assumed porosity (≤ 10%), high temperatures (high conductivity) of pore fluids alone cannot explain the low resistivity of less than 0.2 Ohm-m in CD2. The existence of conductive SMS minerals is consistent with rock-core observations at 27–45 mbsf of Hole C0016, drilled at NBC, containing approximately 5% sulfide with very fine-grained pyrite (Takai *et al.* 2011). Similar contents of fine-grained sulfide minerals (3%: Takai *et al.* 2015) were also confirmed in the recovered cores at about 23–31 mbsf at Hole C9015B drilled by the CK14-04 cruise.

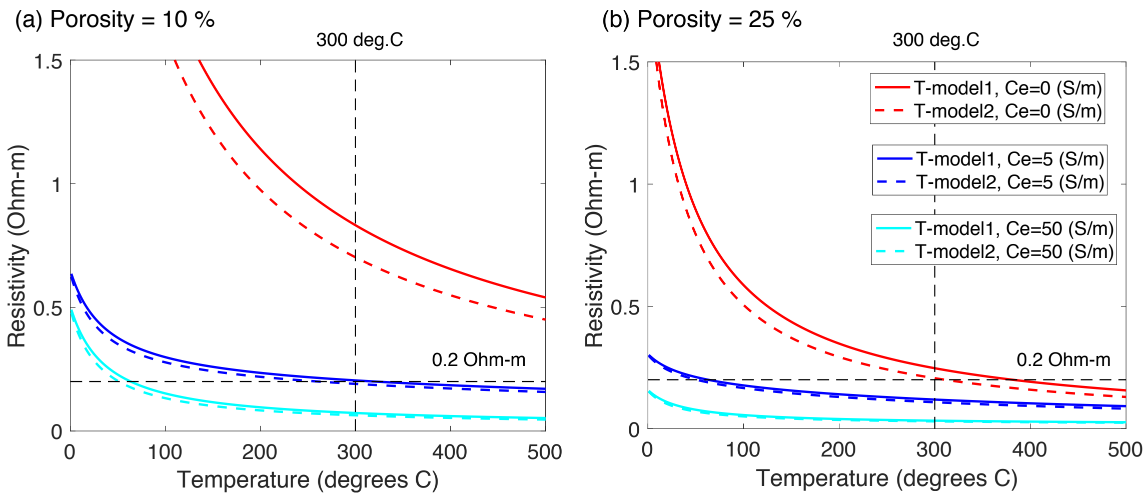

Figure 4.15. Relation between bulk resistivity and temperature of pore fluid for each T-model with a set of C_e (0, 5, 50 S/m). Porosity is (a) 10 and (b) 25%.

For the shallow seafloor conductive zone (CD1, around 0.2 Ohm-m), the same equation indicates absence of conductive SMS minerals under porosity of 25% and temperature of 300 °C (Fig. 4.15). However, X-ray diffraction analysis of rock samples from the Iheya North hydrothermal field indicated the volume amount of conductive SMS minerals as 18–49% (Ohta *et al.* 2018). The temperature is expected to be much lower than 300 °C because of cooling by seawater. Therefore, CD1 also requires greater amounts of conductive SMS (*e.g.* greater than 9% at a temperature of about 100 °C). Note that I only discussed conductive SMS. The cores from Hole C0016B at 6–9 mbsf consist of massive sulfide ore containing 40–60% sphalerite (non-conductive SMS), 10–20% pyrite, and a few percent each of galena and chalcopyrite (Takai *et al.* 2011). The total amount including both conductive and non-conductive SMS would be much more than that of only conductive SMS.

The seawater salinity also decreases the resistivity with a linear relation (Keller 1988). The minimum salinity measured at discharge zones above vents is 30% smaller than that of seawater. However, such slight fluctuation of seawater salinity cannot explain the low resistivity of 0.2 Ohm-m. I also devote attention to the clay minerals. Actually, core samples obtained at depth 30 mbsf (C0016) contain chlorite (Miyoshi *et al.* 2015). However, laboratory measurements demonstrate a minor effect of clay in electrical conduction (Ohta *et al.* 2018). In addition, logging data measured in land hydrothermal areas often show low resistivity at the clay-rich layer, but the typical value is around 1.0 Ohm-m (*e.g.* at drilling around Mt. Aso, Japan, as reported by New Energy and Industrial Technology Development Organization (NEDO) 1995). This resistivity value is insufficient for causing low resistivity (0.2 Ohm-m). Therefore, I conclude that conductive zones CD1 and CD2 can both be attributed to SMS deposits.

The semi-layered resistivity structure is supported by the multi-channel seismic reflection data recorded on the KR 10-02 cruise (Tsuji *et al.* 2012). To characterize the shallow structures close to the seafloor precisely, the shallow reflectors were carefully analyzed in seismic data analysis (*e.g.* velocity analysis). The seismic profile highlights strong reflectors with positive polarity below the venting sites (southern half of the survey profile; Fig. 4.3), which implies the existence of rock layers with high acoustic impedance. The reflective layer, which is recognized horizontally and as extending widely below the seafloor, corresponds to the top of the deep conductive zone, CD2. This observation supports no indication of a huge reservoir of hydrothermal fluids at CD2. Altered volcanic rocks with quartz–chlorite–pyrite and pyrite–anhydrite veins were found in cores recovered from Hole C0016 (27–45 mbsf; Takai *et al.* 2011). Another drilling result at 23–31 mbsf in Hole C9015B indicated highly silicified quartz-rich rocks with 3% fine-grained SMS (Takai *et al.* 2015). The altered volcanic and silicified quartz-rich rocks are probably harder than the near-seafloor unconsolidated materials, resulting in strong amplitude layers with positive polarity. In addition, the layers might have lower permeability than their surroundings because gypsification of the anhydrite and silicification engender rapid closure of pore spaces and fractures in the host rock.

4.6 Conclusions

I applied a deep-towed ERT system to clarify the electrical resistivity structures of SMS deposits in the Iheya North hydrothermal field, the Okinawa Trough, southwestern Japan. The resistivity image by the inversion analysis revealed that the highly conductive zones below the seafloor were consistent with observed hydrothermal venting sites and heat anomalies. This high conductivity is probably attributable to rich conductive SMS minerals, not only to high-temperature fluids, clay minerals, and salinity of pore fluids. The recovered resistivity cross-section indicates a semi-layered structure consisting of exposed and deeply embedded SMS deposits. The cap rock layer is also inferred from a seismic reflection survey and seafloor drillings. This study represents the first reported success in detailed imaging of SMS deposits, which demonstrates the effectiveness of the marine deep-towed ERT system for exploration and characterization of SMS deposits.

Chapter 5

Application to observed CSEM data for deep resistivity structures

5.1 Introduction

SMS deposits are often associated with mound structures and complex bathymetry. These environments make resistivity structures in the area of SMS deposits 3D. Haroon *et al.* (2018) applied a 2D inversion algorithm (MARE2DEM; Key 2016) to synthetic CSEM data generated from a realistic 3D resistivity model of SMS deposits using 3D forward modeling. The inverted 2D model recovered the mound SMS deposits, but several artifacts were also imaged due to the 3D resistivity effects. 3D CSEM inversion algorithms are necessary to more precisely estimate resistivity structures of SMS deposits. However, 3D inversion algorithms have not been applied to CSEM data for imaging of SMS deposits. Therefore, imaging techniques of resistivity structures of SMS deposits using CSEM inversion algorithms are far from established.

A new hydrothermal field in mid-Okinawa Trough, southwestern Japan called Ieyama was found by a preliminary survey using a ship and a subsequent detailed survey using AUV (Kasaya *et al.* 2020). In the hydrothermal field, a clear negative self-potential zone and mound structures were observed. Therefore, SMS deposits formed through the hydrothermal activity are expected to be in the field. Marine CSEM data were collected for investigating resistivity structures of SMS deposits in the field. I image 3D resistivity structures of SMS deposits by applying the algorithm to CSEM data collected in the hydrothermal field.

5.2 Ieyama hydrothermal field

The target area for this study is located in the mid-Okinawa Trough, southwestern Japan (Fig. 5.1). The Okinawa Trough is a back-arc basin of the Ryukyu arc-trench system. Two major hydrothermal fields of Iheya and Izena in the mid-Okinawa Trough have been well investigated (Ishibashi *et al.* 2015). A new hydrothermal field called Ieyama was found through a preliminary survey using a ship and a subsequent detailed survey using an AUV (Kasaya *et al.* 2020). The preliminary survey collected bathymetry, backscatter, and water column data using MBES system on the ship. These data were used for narrowing the target hydrothermal area. The area narrowed by the preliminary survey was further investigated using a self-potential survey and a highly accurate MBES system on an AUV. Clear negative self-potential zones and hydrothermal vents were observed in the Ieyama hydrothermal field. Field surveys conducted in the area of known SMS deposits revealed that the observed negative self-potential anomalies were correlated with the SMS on the seafloor and below the seafloor (Kawada & Kasaya 2017). Therefore, SMS formed through the hydrothermal activity is expected to be in the field.

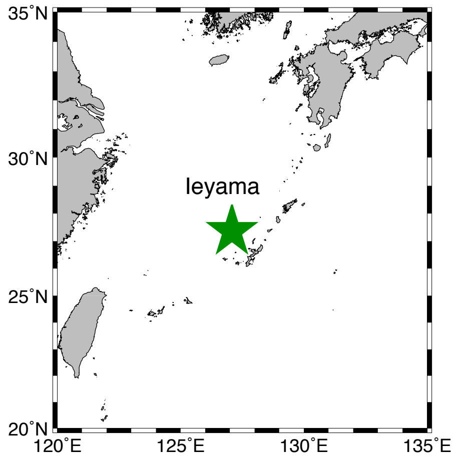

Figure 5.1. Map of the study area. The green star shows the location of the Ieyama hydrothermal field, Okinawa Trough, southwestern Japan.

5.3 Observed CSEM data

A CSEM survey was conducted in the Ieyama hydrothermal field during 6–11 Oct. 2017 using the research vessel Kaimei from JAMSTEC. A marine electromagnetic system called MEMSYS was used to transmit an electric current (Kasaya *et al.* 2019). MEMSYS has a 200 m long cable including a 28.3 m horizontal dipole antenna for transmitting a current and 9 potential electrodes to record potential for direct current and self-potential surveys (Fig. 5.2). MEMSYS transmitted a 0.125 Hz square wave current of approximately 60 A (zero to peak) in this survey. The towed speed of MEMSYS was about 0.5 knots for each survey line. The ambient seawater temperature and electric conductivity were measured using a CTD sensor mounted on the towed system during towing. The deep-tow and tail positions of the cable were monitored using acoustic transponders. The towed height from the seafloor was 20–60 m depending on the topography below the system.

Four OBE sensors and two mobile OBE sensors were deployed on the seafloor to measure the horizontal electric fields at a sampling rate of 1 kHz (Kasaya & Goto 2009). The four OBE sensors with 4.4 m dipole length were dropped from the ship (Rx 1, 3, 5 and 6). The two mobile OBE sensors with dipole length of 1.4 m were carried directly to the seafloor (Rx 2 and 4) using a ROV. The positions of OBE sensors are overlaid on the bathymetry map with towing lines of MEMSYS (Fig. 5.3). Magnetometers were equipped on the OBE sensors to measure the OBE sensor rotation.

The frequency domain transfer function was converted from time series data of voltage recorded at OBE sensors using a robust processing scheme proposed by Myer *et al.* (2011). Data were fast Fourier transformed over 8-s window length corresponding exactly to one waveform long. To calculate the CSEM transfer function, the voltage recorded at OBE sensors was normalized by the transmitted source dipole moment. The data were stacked by every four-wave cycle corresponding to a sample interval of approximately 30 m in the horizontal. The stacked transfer functions of CSEM data were then rotated into E_x and E_y using the dipole orientation recorded by magnetic field sensors. The processed amplitude data of E_x and E_y are presented in Fig. 5.4. Noisy data for which the error was greater than 50% were removed. Data with Tx-Rx offset was less than 100 m was also removed because of the navigation errors. Inputted data of the inversion algorithm is the $\log_{10}$-scaled amplitude of E_x and E_y without the phase at three frequencies of 0.125, 0.375, and 0.625 Hz. The data number for the inversion algorithm is N=3,833.

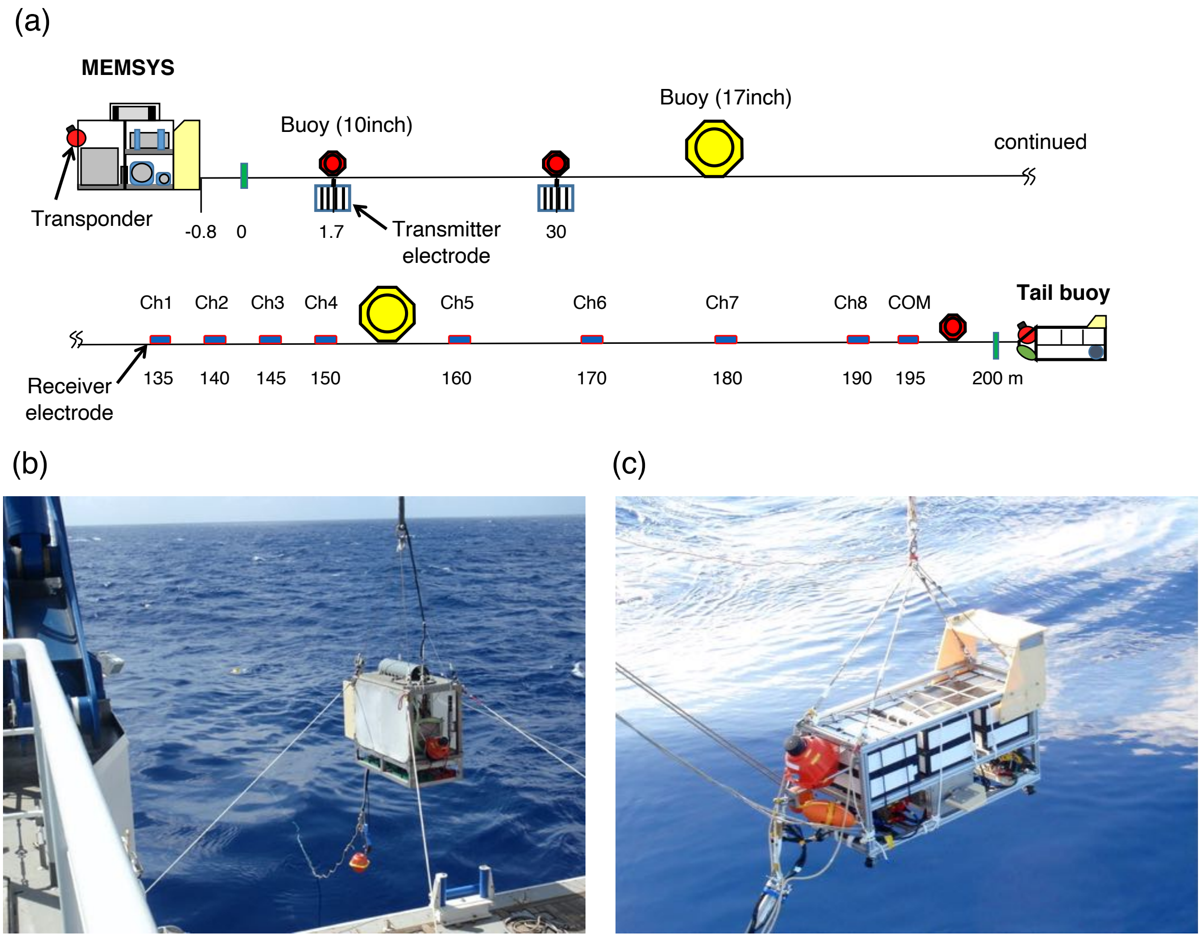

Figure 5.2. Equipment used for this study. (a) Configuration of MEMSYS with 200 m long cable terminated by a tail buoy system (Kasaya *et al.* 2019). A pair of transmitter electrodes with 28.3 m dipole length is mounted on the cable. Nine Ag/AgCl electrodes are mounted to measure the self-potential signal. (b) Photograph of the transmitter system. (c) Photograph of the tail buoy.

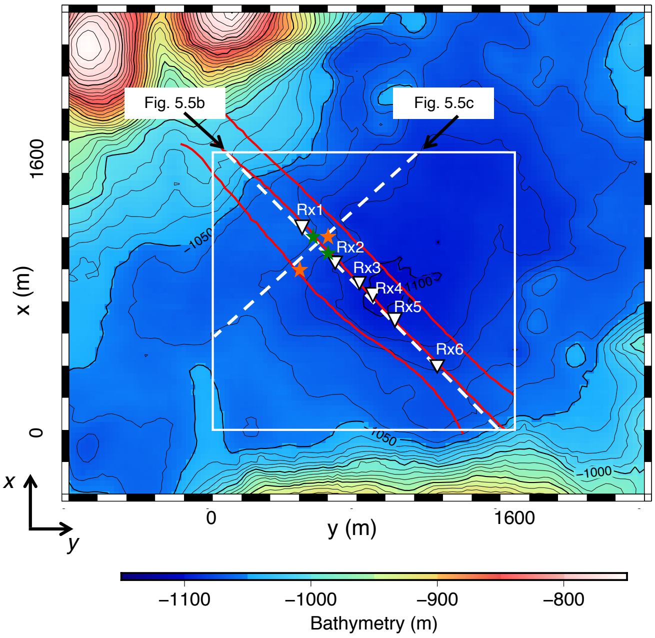

Figure 5.3. A bathymetric map overlain with OBE sensor deployment location (white triangles), three tow lines (red lines) and known vents (green stars). In the present study, x and y correspond to latitude and longitude, respectively. White box shows area shown inverted model in Fig. 5.5.

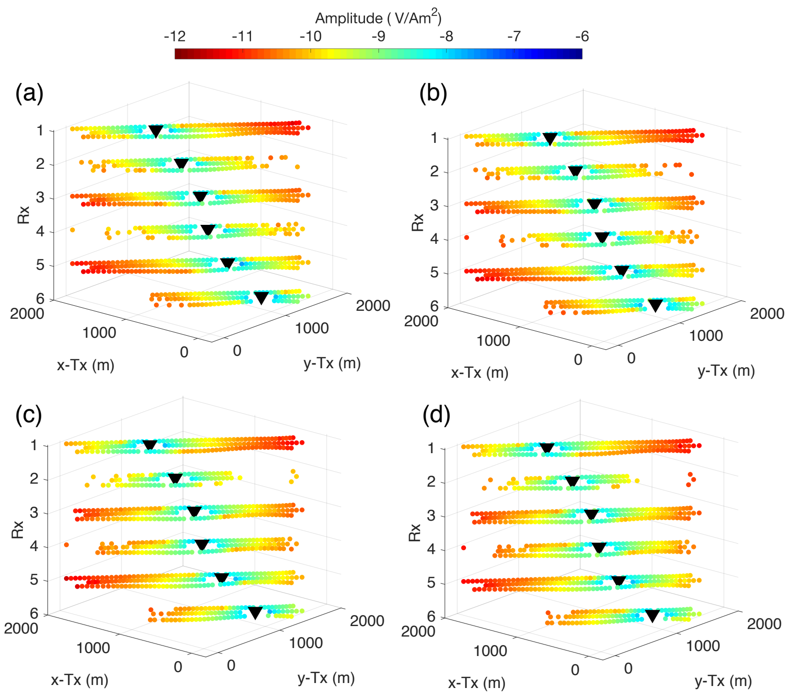

Figure 5.4. Electric data measured by OBE sensors at a frequency of 0.125 Hz. (a) Observed amplitude of E_x, (b) Calculated amplitude of E_x from the inverted model in Fig. 5.5. (c) Observed amplitude of E_y, (d) Calculated amplitude of E_y from the inverted model in Fig. 5.5.

5.4 Inversion results from the observed 3D CSEM data

5.4.1 Inverted model

The 3D inversion algorithm was applied to the processed CSEM data for imaging resistivity structures of SMS. A simple starting model consists of a highly resistive air layer (10^9 Ohm-m), a seawater layer of constant resistivity (0.304 Ohm-m) and homogeneous seafloor (1 Ohm-m). The model is divided into a grid of 67 × 67 × 66 cells including several boundary cells. For the horizontal cells, 50 m grid was used in the interest region. 10 m grid was used in the region from 950 m to 1,250 m below the sea surface for the vertical mesh. The inversion domain is limited to the interesting seafloor region, excluding boundary cells, air, and resulting in M=119,156 unknown model parameters. The model number M=119,156 is much larger than the data number N=3,833. Fig. 5.5 shows the inverted model of CSEM data recorded by six OBE sensors. The initial RMS misfit was 7.6. It reached 1.6 after 10 iterations. The response calculated from the inverted model is presented in Fig. 5.4.

The inverted model reveals sub-seafloor electric conductive zones immediately below the seafloor. The resistivity value (0.1–0.2 Ohm-m) is much lower than that of the backgrounds (1.0 Ohm-m). Low resistivity values in seafloor hydrothermal fields can result from diverse factors such as high porosity, high temperature of pore fluids, and the amounts of metallic minerals. Ishizu *et al.* (2019a) showed under the assumed porosity (≤ 10%), high temperatures (high conductivity) of pore fluids alone cannot explain the low resistivity of less than 0.2 Ohm-m. That low resistivity requires the existence of conductive SMS such as pyrite, galena, and chalcopyrite. The low-resistivity value is consistent with resistivity values of SMS deposits measured in the Iheya and Trans-Atlantic Geotraverse hydrothermal fields (Haroon *et al.* 2018, Ishizu *et al.* 2019a).

Vertical conductive zones $\{(x, y)$: 500 m $< x <$ 1,000 m, 500 m $< y <$ 800 m$\}$ were imaged immediately below the conductive zones on the seafloor. The resistivity value of vertical conductive zones is approximately 0.4 Ohm-m. The vertical zones might be attributed to the hydrothermal conduits, which upwell from the deep parts and which contribute to the formation of SMS. The observed hydrothermal vents were found above the vertical conductive zones (Fig. 5.5).

This report is the first describing results of imaging 3D resistivity structure of SMS. Although 2D inversion algorithms were applied to CSEM survey data for imaging mound type SMS (Haroon *et al.* 2018, Gehrmann *et al.* 2019), several artifacts appeared in the resultant models because of 3D resistivity effects. The result described in this chapter demonstrates that the 3D inversion algorithm is more appropriate for clarifying the true resistivity structure of SMS than 2D inversion algorithms because greater detail of 3D resistivity structures in the SMS area was detected. The SMS volume can also be estimated from 3D resistivity imaging, which contributes further to resource estimation.

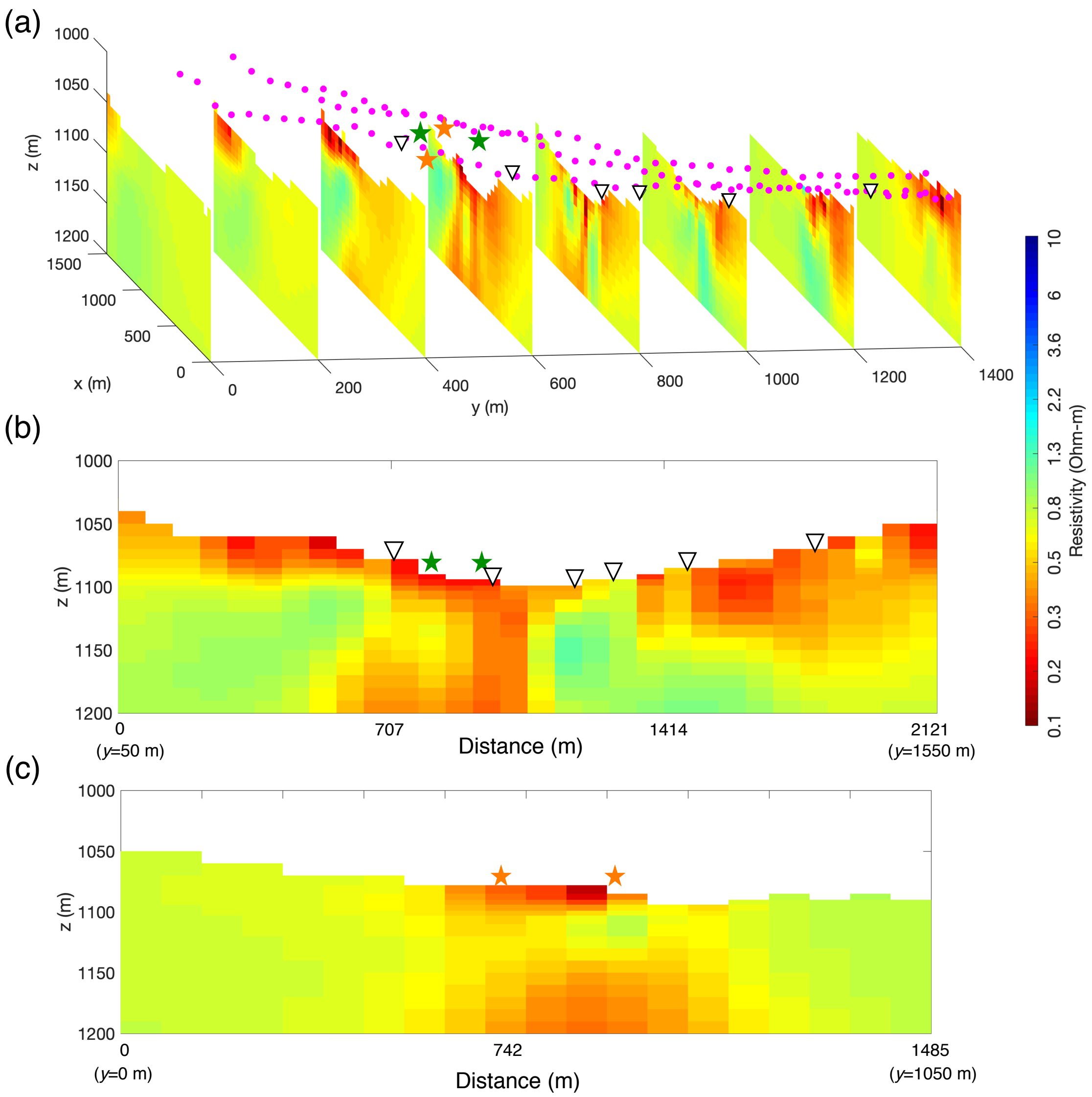

Figure 5.5. (a) Resistivity model resulting from 3D inversion of the observed CSEM data overlain by positions of transmitter (circles), receivers (triangles), and known vents (stars). *z* shows depth from the sea surface. (b) 2D section of the inverted model along tow line 2 shown in Fig. 5.3. (c) 2D section of the inverted model along the direction perpendicular to tow line 2.

5.4.2 Sensitivity test

The inverted conductive anomalies (0.1–0.2 Ohm-m) below the seafloor might be related to the formation of SMS deposits. SMS exists below the seafloor if the anomalies are true structures. My objective in this section is to demonstrate that the conductive anomalies are true structures, not artifacts from inversion. A sensitivity test was conducted to evaluate the ability of the CSEM data to constrain the conductive anomalies below the seafloor. The synthetic model of the sensitivity test consists of a background and two conductive anomalies on the seafloor (Fig. 5.6a). The background resistivity is 1.0

Ohm-m; resistivity of the conductive anomalies is 0.1 Ohm-m. The models include fixed parameters for seawater (0.304 Ohm-m). The model was used for forward calculation to obtain the synthetic data. The number of data is 3,833 from the same survey configuration with the field data. Then Gaussian random noise for which the level is the same with the observed data was added to provide a realistic test of the inversion algorithm. The starting and prior models for the inversion are 1.0 Ohm-m homogeneous half-space. The grid design and inversion parameter are consistent with the setting on the field data. The inverted resistivity model presented in Fig. 5.6b reached the RMS misfit 1.6 after four iterations, which is the same fitting level with the field data.

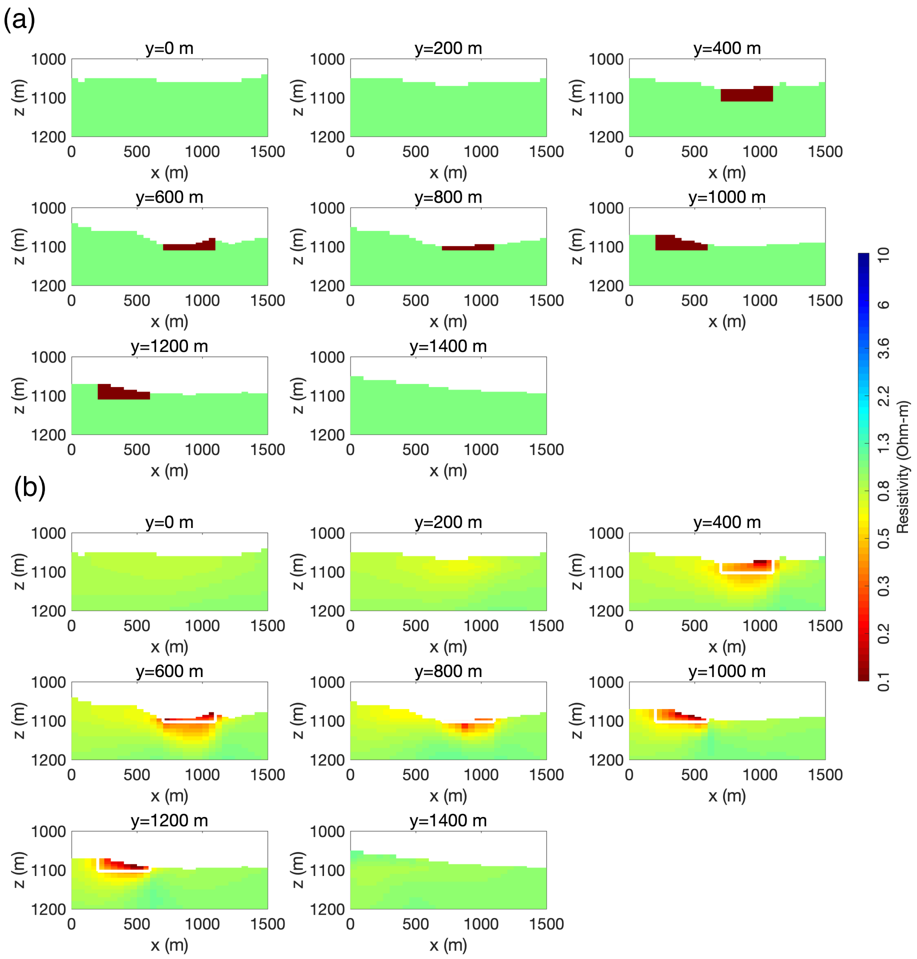

Figure 5.6. Synthetic model based on an actual field survey used to demonstrate the performance. This model includes 0.1 Ohm-m conductive anomalies and 1.0 Ohm-m background sub-seafloor: (a) model for generating synthetic data and (b) inverted model from the synthetic data. White lines mark the outline of the true conductive anomalies.

The inverted model from the synthetic data showed that the conductive anomalies on the seafloor can be imaged. Resistivity values and the shapes of the inverted anomalies are close to those of the true models. The conductive anomalies are well recovered on all *y*-sections, indicating that the quality of data at different transmitter and receiver offsets is not spatially biased. The numerical example shows that the conductive anomalies obtained from the actual field data must explain the data. Therefore, the conductive anomalies might be related to the formation of SMS deposits, not to the artifacts of the inversion.

5.4.3 Interpretation of resistivity model

The very low resistivity anomalies (0.2 Ohm-m) were recovered below the seafloor. The most of the shallow sub-seafloor is covered by the low resistivity. In seafloor hydrothermal fields, the low resistivity can be caused by diverse factors such as high porosity, high temperature of pore fluids and the amounts of metallic minerals. Rocks in the near seafloor often have higher porosity. Resistivity of highly porous rock shows lower resistivity due to the pore fluids. Average porosity of rock samples on the seafloor in the Iheya hydrothermal field is 41.6% (Ohta *et al.* 2018). Highly porous pumice layers were also identified by drilling surveys in the Iheya hydrothermal field (Takai *et al.* 2015). Using the rock physics model by Ohta *et al.* (2018) with 41.6% porosity, the 0.2 Ohm-m resistivity can be caused by the hot pore fluids (about 170 °C). This rock physics also indicate that the 0.2 Ohm-m resistivity requires conductive SMS such as pyrite, galena, and chalcopyrite such as pyrite, galena, and chalcopyrite if temperature of the pore fluids is less than 170 °C.

Vertical conductive zones $\{(x,y)$: 500 m $< x <$ 1000 m, 500 m $< y <$ 800 m$\}$ were imaged just below conductive zones on the seafloor. The resistivity value of vertical conductive zones is around 0.4 Ohm-m. The observed hydrothermal vents were found above the vertical conductive zones (Fig. 5.5). The vertical zones might be attributed to up-flow hydrothermal conduits, which upwell from the deep parts below the seafloor. The hydrothermal conduits often accompany stock-work SMS mineralization (Humphris *et al.* 1995). The vertical conductive zones are interpreted as the up-flow hydrothermal conduits, stock-work SMS, or both.

The 0.2 Ohm-m areas below the seafloor are connected to the vertical hydrothermal conduits. It indicates the hydrothermal fluids possibly flow laterally below the seafloor. The up-flow hydrothermal flows are guided by impermeable structures and they flow laterally below the seafloor. The near seafloor rock has higher porosity and permeability to accommodate the hydrothermal flows. The temperature of the hot fluids near the seafloor might be lower than 170 °C by mixing with cold seawater. If the temperature of the pore fluids is 100 °C, the rock physics model with 41.6% porosity implies that 0.2 Ohm-m resistivity requires existence of 6.4% conductive SMS. The hydrothermal conduits contribute formation of stock-work SMS mineralization. The low resistivity below the seafloor might include both hydrothermal fluids and SMS mineralization. However, it is not reasonable for all parts of the low resistivity area have 6.4% conductive SMS. To discriminate the low resistivity between conductive SMS or hot fluids, other geophysical data such as induced polarization or gravity data are useful.

5.5 Conclusions

The 3D resistivity structures were obtained by applying the inversion algorithm to CSEM survey data collected in a hydrothermal field, mid-Okinawa Trough, southwestern Japan. The 3D inversion algorithm could take into account of 3D resistivity features. The obtained resistivity model by the developed inversion algorithm revealed 3D resistivity features. Thus, the 3D inversion algorithm is more suitable for recovering resistivity structures in this hydrothermal field than the 1D or 2D inversion algorithms.

The very low resistivity anomalies were laterally recovered just below the observed active hydrothermal vents. A sensitivity test showed that the observed CSEM data can sufficiently constrain the low resistivity structures below the seafloor. The existence of the low resistivity structures is supported by the observation of the hydrothermal vents and clear self-potential anomaly. Therefore, they are not artefacts from inversion algorithms but might be related to the formation of SMS deposits. Vertical moderately conductive zones were also imaged. The hydrothermal vents were observed above the vertical conductive zones. The vertical conductive zones are interpreted as the up-flow hydrothermal conduits, stock-work SMS, or both. The hot fluids upwell from the deep parts to the seafloor, and then laterally flows near the seafloor. The lateral flows of hot fluids contribute to the horizontally distributed SMS accumulation below the seafloor.

To reduce computation time, the data-space approach was applied to the Occam inversion algorithm. In this real field example with M=119,156 and N=3,833, the storage of the coefficient matrix would require a factor of 1,000 times less memory than the model-space approach. The developed inversion algorithm could be run with reasonable computation time. This is the first report on 3D resistivity structures of SMS deposits. Based on the real data, I showed that the 3D marine CSEM data-space Occam inversion algorithm is effective for imaging SMS deposits with a reasonable computation time.

Chapter 6

Conceptual model of SMS mineralization from shallow and deep resistivity structures

6.1 Introduction

Accumulation of SMS occurs due to the decline of solubility of metal to mineral-rich fluids. SMS form as chimney structures by mixing of mineral-rich fluids with low-temperature (0°C) and alkalescent seawater (pH~8) at the seafloor (Nozaki *et al.* 2016). Mound-style SMS accumulate via the growth, collapse, and cementation of chimneys (Tornos *et al.* 2015). Another key for SMS accumulation is phase separation of hydrothermal fluids by boiling. Phase separation (gas species such as CO_2 and H_2S into the vapor phase, while ion species such as Cl and Na into the liquid phase) controls fluid chemistry. The liquid phase has lower pH after phase separation. Decreasing of pH of mineral-rich fluids causes a metal accumulation. Phase separation occurs in the mid-Okinawa Trough due to the lower confining pressures from shallower water depths of around 1,000 m (Suzuki *et al.* 2008, Kawagucci *et al.* 2011). Phase separation might greatly contribute to accumulation for hydrothermal fields in the mid-Okinawa Trough. I discuss the generation mechanism based on the resistivity models shown in Fig. 4.3 because of the accumulated data in the Iheya North Knoll hydrothermal field.

6.2 Possible generation mechanism of SMS deposits

I consider a possible mechanism of formation of the semi-layered SMS deposits shown in Fig. 4.3. Because of the good correspondence of the conductive zones (CD1 and CD2) with the hydrothermal vents and high heat flows, hydrothermal fluids are expected to ascend from the deep parts of CD1 and CD2. The hydrothermal waters can be captured by less-permeable cap rocks (CP1 in Fig. 4.3), as inferred from the seismic reflectors and drillings. The trapped hydrothermal fluids precipitated SMS minerals below CP1, thereby forming conductive SMS deposits in CD2.

SMS deposits (CD2) possibly accumulate by decline of solubility of metal to mineral-rich fluids by phase separation. A wide range of Cl concentrations of hydrothermal fluids between 16-585 mmol/kg (seawater: 560 mmol/kg) suggests occurrences of phase separation below the seafloor (Kawagucci *et al.* 2011). Actually, black smoker fluids with high Cl concentrations upwelled to the seafloor after a penetration of drilling to a cap-rock (Kawagucci *et al.* 2013). The fluids with high Cl concentrations indicate occurrences of boiling below the cap rock layer. A numerical simulation also showed that existence of cap rock layer is necessary for occurrences of boiling (Tomita *et al.* 2018).

The hydrothermal fluids passing through the cracks or fractures remaining in the cap rocks (CP1) flows to the seafloor. However, the emitting fluids from hydrothermal vents are clear smoker (Chiba *et* *al.* 1996). Clear smoker fluids have no contribution to accumulation of SMS. This implies that CD1 on the seafloor accumulated before, and are not developing currently. Observation of clear smoker fluids also support that boiling and its associated SMS accumulation occur below the cap rock layer. I propose a conceptual model of SMS mineralization inferred from the resistivity structures (Fig. 6.1). It has combination of two types of SMS mineralization of mound-style SMS and sub-seafloor SMS. The sub-seafloor SMS are developing by phase separation of boiling below a cap rock layer. The emitting fluids are clear smoker flow, not black smoker flow. Thus, the mound SMS used to develop by mixing of mineral-rich fluids with seawater on the seafloor.

Similar two-layer or multilayered SMS structures have been found from drilling in the Iheya North hydrothermal field, not along the towed profile. The LWD exhibited two sequences of large variation in gamma ray and resistivity, each of which indicated a high natural gamma-ray radiation zone, a low-resistivity zone (< 0.3 Ohm-m), and a low-radiation/high-resistive zone from shallow to deep depths (Takai *et al.* 2015). This sequence can be interpreted as a K-rich alteration zone, a buried sulfide zone, and low-K hard (silicified) sediments (Saito *et al.* 2015). Although the two-layer SMS deposits in the Okinawa Trough were revealed by the seafloor drilling, the number of these boreholes was limited. The recovery rate of the core is generally low in the hydrothermal field. Therefore, the obtained resistivity structure is the first detailed image of the two-layer SMS deposits in the Okinawa Trough, and also the first ever reported in the world. At another drilling program in the Izena hydrothermal field, Okinawa Trough, JOGMEC (2013) reported buried SMS deposits at 20 mbsf or much deeper, together with the seafloor SMS mounds. Such complex (two-layered or multilayered) SMS deposits under two or more styles of mineralization are necessary in most cases (in the review by Tornos *et al.* 2015), and might be rather normal.

In the resistivity from the CSEM data covering deep sub-seafloor shown in Fig. 5.5, the 0.2 Ohm-m areas below the seafloor are connected to the vertical hydrothermal conduits. It indicates the hydrothermal fluids and associated SMS laterally are presented below the seafloor. Flow of the upwelling hydrothermal fluids might be guided by impermeable structures. Then, the hydrothermal fluids laterally flow below the impermeable structures. However, such two-layer conductive anomalies were not shown in the resistivity from the CSEM data covering deep sub-seafloor. In this field, SMS mineralization below the seafloor might be a beginning stage.

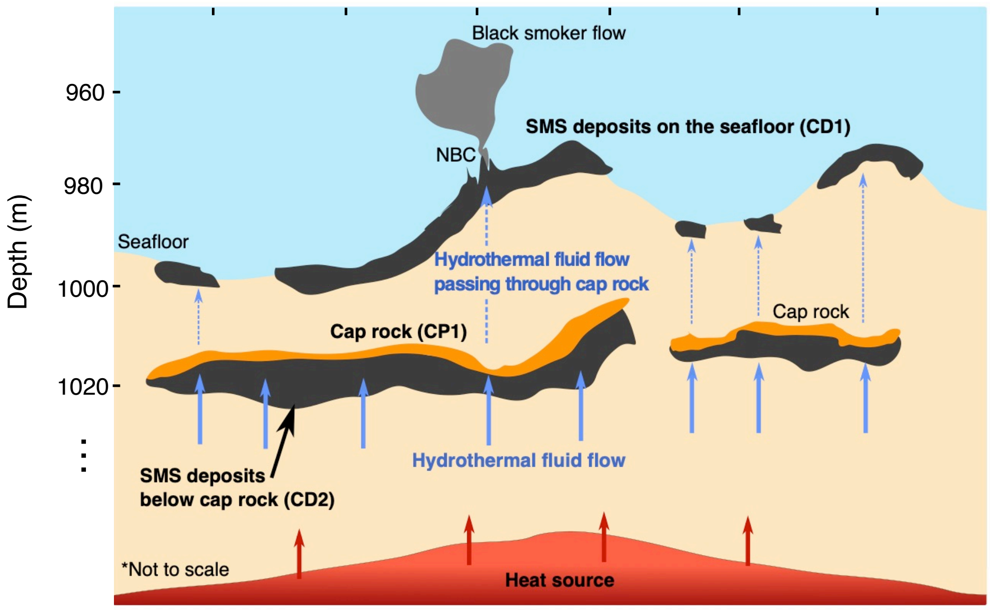

Figure 6.1. Inferred conceptual model of SMS mineralization; it is not to scale.

6.3 Conclusions

I proposed a generation mechanism of SMS deposits inferred from the resistivity structures in previous sections. It has combination of two types of SMS mineralization of mound-style SMS and sub-seafloor SMS. The sub-seafloor SMS are developing due to phase separation occurring below a cap rock layer. The emitting fluids are currently clear smoker flows, not black smoker flows in the Iheya hydrothermal field. Thus, the mound SMS used to develop by mixing of mineral-rich fluids with seawater on the seafloor. This mechanism seems to be a common among SMS accumulation in the mid-Okinawa Trough. Thus, identifying places of phase separation is a key for exploring SMS deposits developing below the seafloor.

Chapter 7

Conclusions

This thesis consists of the development of resistivity imaging techniques based on inversion algorithms of 2D marine ERT surveys and 3D CSEM surveys for the exploration of SMS deposits. The ERT survey tows a transmitter and eight electrode pairs of receivers for increasing resolution to shallow resistivity structures. The high-resolution resistivity images near the seafloor could be obtained by inversion of the ERT data. I focus on a CSEM survey consisting of a towed transmitter and stationary receivers on the seafloor to investigate deep resistivity structures. 3D resistivity images covering the deep area below the seafloor can be obtained by inversion of the CSEM data. I applied the developed inversion algorithms to the observed real field data. The inversion algorithm obtained the detailed resistivity structures in the hydrothermal fields. The resistivity models revealed distribution of SMS mineralization.

I developed a model-space Occam inversion algorithm for the 2D marine ERT survey. The marine 2D ERT forward modeling scheme was solved by the FEM with the unconstructed meshes. The detailed bathymetry can be precisely modeled with unconstructed meshes. Numerical tests suing synthetic data showed the 2D marine ERT inversion algorithm could image the shallowly existing conductive anomalies after a small number of iterations.

The developed 2D inversion algorithm of deep-towed ERT data were applied to the observed data in the Iheya North hydrothermal field, the Okinawa Trough, southwestern Japan. The recovered resistivity cross-section indicates a semi-layered structure consisting of exposed and deeply embedded SMS deposits. This study represents the first reported success in detailed imaging of SMS deposits, which demonstrates the effectiveness of the marine deep-towed ERT system for exploration and characterization of SMS deposits.

A data-space Occam inversion algorithm for the 3D CSEM survey was developed. A 3D marine CSEM forward modeling scheme was also developed using the FDM with the scattered field approach. For the 3D CSEM inversion problem, the number of model parameters is frequently much larger than the number of data Dimension of coefficient matrix for updating models could be reduced, from $M \times M$ in the model-space approach, to $N \times N$ in the data-space approach. The 3D marine CSEM inversion algorithm could image conductive and resistive anomalies embedded into a half-space after a small number of iterations. Combined CSEM inversion algorithm of towed and ocean-bottom electric field receiver data could recover anomalies on the seafloor and also a buried anomaly.

The 3D resistivity structures were obtained by applying the inversion algorithm to CSEM survey data collected in the Ieyama hydrothermal field, mid-Okinawa Trough, southwestern Japan. The obtained resistivity model by the developed inversion algorithm revealed 3D resistivity features. Thus, the 3D inversion algorithm is more suitable for recovering resistivity structures in this hydrothermal field than the 1D or 2D inversion algorithms. The very low resistivity anomalies were laterally recovered just below the observed active hydrothermal vents. Vertical moderately conductive zones were also imaged. The vertical conductive zones are interpreted as the up-flow hydrothermal conduits, stock-work SMS, or both. The hot fluids upwell from the deep parts to the seafloor, and then laterally flows near the seafloor. The lateral flows of hot fluids contribute to the horizontally distributed SMS accumulation below the seafloor.

I proposed a generation mechanism of SMS deposits inferred from the resistivity structures in previous sections. It has combination of two types of SMS mineralization of mound-style SMS and sub-seafloor SMS. The sub-seafloor SMS are developing by phase separation of boiling below a cap rock layer. The emitting fluids are clear smoker flow, not black smoker flow. Thus, the mound SMS used to develop by mixing of mineral-rich fluids with seawater on the seafloor.

These results showed a combination between the inversion of ERT and CSEM data enabled seamless imaging of shallow and deep resistivity structures. The developed inversion techniques can be extended to the exploration of other seafloor resources such as gas hydrate and oil reservoirs. Therefore, the imaging technique is expected to be a common technique for exploring seafloor resources in the future.

Bibliography

Afshar, A., Abedi, M., Norouzi, G.-H. & Riahi, M.-A. (2015) Geophysical investigation of underground water content zones using electrical resistivity tomography and ground penetrating radar: A case study in Hesarak-Karaj, Iran. *Engineering Geology*, **196**, 183–193.

Allen, D. & Merrick, N. (2007) Robust 1D inversion of large towed geo-electric array datasets used for hydrogeological studies. *Exploration Geophysics*, **38**, 50–59.

Amidu, S.A. & Dunbar, J.A. (2008) An evaluation of the electrical-resistivity method for water-reservoir salinity studies. *Geophysics*, **73**, G39–G49.

Ansari, S. & Farquharson, C.G. (2014) 3D finite-element forward modeling of electromagnetic data using vector and scalar potentials and unstructured grids. *Geophysics*, **79**, E149–E165.

Asakawa, E., Sumi, T., Yamakawa, T. & Kose, M. (2016) Multi-stage and integrated approach for seafloor massive sulfide (SMS) exploration. *Near Surface Geoscience 2016-First Conference on Geophysics for Mineral Exploration and Mining*.

Attias, E., Weitemeyer, K., Hölz, S., Naif, S., Minshull, T.A., Best, A.I., Haroon, A., *et al.* (2018) High-resolution resistivity imaging of marine gas hydrate structures by combined inversion of CSEM towed and ocean-bottom receiver data. *Geophysical Journal International*, **214**, 1701–1714.

Attias, E., Weitemeyer, K., Minshull, T.A., Best, A.I., Sinha, M., Jegen-Kulcsar, M., Hölz, S., *et al.* (2016) Controlled-source electromagnetic and seismic delineation of subseafloor fluid flow structures in a gas hydrate province, offshore Norway. *Geophysical Journal International*, **206**, 1093–1110.

Avdeev, D.B., Kuvshinov, A.V., Pankratov, O.V. & Newman, G.A. (2002) Three-dimensional induction logging problems, Part I: An integral equation solution and model comparisons. *Geophysics*, **67**, 413–426.

Baba, K., Tada, N., Utada, H. & Siripunvaraporn, W. (2013) Practical incorporation of local and regional topography in three-dimensional inversion of deep ocean magnetotelluric data. *Geophysical Journal International*, **194**, 348–361.

Biswas, A. & Sharma, S.P. (2016) Integrated geophysical studies to elicit the subsurface structures associated with Uranium mineralization around South Purulia Shear Zone, India: A review. *Ore Geology Reviews*, **72**, 1307–1326.

Blatter, D., Key, K., Ray, A., Gustafson, C. & Evans, R. (2019) Bayesian joint inversion of controlled source electromagnetic and magnetotelluric data to image freshwater aquifer offshore New Jersey. *Geophysical Journal International*, **218**, 1822–1837.

Blome, M., Maurer, H.R. & Schmidt, K. (2009) Advances in three-dimensional geoelectric forward

solver techniques. *Geophysical Journal International*, **176**, 740–752.
Börner, R.-U., Ernst, O.G. & Spitzer, K. (2008) Fast 3-D simulation of transient electromagnetic fields by model reduction in the frequency domain using Krylov subspace projection. *Geophysical Journal International*, **173**, 766–780.
Boschen, R.E., Rowden, A.A., Clark, M.R. & Gardner, J.P. (2013) Mining of deep-sea seafloor massive sulfides: a review of the deposits, their benthic communities, impacts from mining, regulatory frameworks and management strategies. *Ocean & coastal management*, **84**, 54–67.
Cai, H., Hu, X., Li, J., Endo, M. & Xiong, B. (2017) Parallelized 3D CSEM modeling using edge-based finite element with total field formulation and unstructured mesh. *Computers & Geosciences*, **99**, 125–134.
Cairns, G.W., Evans, R.L. & Edwards, R.N. (1996) A time domain electromagnetic survey of the TAG hydrothermal mound. *Geophysical Research Letters*, **23**, 3455–3458.
Chasseriau, P. & Chouteau, M. (2003) 3D gravity inversion using a model of parameter covariance. *Journal of applied geophysics*, **52**, 59–74.
Chave, A.D., Constable, S.C. & Edwards, R.N. (1991) 12. Electrical Exploration Methods for the Seafloor. in *Electromagnetic Methods in Applied Geophysics: Volume 2, Application, Parts A and B* Investigations in Geophysics, Vols 1-0, pp. 931–966, Society of Exploration Geophysicists.
Chave, A.D. & Cox, C.S. (1982) Controlled electromagnetic sources for measuring electrical conductivity beneath the oceans: 1. Forward problem and model study. *Journal of Geophysical Research: Solid Earth*, **87**, 5327–5338.
Chiang, C.-W., Goto, T., Mikada, H., Chen, C.-C. & Hsu, S.-K. (2012) Sensitivity of deep-towed marine electrical resistivity imaging using two-dimensional inversion: A case study on methane hydrate. *TAO: Terrestrial, Atmospheric and Oceanic Sciences*, **23**, 725–732.
Chiba, H., Ishibashi, J., Ueno, H., Oomori, T., Uchiyama, N., Takeda, T., Takamine, C., *et al.* (1996) Seafloor hydrothermal systems at North Knoll, Iheya Ridge, Okinawa Trough. *JAMSTEC. J. Deep-Sea Res.*, **12**, 211–217.
Chiles, J.-P. & Delfiner, P. (2009) *Geostatistics: modeling spatial uncertainty*, Vol. 497, John Wiley & Sons.
Christensen, N.B., Reid, J.E. & Halkjær, M. (2009) Fast, laterally smooth inversion of airborne time-domain electromagnetic data. *Near Surface Geophysics*, **7**, 599–612.
Coggon, J.H. (1971) Electromagnetic and electrical modeling by the finite element method. *Geophysics*, **36**, 132–155.
Commer, M. & Newman, G.A. (2008) New advances in three-dimensional controlled-source electromagnetic inversion. *Geophysical Journal International*, **172**, 513–535.
Constable, S. (2006) Marine electromagnetic methods—A new tool for offshore exploration. *The*

Leading Edge, **25**, 438–444.
Constable, S., Kannberg, P.K. & Weitemeyer, K. (2016) Vulcan: A deep-towed CSEM receiver. *Geochemistry, Geophysics, Geosystems*, **17**, 1042–1064.
Constable, S., Kowalczyk, P. & Bloomer, S. (2018) Measuring marine self-potential using an autonomous underwater vehicle. *Geophysical Journal International*, **215**, 49–60.
Constable, S., Parker, R.L. & Constable, C.G. (1987) Occam's inversion: A practical algorithm for generating smooth models from electromagnetic sounding data. *Geophysics*, **52**, 289–300.
Corliss, J.B., Dymond, J., Gordon, L.I., Edmond, J.M., Herzen, R.P. von, Ballard, R.D., Green, K., *et al.* (1979) Submarine thermal springs on the Galapagos Rift. *Science*, **203**, 1073–1083.
Dakhnov, V.N. (1962) Geophysical Well Logging. *Colorado School of Mines*, **57**.
Davydycheva, S., Druskin, V. & Habashy, T. (2003) An efficient finite-difference scheme for electromagnetic logging in 3D anisotropic inhomogeneous mediaFinite-difference Scheme in Anisotropic Media. *Geophysics*, **68**, 1525–1536.
Day-Lewis, F.D. & Lane Jr, J.W. (2004) Assessing the resolution-dependent utility of tomograms for geostatistics. *Geophysical Research Letters*, **31**, L07503.
Dehiya, R., Singh, A., Gupta, P.K. & Israil, M. (2017) 3-D CSEM data inversion algorithm based on simultaneously active multiple transmitters concept. *Geophysical Journal International*, **209**, 1004–1017.
Dey, A. & Morrison, H.F. (1979) Resistivity modelling for arbitrarily shaped two-dimensional structures. *Geophysical prospecting*, **27**, 106–136.
Doyle, M.G. & Allen, R.L. (2003) Subsea-floor replacement in volcanic-hosted massive sulfide deposits. *Ore Geology Reviews*, **23**, 183–222.
Egbert, G.D. & Kelbert, A. (2012) Computational recipes for electromagnetic inverse problems. *Geophysical Journal International*, **189**, 251–267.
Eidesmo, T., Ellingsrud, S., MacGregor, L.M., Constable, S., Sinha, M.C., Johansen, S., Kong, F.N., *et al.* (2002) Sea bed logging (SBL), a new method for remote and direct identification of hydrocarbon filled layers in deepwater areas. *First break*, **20**, 144–152.
Evans, R.L. (1996) A seafloor gravity profile across the TAG hydrothermal mound. *Geophysical Research Letters*, **23**, 3447–3450.
Evans, R.L., Sinha, M.C., Constable, S. & Unsworth, M.J. (1994) On the electrical nature of the axial melt zone at 13 N on the East Pacific Rise. *Journal of Geophysical Research: Solid Earth*, **99**, 577–588.
Expedition 331 Scientists. (2010) Deep hot biosphere. *IODP Prel. Rept.*, **331**.
Farquharson, C.G. & Miensopust, M.P. (2011) Three-dimensional finite-element modelling of magnetotelluric data with a divergence correction. *Journal of Applied Geophysics*, **75**, 699–710.
Fuji-ta, K. & Ikuta, O. (2000) Resistivity structure of the central part of the Yamasaki fault studied by

the multiple electrodes resistivity method. *Earth, planets and space*, **52**, 567–571.

Gehrmann, R.A.S., North, L.J., Graber, S., Szitkar, F., Petersen, S., Minshull, T.A. & Murton, B.J. (2019) Marine mineral exploration with controlled source electromagnetics at the TAG Hydrothermal Field, 26° N Mid-Atlantic Ridge. *Geophysical Research Letters*, **46**, 5808–5816.

Goswami, B.K., Weitemeyer, K.A., Minshull, T.A., Sinha, M.C., Westbrook, G.K. & Marín-Moreno, H. (2016) Resistivity image beneath an area of active methane seeps in the west Svalbard continental slope. *Geophysical Journal International*, **207**, 1286–1302.

Goto, T., Kasaya, T., Machiyama, H., Takagi, R., Matsumoto, R., Okuda, Y., Satoh, M., *et al.* (2008) A marine deep-towed DC resistivity survey in a methane hydrate area, Japan Sea. *Exploration Geophysics*, **39**, 52–59.

Grayver, A.V., Streich, R. & Ritter, O. (2013) Three-dimensional parallel distributed inversion of CSEM data using a direct forward solver. *Geophysical Journal International*, **193**, 1432–1446.

Gribenko, A. & Zhdanov, M. (2007) Rigorous 3D inversion of marine CSEM data based on the integral equation method. *Geophysics*, **72**, WA73–WA84.

Guptasarma, D. & Singh, B. (1997) New digital linear filters for Hankel J0 and J1 transforms. *Geophysical prospecting*, **45**, 745–762.

Haber, E. (2004) Quasi-Newton methods for large-scale electromagnetic inverse problems. *Inverse problems*, **21**, 305–323.

Hannington, M., Jamieson, J., Monecke, T., Petersen, S. & Beaulieu, S. (2011) The abundance of seafloor massive sulfide deposits. *Geology*, **39**, 1155–1158.

Haroon, A., Hölz, S., Gehrmann, R.A., Attias, E., Jegen, M., Minshull, T.A. & Murton, B.J. (2018) Marine dipole–dipole controlled source electromagnetic and coincident-loop transient electromagnetic experiments to detect seafloor massive sulphides: effects of three-dimensional bathymetry. *Geophysical Journal International*, **215**, 2156–2171.

Hermans, T., Kemna, A. & Nguyen, F. (2016) Covariance-constrained difference inversion of time-lapse electrical resistivity tomography data. *Geophysics*, **81**, E311–E322.

Hermans, T., Vandenbohede, A., Lebbe, L., Martin, R., Kemna, A., Beaujean, J. & Nguyen, F. (2012) Imaging artificial salt water infiltration using electrical resistivity tomography constrained by geostatistical data. *Journal of Hydrology*, **438**, 168–180.

Herzig, P.M. & Hannington, M.D. (1995) Polymetallic massive sulfides at the modern seafloor a review. *Ore Geology Reviews*, **10**, 95–115.

Hesthammer, J., Stefatos, A., Boulaenko, M., Vereshagin, A., Gelting, P., Wedberg, T. & Maxwell, G. (2010) CSEM technology as a value driver for hydrocarbon exploration. *Marine and Petroleum Geology*, **27**, 1872–1884.

Honsho, C., Ura, T. & Kim, K. (2013) Deep-sea magnetic vector anomalies over the Hakurei hydrothermal field and the Bayonnaise knoll caldera, Izu-Ogasawara arc, Japan. *Journal of*

Geophysical Research: Solid Earth, **118**, 5147–5164.
Humphris, S.E., Herzig, P.M., Miller, D.J., Alt, J.C., Becker, K., Brown, D., BrŘgmann, G., *et al.* (1995) The internal structure of an active sea-floor massive sulphide deposit. *Nature*, **377**, 713–716.
Iizasa, K., Fiske, R.S., Ishizuka, O., Yuasa, M., Hashimoto, J., Ishibashi, J., Naka, J., *et al.* (1999) A Kuroko-type polymetallic sulfide deposit in a submarine silicic caldera. *Science*, **283**, 975–977.
Imamura, N., Goto, T., Kasaya, T. & Machiyama, H. (2018) Robust data processing of noisy marine controlled-source electromagnetic data using independent component analysis. *Exploration Geophysics*, **49**, 21–29.
Ishibashi, J., Ikegami, F., Tsuji, T. & Urabe, T. (2015) Hydrothermal activity in the Okinawa Trough back-arc basin: geological background and hydrothermal mineralization. in *Subseafloor biosphere linked to hydrothermal systems*, pp. 337–359, Springer.
Ishizu, K., Goto, T., Ohta, Y., Kasaya, T., Iwamoto, H., Vachiratienchai, C., Siripunvaraporn, W., *et al.* (2019a) Internal Structure of a Seafloor Massive Sulfide Deposit by Electrical Resistivity Tomography, Okinawa Trough. *Geophysical Research Letters*, **46**, 11025–11034.
Ishizu, K., Vachiratienchai, C., Siripunvaraporn, W., Goto, T., Kasaya, T. & Iwamoto, H. (2019b) Evaluations of effectiveness of marine deep-towed DC resistivity survey in investigation of seafloor massive sulfide deposits. *BUTSURI-TANSA(Geophysical Exploration)*, **72**, 122–138.
Jaysaval, P., Shantsev, D.V. & Kethulle de Ryhove, S. de la. (2015) Efficient 3-D controlled-source electromagnetic modelling using an exponential finite-difference method. *Geophysical Journal International*, **203**, 1541–1574.
JOGMEC. (2013) News Release. Retrieved February 20, 2020, from http://www.jogmec.go.jp/news/release/news_06_000130.html
Johansen, S.E., Panzner, M., Mittet, R., Amundsen, H.E., Lim, A., Vik, E., Landrø, M., *et al.* (2019) Deep electrical imaging of the ultraslow-spreading Mohns Ridge. *Nature*, **567**, 379–383.
Jordi, C., Doetsch, J., Günther, T., Schmelzbach, C. & Robertsson, J.O. (2018) Geostatistical regularization operators for geophysical inverse problems on irregular meshes. *Geophysical Journal International*, **213**, 1374–1386.
Kasaya, T. & Goto, T. (2009) A small ocean bottom electromagnetometer and ocean bottom electrometer system with an arm-folding mechanism (Technical Report). *Exploration Geophysics*, **40**, 41–48.
Kasaya, T., Goto, T., Iwamoto, H. & Kawada, Y. (2019) Development of multi-purpose electromagnetic survey instruments. *The 13th SEGJ International Symposium, Tokyo, Japan, 12-14 November 2018*, pp. 159–161, Society of Exploration Geophysicists.
Kasaya, T., Kaneko, J. & Iwamoto, H. (2020) Observation and confirmation based on survey protocol for seafloor massive sulfide deposits using acoustic survey technique and self-potential surveys.

BUTSURI-TANSA(Geophysical Exploration), **72**, 155–165.
Kasaya, T., Machiyama, H., Kitada, K. & Nakamura, K. (2015) Trial exploration for hydrothermal activity using acoustic measurements at the North Iheya Knoll. *Geochemical Journal*, **49**, 597–602.
Kawada, Y. & Kasaya, T. (2017) Marine self-potential survey for exploring seafloor hydrothermal ore deposits. *Scientific reports*, **7**, 13552.
Kawagucci, S., Chiba, H., Ishibashi, J., Yamanaka, T., Toki, T., Muramatsu, Y., Ueno, Y., *et al.* (2011) Hydrothermal fluid geochemistry at the Iheya North field in the mid-Okinawa Trough: Implication for origin of methane in subseafloor fluid circulation systems. *Geochemical Journal*, **45**, 109–124.
Kawagucci, S., Miyazaki, J., Nakajima, R., Nozaki, T., Takaya, Y., Kato, Y., Shibuya, T., *et al.* (2013) Post-drilling changes in fluid discharge pattern, mineral deposition, and fluid chemistry in the Iheya North hydrothermal field, Okinawa Trough. *Geochemistry, Geophysics, Geosystems*, **14**, 4774–4790.
Keller, G.V. (1988) 2. Rock and Mineral Properties. in *Electromagnetic Methods in Applied Geophysics: Volume 1, Theory* Investigations in Geophysics, Vols 1-0, pp. 12–51, Society of Exploration Geophysicists.
Key, K. (2009) 1D inversion of multicomponent, multifrequency marine CSEM data: Methodology and synthetic studies for resolving thin resistive layers. *Geophysics*, **74**, F9–F20.
Key, K. (2012) Marine electromagnetic studies of seafloor resources and tectonics. *Surveys in geophysics*, **33**, 135–167.
Key, K. (2016) MARE2DEM: a 2-D inversion code for controlled-source electromagnetic and magnetotelluric data. *Geophysical Journal International*, **207**, 571–588.
Key, K. & Weiss, C. (2006) Adaptive finite-element modeling using unstructured grids: The 2D magnetotelluric example. *Geophysics*, **71**, G291–G299.
Komori, S., Masaki, Y., Tanikawa, W., Torimoto, J., Ohta, Y., Makio, M., Maeda, L., *et al.* (2017) Depth profiles of resistivity and spectral IP for active modern submarine hydrothermal deposits: a case study from the Iheya North Knoll and the Iheya Minor Ridge in Okinawa Trough, Japan. *Earth, Planets and Space*, **69**, 114.
Kong, F.N. (2007) Hankel transform filters for dipole antenna radiation in a conductive medium. *Geophysical Prospecting*, **55**, 83–89.
Kordy, M., Wannamaker, P., Maris, V., Cherkaev, E. & Hill, G. (2016) 3-dimensional magnetotelluric inversion including topography using deformed hexahedral edge finite elements and direct solvers parallelized on symmetric multiprocessor computers–Part II: direct data-space inverse solution. *Geophysical Journal International*, **204**, 94–110.
Kowalczyk, P. (2008) Geophysical prelude to first exploitation of submarine massive sulphides. *First*

Break, **26**, 99–106.

Kumagai, H., Nozaki, T., Ishibashi, J. -i & Maeda, L. (2017) Cruise Report SIP-HOT II" Explorer"(SIP-Hydrothermal deposit in Okinawa Trough) CK16-01 (Exp. 908), JAMSTEC, 443.

Kumagai, H., Tsukioka, S., Yamamoto, H., Tsuji, T., Shitashima, K., Asada, M., Yamamoto, F., *et al.* (2010) Hydrothermal plumes imaged by high-resolution side-scan sonar on a cruising AUV, Urashima. *Geochemistry, Geophysics, Geosystems*, **11**, Q12013.

Kwon, H.-S., Kim, J.-H., Ahn, H.-Y., Yoon, J.-S., Kim, K.-S., Jung, C.-K., Lee, S.-B., *et al.* (2005) Delineation of a fault zone beneath a riverbed by an electrical resistivity survey using a floating streamer cable. *Exploration Geophysics*, **36**, 50–58.

Legault, J.M., Carriere, D. & Petrie, L. (2008) Synthetic model testing and distributed acquisition dc resistivity results over an unconformity uranium target from the Athabasca Basin, northern Saskatchewan. *The Leading Edge*, **27**, 46–51.

Letouzey, J. & Kimura, M. (1986) The Okinawa Trough: genesis of a back-arc basin developing along a continental margin. *Tectonophysics*, **125**, 209–230.

Li, G., Li, Y. & Han, B. (2017) Accurate interpolation at receiver positions: A novel method for frequency-domain marine CSEM finite-difference modelling. *Pure and Applied Geophysics*, **174**, 2143–2160.

Li, G., Li, Y., Han, B. & Liu, Z. (2018) Application of the perfectly matched layer in 3-D marine controlled-source electromagnetic modelling. *Geophysical Journal International*, **212**, 333–344.

Li, Y. & Li, G. (2016) Electromagnetic field expressions in the wavenumber domain from both the horizontal and vertical electric dipoles. *Journal of Geophysics and Engineering*, **13**, 505–515.

Li, Y. & Spitzer, K. (2002) Three-dimensional DC resistivity forward modelling using finite elements in comparison with finite-difference solutions. *Geophysical Journal International*, **151**, 924–934.

Linde, N., Binley, A., Tryggvason, A., Pedersen, L.B. & Revil, A. (2006) Improved hydrogeophysical characterization using joint inversion of cross-hole electrical resistance and ground-penetrating radar traveltime data. *Water Resources Research*, **42**, W12404.

Lipton, I. (2012) Mineral Resource Estimate, Solwara Project, Bismarck Sea, PNG, p. 240. Retrieved from http://www.nautilusminerals.com/irm/content/pdf/SL01-NSG-DEV-RPT-7020-001_Rev_1_Golder_Resource_Report.pdf

Løseth, L.O. & Ursin, B. (2007) Electromagnetic fields in planarly layered anisotropic media. *Geophysical Journal International*, **170**, 44–80.

MacGregor, L.M., Constable & Sinha, M.C. (1998) The RAMESSES experiment—III. Controlled-source electromagnetic sounding of the Reykjanes Ridge at 57° 45′ N. *Geophysical Journal International*, **135**, 773–789.

Mackie, R.L. & Madden, T.R. (1993) Conjugate direction relaxation solutions for 3-D magnetotelluric modeling. *Geophysics*, **58**, 1052–1057.

Mansoor, N. & Slater, L. (2007) Aquatic electrical resistivity imaging of shallow-water wetlands. *Geophysics*, **72**, F211–F221.

Masaki, Y., Kinoshita, M., Inagaki, F., Nakagawa, S. & Takai, K. (2011) Possible kilometer-scale hydrothermal circulation within the Iheya-North field, mid-Okinawa Trough, as inferred from heat flow data. *JAMSTEC Report of Research and Development*, **12**, 1–12.

Maurer, H., Holliger, K. & Boerner, D.E. (1998) Stochastic regularization: Smoothness or similarity? *Geophysical Research Letters*, **25**, 2889–2892.

Miller, A.R., Densmore, C.D., Degens, E.T., Hathaway, J.C., Manheim, F.T., McFarlin, P.F., Pocklington, R., *et al.* (1966) Hot brines and recent iron deposits in deeps of the Red Sea. *Geochimica et Cosmochimica Acta*, **30**, 341–359.

Minami, T., Utsugi, M., Utada, H., Kagiyama, T. & Inoue, H. (2018) Temporal variation in the resistivity structure of the first Nakadake crater, Aso volcano, Japan, during the magmatic eruptions from November 2014 to May 2015, as inferred by the ACTIVE electromagnetic monitoring system. *Earth, Planets and Space*, **70**, 138.

Misonou, T., Asaue, H., Koike, K., Shimada, J., Yoshinaga, T. & Inoue, M. (2012) Imaging of Geologic Structures and Groundwater-discharge Paths in the Shallow Depths under the Sea Bottom of Ariake and Yatsushiro Seas by Electric Sounding Survey. *Journal of the Japan Society of Engineering Geology*, **53**, 235–244.

Mittet, R. (2010) High-order finite-difference simulations of marine CSEM surveys using a correspondence principle for wave and diffusion fields. *Geophysics*, **75**, F33–F50.

Miyoshi, Y., Ishibashi, J., Shimada, K., Inoue, H., Uehara, S. & Tsukimura, K. (2015) Clay minerals in an active hydrothermal field at Iheya-North-Knoll, Okinawa Trough. *Resource Geology*, **65**, 346–360.

Monecke, T., Petersen, S., Hannington, M.D., Grant, H. & Samson, I. (2016) The minor element endowment of modern sea-floor massive sulfides and comparison with deposits hosted in ancient volcanic successions. *Reviews in Economic Geology*, **18**, 245–306.

Müller, H., Schwalenberg, K., Reeck, K., Barckhausen, U., Schwarz-Schampera, U., Hilgenfeldt, C. & Dobeneck, T. von. (2018) Mapping seafloor massive sulfides with the Golden Eye frequency-domain EM profiler. *First Break*, **36**, 61–67.

Murton, B.J., Lehrmann, B., Dutrieux, A.M., Martins, S., Iglesia, A.G. de la, Stobbs, I.J., Barriga, F.J., *et al.* (2019) Geological fate of seafloor massive sulphides at the TAG hydrothermal field (Mid-Atlantic Ridge). *Ore Geology Reviews*, **107**, 903–925.

Myer, D., Constable, S. & Key, K. (2011) Broad-band waveforms and robust processing for marine CSEM surveys. *Geophysical Journal International*, **184**, 689–698.

Myer, D., Key, K. & Constable, S. (2015) Marine CSEM of the Scarborough gas field, Part 2: 2D inversion. *Geophysics*, **80**, E187–E196.

Nakagawa, S., Takai, K., Inagaki, F., Chiba, H., Ishibashi, J., Kataoka, S., Hirayama, H., *et al.* (2005) Variability in microbial community and venting chemistry in a sediment-hosted backarc hydrothermal system: impacts of subseafloor phase-separation. *FEMS microbiology ecology*, **54**, 141–155.

Nakayama, K. & Saito, A. (2016) The seabed TDEM towed by ROV for the ocean bottom hydrothermal deposits. *Near Surface Geoscience 2016-First Conference on Geophysics for Mineral Exploration and Mining*.

Nam, M.J., Kim, H.J., Song, Y., Lee, T.J., Son, J.-S. & Suh, J.H. (2007) 3D magnetotelluric modelling including surface topography. *Geophysical Prospecting*, **55**, 277–287.

Negri, S., Leucci, G. & Mazzone, F. (2008) High resolution 3D ERT to help GPR data interpretation for researching archaeological items in a geologically complex subsurface. *Journal of Applied Geophysics*, **65**, 111–120.

Nelder, J.A. & Mead, R. (1965) A simplex method for function minimization. *The computer journal*, **7**, 308–313.

New Energy and Industrial Technology Development Organization (NEDO). (1995) Report of exploration for development of geothermal power in west Aso area. Retrieved February 20, 2020, from http://geothermal.jogmec.go.jp/gathering/file/57.pdf

Newman, G.A. & Alumbaugh, D.L. (1997) Three-dimensional massively parallel electromagnetic inversion—I. Theory. *Geophysical journal international*, **128**, 345–354.

Nozaki, T., Ishibashi, J.-I., Shimada, K., Nagase, T., Takaya, Y., Kato, Y., Kawagucci, S., *et al.* (2016) Rapid growth of mineral deposits at artificial seafloor hydrothermal vents. *Scientific Reports*, **6**, 1–10, Nature Publishing Group.

Ohta, Y., Goto, T., Koike, K., Kashiwaya, K., Lin, W., Tadai, O., Kasaya, T., *et al.* (2018) Construction of rock physics model based on electrical conductivity characteristics of rock samples obtained in seafloor hydrothermal areas. *Exploration Geophysics (Butsuri-Tansa)*, **71**, 43–55.

Oldenburg, D.W., Haber, E. & Shekhtman, R. (2013) Three dimensional inversion of multisource time domain electromagnetic data. *Geophysics*, **78**, E47–E57.

Osella, A., Vega, M. de la & Lascano, E. (2005) 3D electrical imaging of an archaeological site using electrical and electromagnetic methods. *Geophysics*, **70**, G101–G107.

Palacky, G.J. (1988) 3. Resistivity Characteristics of Geologic Targets. in *Electromagnetic Methods in Applied Geophysics: Volume 1, Theory* Investigations in Geophysics, Vols 1-0, pp. 52–129, Society of Exploration Geophysicists.

Pan, K. & Tang, J. (2014) 2.5-D and 3-D DC resistivity modelling using an extrapolation cascadic multigrid method. *Geophysical Journal International*, **197**, 1459–1470.

Pelton, W.H., Ward, S.H., Hallof, P.G., Sill, W.R. & Nelson, P.H. (1978) Mineral discrimination and removal of inductive coupling with multifrequency IP. *Geophysics*, **43**, 588–609.

Petersen, S., Herzig, P.M. & Hannington, M.D. (2000) Third dimension of a presently forming VMS deposit: TAG hydrothermal mound, Mid-Atlantic Ridge, 26 N. *Mineralium Deposita*, **35**, 233–259.

Petersen, S., Lehrmann, B. & Murton, B.J. (2018) Modern seafloor hydrothermal systems: new perspectives on ancient ore-forming processes. *Elements: An International Magazine of Mineralogy, Geochemistry, and Petrology*, **14**, 307–312.

Petersen, S., Monecke, T., Westhues, A., Hannington, M.D., Gemmell, J.B., Sharpe, R., Peters, M., *et al.* (2014) Drilling shallow-water massive sulfides at the Palinuro volcanic complex, Aeolian island arc, Italy. *Economic Geology*, **109**, 2129–2158.

Puzyrev, V., Koric, S. & Wilkin, S. (2016) Evaluation of parallel direct sparse linear solvers in electromagnetic geophysical problems. *Computers & Geosciences*, **89**, 79–87.

Quist, A.S. & Marshall, W.L. (1968) Electrical conductances of aqueous sodium chloride solutions from 0 to 800. degree. and at pressures to 4000 bars. *The journal of physical chemistry*, **72**, 684–703.

Ray, A. & Key, K. (2012) Bayesian inversion of marine CSEM data with a trans-dimensional self parametrizing algorithm. *Geophysical Journal International*, **191**, 1135–1151.

Ren, Z., Kalscheuer, T., Greenhalgh, S. & Maurer, H. (2013) A goal-oriented adaptive finite-element approach for plane wave 3-D electromagnetic modelling. *Geophysical Journal International*, **194**, 700–718.

Revil, A., Florsch, N. & Mao, D. (2015) Induced polarization response of porous media with metallic particles—Part 1: A theory for disseminated semiconductors. *Geophysics*, **80**, D525–D538.

Rona, P.A. (1988) Hydrothermal mineralization at oceanic ridges. *The Canadian Mineralogist*, **26**, 431–465.

Rücker, C., Günther, T. & Spitzer, K. (2006) Three-dimensional modelling and inversion of dc resistivity data incorporating topography—I. Modelling. *Geophysical Journal International*, **166**, 495–505.

Safipour, R., Hölz, S., Jegen, M. & Swidinsky, A. (2017) On electric fields produced by inductive sources on the seafloor. *Geophysics*, **82**, E297–E313.

Safipour, R., Hölz, S., Jegen, M. & Swidinsky, A. (2018) A first application of a marine inductive source electromagnetic configuration with remote electric dipole receivers: Palinuro Seamount, Tyrrhenian Sea. *Geophysical Prospecting*, **66**, 1415–1432.

Saito, S., Sanada, Y., Moe, K., Kido, Y.N., Hamada, Y., Kumagai, H., Nozaki, T., *et al.* (2015) Identification and characterization of the active hydrothermal deposits in Okinawa Trough, SW Japan: estimates from logging-while-drilling. *AGU Fall Meeting Abstracts*.

Sasaki, Y. & Meju, M.A. (2009) Useful characteristics of shallow and deep marine CSEM responses inferred from 3D finite-difference modeling. *Geophysics*, **74**, F67–F76.

Schenk, O. & Gärtner, K. (2004) Solving unsymmetric sparse systems of linear equations with PARDISO. *Future Generation Computer Systems*, **20**, 475–487.

Schwalenberg, K., Haeckel, M., Poort, J. & Jegen, M. (2010) Evaluation of gas hydrate deposits in an active seep area using marine controlled source electromagnetics: Results from Opouawe Bank, Hikurangi Margin, New Zealand. *Marine Geology*, **272**, 79–88.

Schwalenberg, K., Rath, V. & Haak, V. (2002) Sensitivity studies applied to a two-dimensional resistivity model from the Central Andes. *Geophysical Journal International*, **150**, 673–686.

Schwarzbach, C., Börner, R.-U. & Spitzer, K. (2011) Three-dimensional adaptive higher order finite element simulation for geo-electromagnetics—a marine CSEM example. *Geophysical Journal International*, **187**, 63–74.

Schwarzbach, C. & Haber, E. (2013) Finite element based inversion for time-harmonic electromagnetic problems. *Geophysical Journal International*, **193**, 615–634.

Shewchuk, J.R. (1996) Triangle: Engineering a 2D quality mesh generatorand Delaunay triangulator. *Applied Computational Geometry:Towards Geometric Engineering*, 203–222.

Sibuet, J.-C., Deffontaines, B., Hsu, S.-K., Thareau, N., Le Formal, J.-P. & Liu, C.-S. (1998) Okinawa trough backarc basin: Early tectonic and magmatic evolution. *Journal of Geophysical Research: Solid Earth*, **103**, 30245–30267.

Silva, N.V. da, Morgan, J.V., MacGregor, L. & Warner, M. (2012) A finite element multifrontal method for 3D CSEM modeling in the frequency domain. *Geophysics*, **77**, E101–E115.

Sinha, M.C., Patel, P.D., Unsworth, M.J., Owen, T.R.E. & MacCormack, M.R.G. (1990) An active source electromagnetic sounding system for marine use. *Marine Geophysical Researches*, **12**, 59–68.

Siripunvaraporn, W. & Egbert, G. (2000) An efficient data-subspace inversion method for 2-D magnetotelluric data. *Geophysics*, **65**, 791–803.

Siripunvaraporn, W., Egbert, G., Lenbury, Y. & Uyeshima, M. (2005) Three-dimensional magnetotelluric inversion: data-space method. *Physics of the Earth and planetary interiors*, **150**, 3–14.

Smith, J.T. (1996) Conservative modeling of 3-D electromagnetic fields, Part II: Biconjugate gradient solution and an accelerator. *Geophysics*, **61**, 1319–1324.

Spagnoli, G., Hannington, M., Bairlein, K., Hördt, A., Jegen, M., Petersen, S. & Laurila, T. (2016) Electrical properties of seafloor massive sulfides. *Geo-Marine Letters*, **36**, 235–245.

Stein, C.A. & Stein, S. (1992) A model for the global variation in oceanic depth and heat flow with lithospheric age. *Nature*, **359**, 123–129.

Streich, R. (2009) 3D finite-difference frequency-domain modeling of controlled-source electromagnetic data: Direct solution and optimization for high accuracy. *Geophysics*, **74**, F95–

F105.

Suzuki, K., Toda, S., Kusunoki, K., Fujimitsu, Y., Mogi, T. & Jomori, A. (2000) Case studies of electrical and electromagnetic methods applied to mapping active faults beneath the thick quaternary. *Developments in geotechnical engineering*, **84**, 29–45.

Suzuki, R., Ishibashi, J.-I., Nakaseama, M., Konno, U., Tsunogai, U., Gena, K. & Chiba, H. (2008) Diverse Range of Mineralization Induced by Phase Separation of Hydrothermal Fluid: Case Study of the Yonaguni Knoll IV Hydrothermal Field in the Okinawa Trough Back-Arc Basin. *Resource Geology*, **58**, 267–288.

Takai, K., Kumagai, H. & Kubo, Y. (2015) Cruise report SIP-HOT I "Pathfinder"(SIP-Hydrothermal deposit in Okinawa Trough) CK14-04 (Exp. 907). *JAMSTEC, Yokosuka, Japan*, 1–116.

Takai, K., Mottl, M.J., Nielsen, S.H. & Scientists, E. 331. (2011) Proceedings of the Integrated Ocean Drilling Program.

Takai, K., Nakagawa, S., Reysenbach, A.-L. & Hoek, J. (2006) Microbial ecology of mid-ocean ridges and back-arc basins. *Geophysical Monograph—American Geophysical Union*, **166**, 185–213.

Tomita, S.A., Koike, K., Goto, T.N. & Suzuki, K. (2018) Modeling of magmatic-hydrothermal fluid system in seafloor vent areas in Japan using TOUGH2. *AGU Fall Meeting Abstracts*, **43**.

Tornos, F. (2006) Environment of formation and styles of volcanogenic massive sulfides: The Iberian Pyrite Belt. *Ore Geology Reviews*, **28**, 259–307.

Tornos, F., Peter, J.M., Allen, R. & Conde, C. (2015) Controls on the siting and style of volcanogenic massive sulphide deposits. *Ore Geology Reviews*, **68**, 142–163.

Tsuji, T., Takai, K., Oiwane, H., Nakamura, Y., Masaki, Y., Kumagai, H., Kinoshita, M., *et al.* (2012) Hydrothermal fluid flow system around the Iheya North Knoll in the mid-Okinawa trough based on seismic reflection data. *Journal of Volcanology and Geothermal Research*, **213**, 41–50.

Um, E.S., Commer, M. & Newman, G.A. (2013) Efficient pre-conditioned iterative solution strategies for the electromagnetic diffusion in the Earth: finite-element frequency-domain approach. *Geophysical Journal International*, **193**, 1460–1473.

U.S. Energy Information Administration. (2015) Offshore production nearly 30% of global crude oil output in 2015. Retrieved from https://www.eia.gov/todayinenergy/detail.php?id=28492#

Usui, Y., Kasaya, T., Ogawa, Y. & Iwamoto, H. (2018) Marine magnetotelluric inversion with an unstructured tetrahedral mesh. *Geophysical Journal International*, **214**, 952–974.

Usui, Y., Ogawa, Y., Aizawa, K., Kanda, W., Hashimoto, T., Koyama, T., Yamaya, Y., *et al.* (2017) Three-dimensional resistivity structure of Asama Volcano revealed by data-space magnetotelluric inversion using unstructured tetrahedral elements. *Geophysical Journal International*, **208**, 1359–1372.

Vachiratienchai, C. & Siripunvaraporn, W. (2013) An efficient inversion for two-dimensional direct current resistivity surveys based on the hybrid finite difference–finite element method. *Physics of* *the Earth and Planetary Interiors*, **215**, 1–11.

Von Herzen, R.P., Kirklin, J. & Becker, K. (1996) Geoelectrical measurements at the TAG hydrothermal mound. *Geophysical Research Letters*, **23**, 3451–3454.

Wang, F., Morten, J.P. & Spitzer, K. (2018) Anisotropic three-dimensional inversion of CSEM data using finite-element techniques on unstructured grids. *Geophysical Journal International*, **213**, 1056–1072.

Wang, K., Tan, H., Lin, C., Yuan, J., Wang, C. & Tang, J. (2018) Three-dimensional tensor controlled-source audio-frequency magnetotelluric inversion using LBFGS. *Exploration Geophysics*, **49**, 268–284.

Ward, S.H. & Hohmann, G.W. (1988) Electromagnetic theory for geophysical applications. in *Electromagnetic Methods in Applied Geophysics: Voume 1, Theory*, pp. 130–311, Society of Exploration Geophysicists.

Weiss, C.J. & Constable, S. (2006) Mapping thin resistors and hydrocarbons with marine EM methods, Part II—Modeling and analysis in 3D. *Geophysics*, **71**, G321–G332.

Weitemeyer, K.A., Constable, S. & Tréhu, A.M. (2011) A marine electromagnetic survey to detect gas hydrate at Hydrate Ridge, Oregon. *Geophysical Journal International*, **187**, 45–62.

Wheelock, B., Constable, S. & Key, K. (2015) The advantages of logarithmically scaled data for electromagnetic inversion. *Geophysical Journal International*, **201**, 1765–1780.

Wilt, M.J., Alumbaugh, D.L., Morrison, H.F., Becker, A., Lee, K.H. & Deszcz-Pan, M. (1995) Crosswell electromagnetic tomography: System design considerations and field results. *Geophysics*, **60**, 871–885.

Wynn, J.C. (1988) Titanium geophysics: The application of induced polarization to sea-floor mineral exploration. *Geophysics*, **53**, 386–401.

Xu, S., Duan, B. & Zhang, D. (2000) Selection of the wavenumbers k using an optimization method for the inverse Fourier transform in 2.5 D electrical modelling. *Geophysical Prospecting*, **48**, 789–796.

Yamaji, N., Okamoto, N., Shiokawa, S., Kawano, S. & Sakurai, H. (2019) Achievement for Pilot Test of Excavating and Ore Lifting Conducted for Seafloor Polymetallic Sulphides. *Journal of MMIJ*, **135**, 42–51.

Yamane, K., Tuji, Y., Akiyoshi, K. & Nagasaki, Y. (2009) Marine controlled-source electromagnetic sounding for hydrocarbon detection and case study. *Journal of the Japanese Association for Petroleum Technology*, **74**, 80–91.

Yeats, C.J., Hollis, S.P., Halfpenny, A., Corona, J.-C., LaFlamme, C., Southam, G., Fiorentini, M., *et al.* (2017) Actively forming Kuroko-type volcanic-hosted massive sulfide (VHMS) mineralization at Iheya North, Okinawa Trough, Japan. *Ore Geology Reviews*, **84**, 20–41.

Yee, K. (1966) Numerical solution of initial boundary value problems involving Maxwell's equations in isotropic media. *IEEE Transactions on antennas and propagation*, **14**, 302–307.

Yuan, J. & Edwards, R.N. (2000) The assessment of marine gas hydrates through electrical remote sounding: Hydrate without a BSR? *Geophysical Research Letters*, **27**, 2397–2400.

Zhang, Y. & Key, K. (2016) MARE3DEM: a three-dimensional CSEM inversion based on a parallel adaptive finite element method using unstructured meshes. in *SEG Technical Program Expanded Abstracts 2016*, pp. 1009–1013, Society of Exploration Geophysicists.

Zhdanov, M.S., Endo, M., Yoon, D., Čuma, M., Mattsson, J. & Midgley, J. (2014) Anisotropic 3D inversion of towed-streamer electromagnetic data: Case study from the Troll West Oil Province. *Interpretation*, **2**, SH97–SH113.

Zierenberg, R.A., Fouquet, Y., Miller, D.J., Bahr, J.M., Baker, P.A., Bjerkgård, T., Brunner, C.A., *et al.* (1998) The deep structure of a sea-floor hydrothermal deposit. *Nature*, **392**, 485–488.